UNIVERSITAT DE BARCELONA

Ti-containing hybrid organosilicas, $Mo_xC/g\text{-}C_3N_4$ nanocomposites and engineered Mo_xC/TiO_2 nanomaterials as noble-metal-free photocatalysts for H_2 production

Yan Wang

Aquesta tesi doctoral està subjecta a la llicència ***Reconeixement- NoComercial 4.0. Espanya de Creative Commons***.

Esta tesis doctoral está sujeta a la licencia ***Reconocimiento - NoComercial 4.0. España de Creative* Commons**.

This doctoral thesis is licensed under the ***Creative Commons Attribution-NonCommercial 4.0. Spain License***.

Doctoral Thesis

Ti-containing hybrid organosilicas, Mo_xC/g-C_3N_4 nanocomposites and engineered Mo_xC/TiO_2 nanomaterials as noble-metal-free photocatalysts for H_2 production

Author:

Yan Wang

Directors:

Dra. Maria Pilar Ramírez de la Piscina Millán

Dr. Narcís Homs Martí

UNIVERSITAT DE BARCELONA

Document signat digitalment per: YAN WANG

Ti-containing hybrid organosilicas, $Mo_xC/g\text{-}C_3N_4$ nanocomposites and engineered Mo_xC/TiO_2 nanomaterials as noble-metal-free photocatalysts for H_2 production

Memòria presentada per optar al grau de doctor per la Universitat de Barcelona

Programa de doctorat en Nanociències

Autor:

Yan Wang

Directors:

Dra. Maria Pilar Ramírez de la Piscina Millán

Dr. Narcís Homs Martí

Tutor:

Dr. Narcís Homs Martí

UNIVERSITAT DE BARCELONA

Acknowledgments

When I start to write the final section of my thesis, my five years of study experience at UB and all my best memories here come back clearly to me, some can even make lump in my throat. Just like before, it is yesterday once more.

Firstly, I would like to express my sincere gratitude to my supervisors, **Prof. Dr. Pilar Ramírez de la Piscina Millán** and **Prof. Dr. Narcís Homs**. Thanks for giving me the opportunity to study in Catalysis and Materials group (MATCAT) in UB. Your patience and scientific manner for my thesis correction make a profound impression to me. The moment in the lab with Prof. Narcís for the equipment fixing and the time in Prof. Pilar's office for the discussion of the experimental results, all make me miss the life in UB.

Secondly, I would like to give my deep gratitude to all the members in MATCAT group: Alberto, Lukasz, Xianyun, Arturo, Paulina, DJ, Michael, Grace, Albert, Blai, Neus, Zeno, Maria, Khaled and Moha. I really enjoy all the moments with you in our group which gives me a lot of happy and unforgettable memories. I would like to thank Dr. Carolina in the Department of Inorganic Chemistry and Dr. Frank in the Faculty of Physics for the research using microwave reactor and on the measurement of photoluminescence in UB, respectively. In the meanwhile, I wish to thank Dr. Teresa, Dr. Sebastian, and technicians Martí, Marco and Dr. Diouldé for the help in the measurements in IREC.

Lastly, I would like to say thanks to my Chinese friends, Ahuang, Chenyang, Jinya, Laoluo, Miaomiao, Teni, Xiaomu, who are studying together with me in Barcelona. The Chinese New Year, the hotpot dinner and the parties we celebrated together is the most important part to me in Barcelona. Moreover, I am extremely grateful to Mengxi, you always give me useful suggestions when

I have troubles. Also, I am extending my heartfelt thanks to Nana, thanks for your support, especially in those hard periods.

I would like to thank China Scholarship Council (CSC) for providing me the financial support, which give me an opportunity to study abroad.

Last but not the least, I am extremely grateful to my parents, who give me love, caring and support, make me go forward courageously when I am faced with any difficulty. I wish in the future, I can take more time with you.

Summary

The photocatalytic hydrogen production is considered an environmentally promising and friendly method, which could lead to achieve clean and renewable hydrogen and contribute in the future to store solar energy as chemical energy.

Inorganic semiconductor materials are usually used as photocatalysts and different strategies are applied in order to avoid the recombination of photogenerated charges, one of these strategies is the addition of noble-metals as co-catalysts. However, the use of noble metal-free photocatalysts has attracted great attention in the last decade. On the other hand, the use of sacrificial electron donors as hole scavengers increases the yield of the process when compared with pure water-splitting. In this context, aqueous solutions of bioalcohols are proposed as attractive sources to produce renewable energy.

In this thesis, three different systems have been developed and studied in the photocatalytic hydrogen production from aqueous solutions of ethanol: Ti-containing hybrid mesoporous organosilicas, Mo_xC/g-C_3N_4 nanocomposites and engineered Mo_xC/TiO_2 nanomaterials.

Photocatalysts have been characterized by different techniques such as, N_2 adsorption-desorption isotherms, powder X-ray diffraction, Fourier-transform infrared, Raman and UV-visible diffuse reflectance spectroscopy, scanning and transmission electron microscopy and X-ray photoelectron spectroscopy. Additionally, photoelectrochemical properties of materials have been evaluated by photoluminescence, photocurrent response measurements and electrochemical impedance spectroscopy.

Mesoporous organic-inorganic hybrid materials with biphenyl moieties and mesoscopically ordered structures (Ti-PMOs) were successfully synthesized using a microwave-assisted method. The presence of tetrahedral Ti^{4+} into the framework of Ti-PMOs is related with a lower rate of photoinduced charge recombination, an easier charge transfer and a better photocatalytic performance of Ti-PMOs hybrid materials.

The preparation of $Mo_xC/g\text{-}C_3N_4$ nanocomposites containing MoC and/or Mo_2C with different sizes onto $g\text{-}C_3N_4$ nanosheets was accomplished using an ultrasonic-assisted method and previously prepared Mo_xC and $g\text{-}C_3N_4$. The Mo_xC characteristics determined the photoelectrochemical behaviour of $Mo_xC/g\text{-}C_3N_4$ and consequently their photocatalytic behaviour. The system containing simultaneously hcp Mo_2C and fcc MoC was the most efficient.

Shape-engineered TiO_2 anatase nanoparticles (nanosheets and bipyramids) were used for the preparation of Mo_xC/TiO_2 nanocomposites in order to study the effect of Mo_xC in the photocatalytic behaviour of Mo_xC/TiO_2. Although in all cases, a beneficial effect of Mo_xC presence was found, the effect depended on the shape of TiO_2. Specifically, a correlation between the exposition of (101) facets onto anatase nanoparticles and the efficiency of the final system is established.

Resumen

La producción fotocatalítica de hidrogeno se considera una ruta medioambientalmente interesante que puede dar lugar a la producción de hidrogeno renovable y por tanto contribuir en un futuro al almacenamiento de energía solar como energía química.

Se han estudiado muchos materiales inorgánicos semiconductores como fotocatalizadores, y se han seguido diversas estrategias para intentar evitar la recombinación de las cargas fotogeneradas. Una de las estrategias es la adición al semiconductor de metales nobles como co-catalizadores. Sin embargo, es preferible el uso de sistemas en el que no estén presentes los mismos. Por otra parte, el uso de agentes de sacrificio donadores de electrones puede también contribuir a aumentar el rendimiento del proceso de obtención de hidrogeno cuando se compara con el uso de agua pura. En este contexto, una propuesta atractiva para la obtención de hidrogeno renovable es el uso de disoluciones acuosas del bioalcoholes.

En esta tesis doctoral se han estudiado, en la producción fotocatalítica de hidrogeno a partir de disoluciones acuosas de etanol, tres sistemas distintos que no contienen metales nobles: sistemas híbridos organosilíceos mesoporosos conteniendo titanio (Ti-PMOs), sistemas laminares basados en C_3N_4 grafítico con Mo_xC ($Mo_xC/g\text{-}C_3N_4$), y sistemas basados en nanopartículas de TiO_2 anatasa con distintas formas y Mo_xC depositado (Mo_xC/TiO_2).

Todos los fotocatalizadores se han caracterizado usando distintas técnicas tales como: isotermas de adsorción/desorción de N_2, difracción de rayos X en polvo, espectroscopias infraroja, Raman y UV-Vis por reflectancia difusa, microscopia electrónica de barrido y de transmisión y espectroscopia fotoelectrónica de rayos X.

Además se han evaluado las propiedades fotoelectroquímicas de los materiales estudiados mediante espectroscopia de fotoluminiscencia y medidas de intensidad de corriente fotogenerada y espectroscopia de impedancia electroquímica.

Los materiales organosilíceos híbridos Ti-PMOs conteniendo grupos bifenil se han sintetizado utilizando microondas y han resultado mesoporosos con estructuras mesoscopicamente ordenadas. Se ha podido relacionar la presencia de Ti^{4+} tetraédrico en la estructura de los mismos con una menor velocidad de recombinación de las cargas fotogeneradas, una mayor facilidad en la transferencia de la carga y una mayor eficiencia fotocatalítica.

La preparación de fotocatalizadores $Mo_xC/g\text{-}C_3N_4$, con nanopartículas de MoC y/o Mo_2C de diferentes tamaños de cristalito en nanoláminas de $g\text{-}C_3N_4$ se ha realizado a partir de los precursores previamente sintetizados mediante la aplicación de ultrasonidos. Las características de las nanopartículas de Mo_xC determinan el comportamiento fotoelectroquímico de $Mo_xC/g\text{-}C_3N_4$ y en consecuencia su eficiencia fotocatalítica. El sistema que resulta más eficiente en la fotoproducción de hidrógeno es el que contiene simultáneamente hcp Mo_2C y fcc MoC.

Finalmente, se han utilizado nanopartículas de TiO_2 anatasa con distinta geometría (laminar y bipiramidal) para estudiar el efecto de la presencia de nanoparticulas de Mo_xC en el comportamiento de fotocatalizadores Mo_xC/TiO_2. Para ello se han utilizado nanopartículas de Mo_xC que se han depositado en TiO_2 bajo ultrasonidos. En todos los casos, Mo_xC actúa como un co-catalizador beneficioso, sin embargo su influencia depende de la geometría del TiO_2, concretamente se ha podido correlacionar la exposición de las caras (101) del semiconductor con unas mejores características fotoelectroquímicas y eficiencia fotocatalítica del sistema.

Ti-containing hybrid organosilicas, $Mo_xC/g\text{-}C_3N_4$ nanocomposites and engineered Mo_xC/TiO_2 nanomaterials as noble-metal-free photocatalysts for H_2 production

Contents

Chapter 1.

Introduction

1.1 Current hydrogen production and future trends

The global energy crisis is a significant bottleneck affecting the world's energy systems. Today, fossil fuels are still the world's primary energy source. However, fossil fuels are unrenewable resources because their formation takes millions of years and it is much slower than their consumption. At the same time, the use of fossil fuels gives rise to environmental problems. Approximately, two-thirds of global CO_2 emissions are coming from fossil fuel use [1]. Therefore, looking for suitable sustainable energy for electricity, heating, cooling, and power for transport is widely believed to be one of humanity's greatest challenges in the 21st century.

Hydrogen is considered of potential application for energy supply because it could be a sustainable, clean and versatile energy carrier. The hydrogen combustion heat (122 kJ/mol) is much higher than that of gasoline or other fossil fuels. Moreover, the energy density of hydrogen (120 MJ/kg) is almost three times higher than those of gasoline or diesel [2,3]. However, fossil fuels and steam reforming processes currently dominate the global production of hydrogen. Nowadays, natural gas, coal, water electrolysis and oil are the four main sources for commercial hydrogen production, which account for 76%, 23%, 1% and <0.1%, of total hydrogen production in the world, respectively, as shown in Figure 1.1 [4].

Depending on the source and the CO_2 emissions of the global process, the different methods of hydrogen production have radically different impacts on the environment. This has led to the proposal of a roadmap for future hydrogen production (Figure 1.1) [5,6].

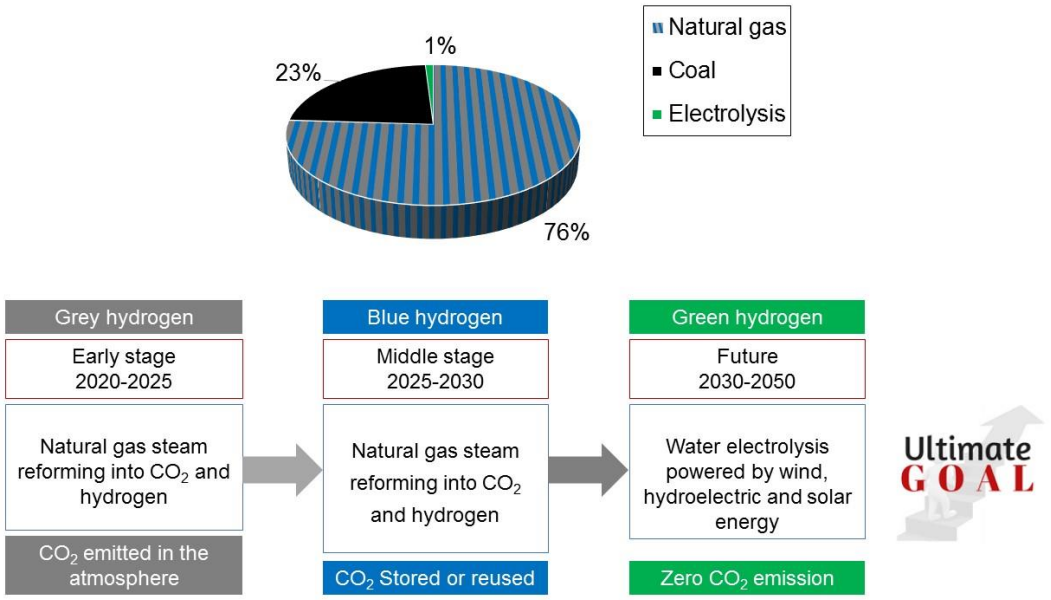

Figure 1.1. Sources of current hydrogen production (70 Mt/year) and 2020-2050 roadmap [5,6].

The electrolysis of water into its components, oxygen and hydrogen, is an appealing greenway for hydrogen production with zero CO_2 emission. Nowadays, almost 8 GW of electrolysis capacity is used worldwide, accounting for about 1% of the global hydrogen production [6]. However, the energy efficiency for converting electricity to hydrogen and the capital cost of the electrolyzer unit are currently two main barriers to further expand the electrolysis method to produce hydrogen. Moreover, the CO_2 emission in the generation of the necessary electricity should be avoided using renewable energy sources [7].

The photocatalytic hydrogen production using solar energy, which has been extensively studied in the last decade, is another method to achieve clean and renewable hydrogen [8]. This process is driven by a photocatalyst suspended directly in water, instead of using an electrolytic device, and could convert solar energy into chemical energy using electrons and protons from

water. This approach can be considered as a future option of potential application in the long term.

1.2 Photocatalytic hydrogen production

In the year of 1972, Fujishima and Honda [9] firstly reported the use of TiO_2 for the photocatalytic splitting of water and UV light-induced hydrogen production. After that, photocatalytic hydrogen production has attracted significant attention all around the world.

The process of solar energy conversion into chemical energy through photocatalytic water splitting involves a largely positive change in the Gibbs free energy. The overall photocatalytic water-splitting reaction is a typical uphill reaction (Figure 1.2) with ΔG^0 of 237 kJ/mol, as shown in Figure 1.2 and equations 1.1-1.3:

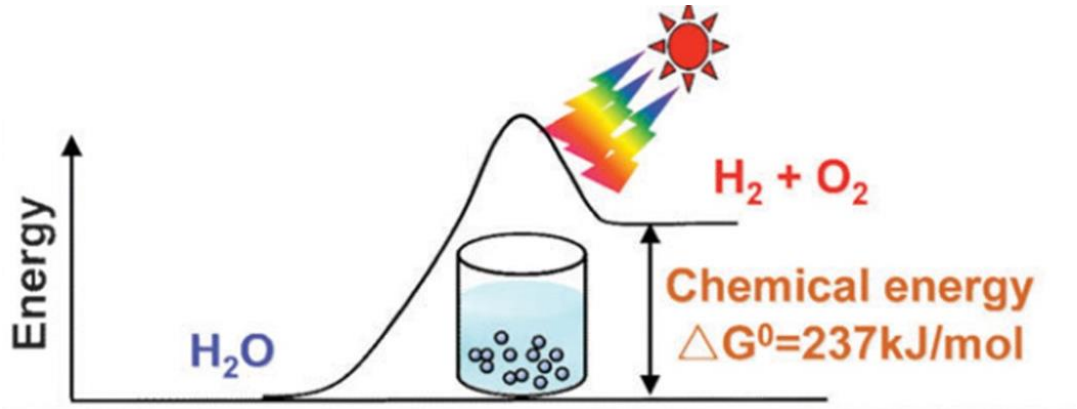

Figure 1.2. Gibbs free energy of the photocatalytic water splitting process [10]. Reproduced by permission of RSC.

$$H_2O \rightarrow \frac{1}{2}O_2 + H_2 \qquad E^0 = 1.23\ V \qquad \Delta G^0 = 237\ kJ/mol \qquad \textbf{1.1}$$

$$2H^+ + 2e^- \rightarrow H_2 \qquad E^0 = 0.00\ V \qquad \textbf{1.2}$$

$$2H_2O \rightarrow O_2 + 4H^+ + 4e^- \qquad E^0 = 1.23\ V \qquad \textbf{1.3}$$

It indicates that the incident photon energy needs to be larger than 1.23 eV, which corresponds to wavelengths lower than 1010 nm; thus, 70 % of total solar radiation can be theoretically available for water splitting [11].

Water itself cannot directly absorb light from sunshine to automatically carry out the photocatalytic water splitting process; however, the process can be achieved in the presence of an appropriate photocatalyst.

Usually, photocatalytic hydrogen production is carried out in the heterogeneous phase, using a semiconductor with a suitable energy bandgap (Eg) [12,13]. The semiconductor used as photocatalyst has a central role in the efficiency of the whole process [12-14]. As shown in Figure 1.3, the overall photocatalytic hydrogen production can be summarized into three main processes. Firstly, incident photons with energy equal to or larger than the bandgap energy of the semiconductor are absorbed to produce electron-hole pairs in the semiconductor. Then, the photogenerated electrons and holes move from bulk to the surface of the photocatalyst. Finally, the photogenerated electrons reduce H^+ into H_2; in the meanwhile, H_2O is oxidized into O_2 by photogenerated holes [10]. However, electrons and holes can easily recombine during the second step, then a poor photocatalytic activity for overall hydrogen production reaction occurs. This effect could be minimized by the presence of appropriate co-catalysts [15].

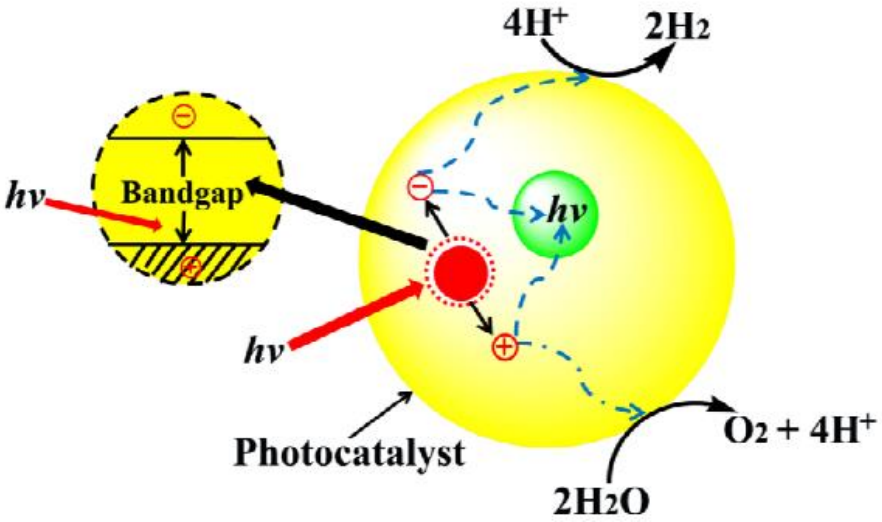

Figure 1.3. Schematic representation of semiconductors for water splitting [16]. Reproduced by permission of RSC.

The essential parameter that governs the light-harvesting ability of the photocatalyst is its electronic structure, which determines its Eg. The conduction band (CB) edge of the catalyst should be more negative than the reduction potential of H^+ to H_2 (0.00 V), while the valence band (VB) edge should be more positive than the oxidation potential of H_2O to O_2 (1.23 V).

TiO_2 has been investigated widely as a photocatalyst not only for hydrogen production but also for CO_2 reduction due to its unique chemical and physical properties [17,18]. TiO_2 is cheap, nontoxic and it has high stability, durability and affordability [19]. Rutile and anatase are the most studied TiO_2 crystalline phases with Eg of 3.0 and 3.2 eV, respectively [17]; therefore, they show photocatalytic UV-visible response. Figure 1.4 shows the schematic illustration of water splitting on anatase which is the most photocatalytically active TiO_2 crystalline phase. In this case, an incident radiation with a wavelength shorter than 387 nm is necessary for its photoactivation.

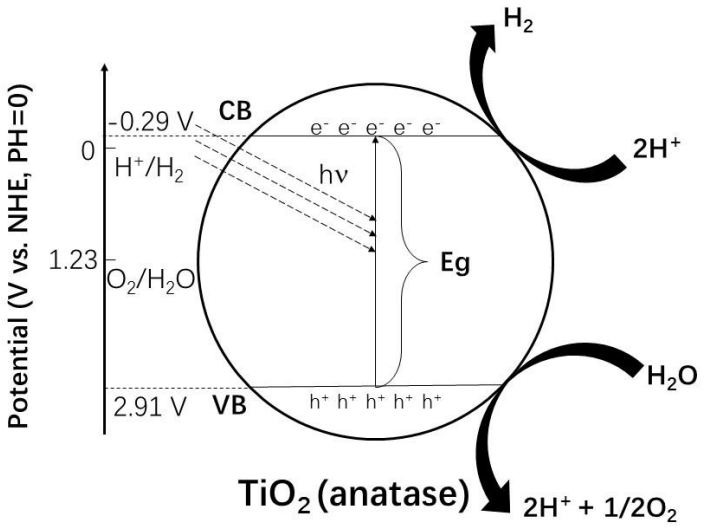

Figure 1.4. Schematic illustration of the photocatalytic hydrogen generation on anatase TiO_2 [20].

In addition to the crystal structure, the characteristic of the exposed surface to the reactants is a crucial factor, which has been demonstrated to influence the global photocatalytic performance of the material [21].

Besides TiO_2, a wide variety of oxide and metal sulfide semiconductor materials have been explored as photocatalysts for H_2 production [22]. Oxide materials such as ZnO [23], $KTaO_3$ [24], $SrTiO_3$ [25] and WO_3 [26] have been used under ultraviolet irradiation. Otherwise, CdS is an interesting candidate for photocatalytic hydrogen production because of its suitable band position and bandgap value, allowing visible light response; visible light is the main component of solar light radiation reaching earth [27]. However, when CdS is used for water splitting, photo corrosion always happens because S^{2-} in CdS rather than H_2O is oxidized by photogenerated holes. To avoid this process, the addition of sacrificial electron donors (SEDs) as hole scavengers are proposed [28].

In the past decade, a variety of materials such as organic polymeric semiconductors, 2D-graphitic carbon nitride (g-C_3N_4) and 3D-ordered mesoporous materials have been used as photocatalysts for hydrogen production [29-34].

Taking into account the content of this thesis, the 1.3 section is devoted to different relevant aspects related with the use of TiO_2, g-C_3N_4 and several Ti-containing ordered mesoporous materials as photocatalysts. Moreover, the role of co-catalysts in the photocatalytic performance and the addition of SEDs are discussed below (1.2.1 and 1.2.2 sections). In addition, the 1.4 section introduces the photocatalytic CO_2 reduction, because the ordered mesoporous materials developed in this work were tested in both, photocatalytic hydrogen production and CO_2 photoreduction.

1.2.1 The role of co-catalysts

As mentioned above, the fast recombination of photogenerated electron-hole pairs is the main problem affecting the efficiency of a semiconductor used as photocatalyst. The utilization of co-catalysts can promote the separation of photogenerated charges and suppress the charge recombination by extracting photogenerated electrons and/or holes [15].

Moreover, an appropriate co-catalyst doped onto a semiconductor can decrease the overpotential or activation energy of the photocatalytic reaction and can avoid photo-corrosion to improve the durability of semiconductors [15,35].

The content, particle size and crystal structure of the co-catalyst in the photocatalyst can impact the photocatalytic performance [15]. Usually, a volcano-type relationship between the amount of co-catalyst and the photocatalytic activity of the system is observed (Figure 1.5). Furthermore,

different reports indicate that a small size and a high dispersion of the co-catalyst significantly favor the efficiency of the system [36-38].

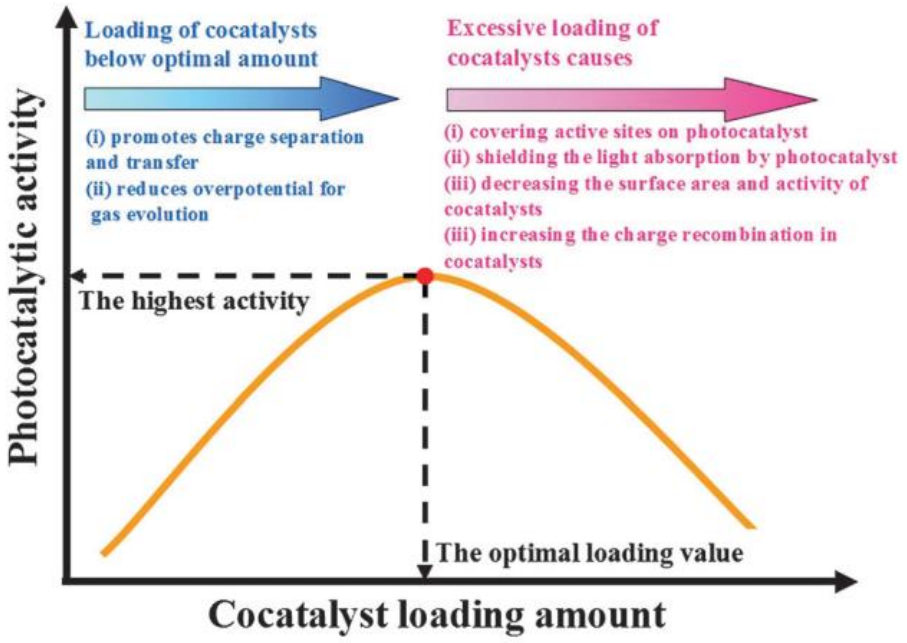

Figure 1.5. The general relationship between the amount of a given co-catalyst and the photocatalytic activity of the system [15]. Reproduced by permission of RSC.

Noble metals such as Pt [39,40]**,** Pd [41,42], Au [43,44], Ag [45,46], Ru [47,48] and Rh [49,50] have been reported as co-catalysts for photocatalytic hydrogen evolution and/or CO_2 reduction, being Pt the most commonly used. When the photogenerated electron migrates to the surface of the host semiconductor, it can be entrapped by the noble metal, which has a lower Fermi energy level than the host semiconductor. The Schottky barrier formed, after dopping the semiconductor with the noble metal, decreases the hole/electron recombination, contributing to increasing the photocatalytic yield [15,35]. However, the high cost and scarcity of noble metals are the main barriers to their application as co-catalysts.

In recent years, cheaper and earth-abundant co-catalysts with high efficiency and high selectivity have been studied [15]. Transition metal oxides, sulfides and carbides have been demonstrated to be effective co-catalysts, enhancing the efficiency of the photocatalytic process. Kumar et al. have reported a highly efficient CuO/TiO_2 photocatalyst for H_2 evolution from a water-glycerol mixture under natural sunlight irradiation [51]. The efficiency is mainly related with the nanotubular morphology of TiO_2 and the quantum size of CuO used as co-catalyst, the uni-directional electron flow and capture at the Schottky barrier would facilitate the charge separation and electron transfer [51].

As stated above, transition metal carbides could be considered appropriate candidates to be used as co-catalysts because they exhibit metallic characteristics and show platinum-like catalytic properties. Garcia-Esparza et al. have demonstrated the co-catalyst effect of tungsten carbide nanoparticles onto a Na-doped $SrTiO_3$ for the water-splitting [52]. More recently, we have reported the role of WC as co-catalyst onto TiO_2 in the photocatalytic hydrogen production from ethanol aqueous solutions [53]. Besides WC, Mo_xC has been also used as co-catalyst onto several semiconductors such as TiO_2, CdS and $SrTiO_3$ for photocatalytic H_2 production [54-57]. In this context, it has been recently reported the use of different g-C_3N_4-based photocatalysts containing Mo_2C for photocatalytic H_2 production: Mo-Mo_2C modified g-C_3N_4 [58], Mo_2C@C/g-C_3N_4 heterostructure [59,60], and rod-like g-C_3N_4 decorated with Mo_2C [61]. In these reports, different routes have been used for both the preparation of the molybdenum carbide system and the integration onto the g-C_3N_4 semiconductor, in all cases, aqueous solutions of triethanolamine (TEOA) have been used as SED.

1.2.2 The role of SEDs

As stated above, in a true photocatalytic water splitting, hydrogen is generated through the reduction process and oxygen is generated through the oxidation process. However, the oxidation process is especially slow and often the bottleneck of the whole water-splitting process. In order to improve the photocatalytic efficiency of the process, some organic compounds are added as SEDs. In a photocatalytic process, the main task of a SED is to avoid the recombination of the photogenerated electrons and holes, playing the role of electron donors or electron-acceptor scavengers. Pellegrin and Odobel have reviewed the use of SEDs in photocatalytic reactions and have detailed the mechanism of different sacrificial reagents' performance and thermodynamic considerations [62].

Typical SEDs are alcohols, amines and organic acids, among others. Galinska and Walendziewski had compared the use of EDTA, Na_2S and methanol as SEDs in the water splitting over Pt-TiO_2 under UV irradiation. The highest photocatalytic efficiency was achieved when methanol was employed [63]. More recently, Scaiano et al. compared several TiO_2-based catalysts in true water splitting (no SED), methanol- and formate-assisted hydrogen photogeneration, they found that the performance of photocatalysts in true water splitting or SED-assisted systems can not be simply transferred [28].

Ethanol has been also used as SED for photocatalytic H_2 production in different studies [53,64-67]. Nowadays, ethanol is the biofuel produced in the largest amount worldwide [68]. Moreover, during the photocatalytic process ethanol can be transformed into interesting intermediate products [66, 67].

If the photoreforming process of aqueous ethanol would be completed, only CO_2 and H_2 could be obtained:

$$CH_3CH_2OH + 3H_2O + 12h^+ \rightarrow 2CO_2 + 12H^+ \quad \textbf{1.4}$$

$$12H^+ + 12e^- \rightarrow 6H_2 \quad \textbf{1.5}$$

However, acetaldehyde, acetic acid and 2,3-butanediol, as partially oxidized intermediate products, can be found in the final solution after the photocatalytic process [67]:

$$CH_3CH_2OH + h^+ \rightarrow \bullet CH(OH)CH_3 + H^+ \quad \textbf{1.6}$$

$$\bullet CH(OH)CH_3 + h^+ \rightarrow CH_3CHO + H^+ \quad \textbf{1.7}$$

$$CH_3CHO + H_2O + 2h^+ \rightarrow CH_3COOH + 2H^+ \quad \textbf{1.8}$$

$$2\bullet CH(OH)CH_3 \rightarrow CH_3CH(OH)CH(OH)CH_3 \quad \textbf{1.9}$$

1.3 Several specific systems as photocatalysts

1.3.1 Shape-engineered TiO_2

The fabrication of TiO_2 with specific morphologies and exposed facets has emerged as a promising way to improve TiO_2 quantum yield [18,69]. Specifically, anatase TiO_2 nanocrystals with different exposed facets have been developed and some of them have demonstrated enhanced photocatalytic performance [70-72]. The different exposed facets of anatase TiO_2 can slightly tune the surface free energy and electronic band structure [73]. Moreover,

different facets of anatase TiO_2 can drive photogenerated electrons or holes [74-76]. Some researches indicate that anatase (001) facets possess lower thermodynamic stability and higher reactivity due to their high density of unsaturated titanium and active surface oxygen species [77,78]. Besides, the role of the anatase (101) facet in producing and separating electron-hole pairs during the photoexcitation has been demonstrated [79,80].

Anatase (101) facet plays a critical role in CO_2 adsorption, facilitating the transfer of the photogenerated electron from the surface of TiO_2 to CO_2 during the photocatalytic CO_2 reduction [81]. In the water splitting, the (101) facet also increases the rate of H_2 photoproduction because favors the electron transfer to water [82].

TiO_2 single crystals could facilitate the directional moving of photogenerated electrons and holes to different surfaces, resulting in an obviously decreased recombination rate [83-85]. For anatase, experimental and theoretical researches point to the preference of moving photogenerated electrons to low-energy (101) facets, while holes preferably migrate to high-energy (001) facets [86-88]. Thus, a co-exposition of (001) and (101) facets could improve the photocatalytic behaviour in comparison to each facet alone [76].

On the other hand, the photocatalytic behaviour of anatase TiO_2 nanoparticles depends not only on the facets exposed but also on the post-synthesis treatment, which can determine physicochemical properties, such as hydrophilicity and Lewis acidity, and then influence on the photocatalytic behaviour [89].

1.3.2 g-C_3N_4-based systems

The morphologic architecture of the photocatalyst regulated by dimensionality can be considered as a useful strategy, which could give rise to an improvement of photocatalytic efficiency [90]. Several 2D materials have received interest in photocatalytic hydrogen production due to their unique ability for confining electrons in their ultrathin layer, resulting in exceptional optical and electronic properties [91].

g-C_3N_4 is a layered material with significant electrical and optical properties, which has been used in different photocatalytic reactions. g-C_3N_4 is a family of metal-free polymeric semiconductors based on triazine- or heptazine units [30-32,92-94]. The heptazine-based layered crystalline structure of g-C_3N_4 is shown in Figure 1.6.

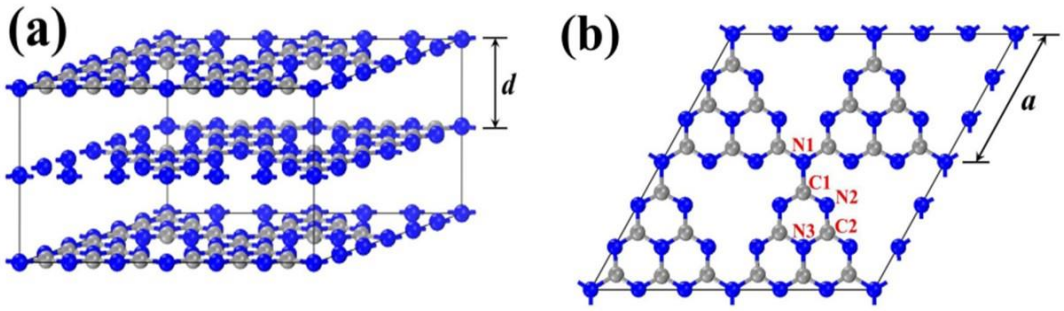

Figure 1.6. Structure diagram of heptazine-based g-C_3N_4 [95]. 2017 Elsevier B.V. All rights reserved.

Bulk g-C_3N_4 is thermically stable, shows very high resistance to the attack of strong acid and alkaline solutions and has a visible light response with a bandgap of 2.7 eV [30]. However, the use of bulk g-C_3N_4 in photocatalysis is limited by the fast recombination of the photoinduced electron-hole pairs. New fabrication strategies and structure modification of g-C_3N_4 have given significant breakthroughs for its application in photocatalysis [96-100]. For

instance, Yang et al. have reported a method to create nitrogen vacancies on g-C_3N_4; the nitrogen vacancies sites are active for the photocatalytic oxygen evolution reaction, promoting the separation and transfer of the photogenerated charge carrier [99]. A higher crystallinity of g-C_3N_4 has been related with a higher light absorption and a faster electron transfer, which results in a higher photoactivity under visible-light irradiation [100]. Hou et al. constructed a layered MoS_2 on g-C_3N_4 photocatalyst with thin and planar interfaces in MoS_2/g-C_3N_4, which is proposed to play a key role in improving photocatalytic activity. This photocatalyst showed a better photocatalytic behaviour under visible light irradiation than Pt/g-C_3N_4 [38] (Figure 1.7).

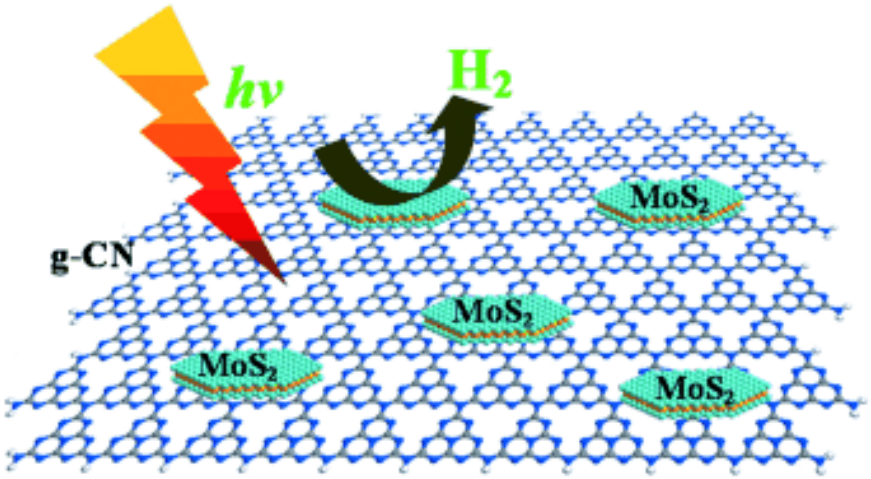

Figure 1.7. Schematic illustration of the photocatalytic H_2 production process over MoS_2-loaded g-C_3N_4 under visible-light irradiation [38]. Copyright (2013) WILEY‐VCH.

1.3.3 Several Ti-containing ordered mesoporous materials

The high surface area, uniform porous array and long-range structure of ordered mesoporous materials make them attractive candidates to be used as photocatalysts [101]. Several Ti-containing porous materials based on zeolites, metal-organic frameworks (MOF), and periodic mesoporous organosilicas

(PMOs) have been applied in photocatalytic reactions. These materials with periodic porous structure show high specific surface area, tunable porosities and dimensionalities, which could capture different substrates into their cavities and show a high dispersion of catalytic active sites [102-104].

Zeolite-based materials, as the traditional porous materials, were early utilized in photocatalytic processes. Anpo et al. reported TiO_2 species as the active sites introduced into the structure of mesoporous zeolites (Ti-MCM-41 and Ti-MCM-48) for the photocatalytic CO_2 reduction with water. The main products were CH_4 and CH_3OH, exhibiting a high selectivity for the CH_3OH generation and almost 10 times higher photocatalytic efficiency for CH_4 generation than bulk TiO_2 [105-107].

Ti-containing MOFs have also been used for the photoreduction of CO_2 [108]. In these systems, the capability of transferring the photogenerated electrons avoiding the electron-hole recombination is of main importance; a strong ligand-metal charge transfer (LMCT) could avoid the recombination of photoinduced electron-hole pairs, favoring the photocatalytic action of the material [109].

PMOs are another series of organic-inorganic materials possessing periodically ordered pores with 2-10 nm width and nanometer-thick pore walls made of organosilica [110-113]. In PMOs, $O_{1.5}$-Si-R-Si-$O_{1.5}$ units, covalently bonded, are forming the pore walls. Organic donor or acceptor moieties can be incorporated within the PMO framework, and this can allow the construction of appropriate photocatalysts, which show larger void spaces for mass transfer than those of mesoporous silicas [114]. The presence of π-conjugated bridging groups could make these materials appropriate for light absorption, harvesting, and photo-induced electron and hole transportation [115-117]. Biphenyl-bridged hybrid PMOs with crystal-like ordering of walls have been synthesized

by the self-assembly hydrothermal method and show both periodic ordered mesoporosity and periodicity at a molecular level [118,119].

PMOs can be also modified with different heteroatoms to improve different properties [120,121]. The titanium introduction into PMO could improve the photocatalytic behaviour. In this context, Ti-containing ethane-bridged PMOs used as photocatalysts for olefin conversion have shown improved epoxide selectivity [122].

1.4 Photocatalytic CO_2 reduction

It is well-known the contribution of CO_2 emissions to the greenhouse effect. It is reported that since the pre-industrial period, the average global temperature has increased by around 1 °C [123]. The development of the world economy mainly relies on the consumption of fossil fuels, which is considered the main source of CO_2. Figure 1.8 presents the huge increase in CO_2 emissions from 1900 [124].

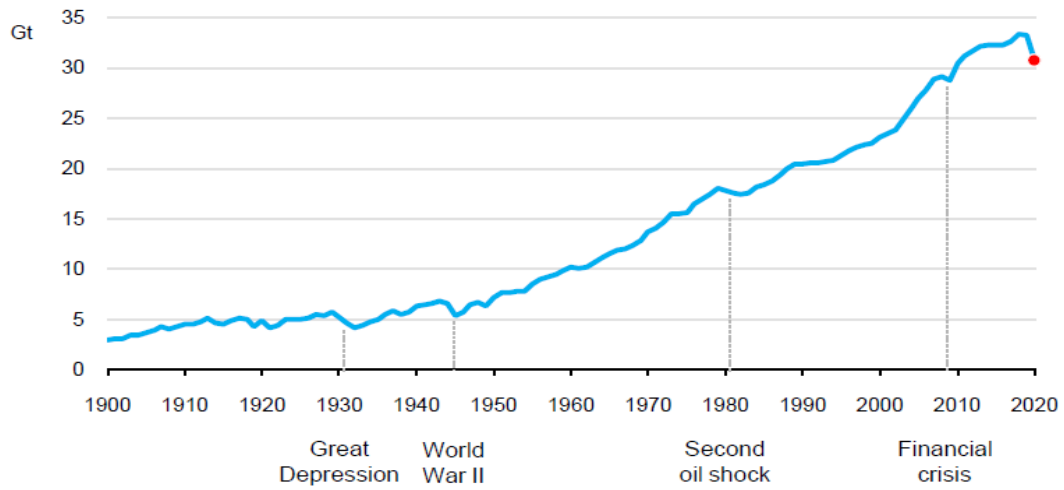

Figure 1.8. Global CO_2 emissions from 1900 to 2020. (Gigatonnes of CO_2 per year) Source: Global Carbon Project, CDIAC, and IEA. [124] IEA. All Rights Reserved.

CO_2 capture, storage and conversion into fuels or valuable chemicals can play a main role in the decrease of CO_2 emissions.

In the long term, direct photocatalytic conversion is one of the more promising research fields into CO_2 recycling. Under this concept, CO_2 could be considered a green molecule from which, through renewable solar energy, desirable chemical products and fuels could be sustainably obtained.

Since the early report by Halmann in 1978, the photocatalytic CO_2 reduction with water into hydrocarbons, by solar energy as the driving force, has attracted much attention [125-127]. The fundamentals of photocatalytic CO_2 reduction are similar to those of photocatalytic H_2 production [128]. Both, H^+ and CO_2 reduction, make use of photogenerated e^- in the CB of a semiconductor. In parallel, to make the process catalytic, an e^- donor must be provided to scavenge h^+ in the VB, reducing the charge recombination in the semiconductor (Figure 1.9).

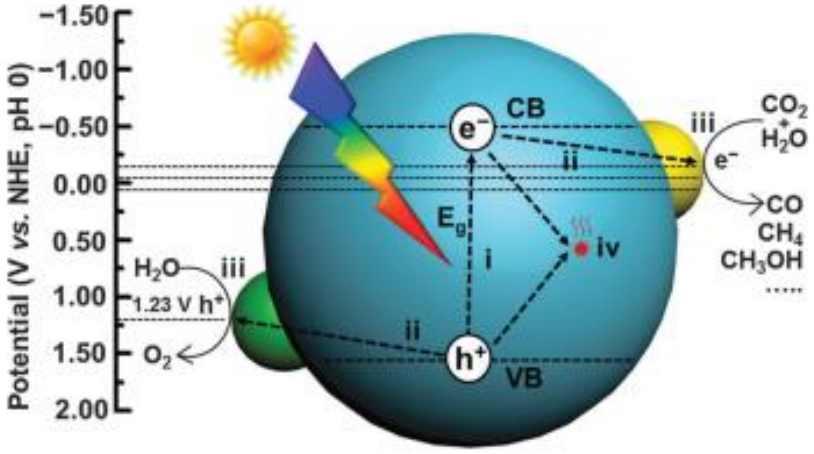

Figure 1.9. Scheme of elementary steps occurring in photocatalytic CO_2 reduction with water over a heterogeneous photocatalyst [129]. Reproduced by permission of RSC.

In order to achieve the photocatalytic CO_2 reduction to CO or other value-added chemicals, electrons generated in the semiconductor are required to have more negative chemical potential; meanwhile, holes need to lie on the more positive potential level than the water oxidation process. Eqs. 1.10–1.17

illustrate different CO_2 photoreduction processes in H_2O and the corresponding potentials at pH = 7 [130].

Reactions	**E^0 (V vs. NHE)**	
$CO_2 + e^- \rightarrow \bullet CO_2^-$	−1.90	**1.10**
$CO_2 + 2H^+ + 2e^- \rightarrow HCOOH$	−0.61	**1.11**
$CO_2 + 2H^+ + 2e^- \rightarrow CO + H_2O$	−0.53	**1.12**
$CO_2 + 4H^+ + 4e^- \rightarrow HCHO + H_2O$	−0.48	**1.13**
$CO_2 + 6H^+ + 6e^- \rightarrow CH_3OH + H_2O$	−0.38	**1.14**
$CO_2 + 8H^+ + 8e^- \rightarrow CH_4 + 2H_2O$	−0.24	**1.15**
$2H_2O + 4h^+ \rightarrow O_2 + 4H^+$	+0.81	**1.16**
$2H^+ + 2e^- \rightarrow H_2$	−0.42	**1.17**

The low conversion efficiency is still the greatest drawback of the photocatalytic CO_2 reduction with H_2O in the presence of solar light radiation. Following, a number of crucial points, which limit the efficiency are presented: (1) mismatching between the absorption ability of semiconductor and the solar spectrum; (2) poor separation efficiency of charge carriers; (3) low solubility of CO_2 in H_2O (approximately 33 µmol in 1 ml of water at 100 kPa and room temperature); (4) back reactions during photocatalytic CO_2 reduction; (5) competition of CO_2 reduction and photocatalytic hydrogen evolution [131-133]. In order to increase the photoreaction efficiency, this process is carried out in the presence of SEDs. Several organic compounds such as formic acid and methanol are used as SEDs for the photocatalytic CO_2 reduction. They are

used as hole scavengers but they can also increase the solubility of CO_2. However, carbon-containing products and H_2 are produced from typical SEDs under CO_2 photoreduction conditions [28]. Moreover, SEDs can achieve photolysis in the absence of photocatalyst [134]. Therefore, an appropriate study of SED evolution during the photocatalytic reduction is mandatory for a proper analysis of the results.

1.5 Objectives and structure of the thesis

Taking into account the above-mentioned background, this thesis aims to design, prepare and study new photocatalysts for H_2 production from ethanol aqueous solution. Three different materials have been developed: Ti-containing periodic mesoporous organosilicas (Ti-PMOs), $Mo_xCT/g\text{-}C_3N_4$ nanocomposites with different Mo_xC as co-catalysts on graphitic C_3N_4, and Mo_xC/TiO_2-X photocatalysts containing shape-engineered anatase nanoparticles and Mo_xC as co-catalyst.

In all cases, the main goal is the preparation and characterization of materials in order to relate their characteristics to the photocatalytic behaviour. The specific objectives of this work are:

- Preparation and characterization of new Ti-PMOs hybrid periodically ordered mesoporous organosilicas with biphenyl moieties and Ti(IV) species. Study of Ti-PMOs in the photocatalytic H_2 production from $ethanol_{(aq)}$. Test Ti-PMOs in the photocatalytic CO_2 reduction in the presence of TEOA as SED. (**Chapter 3**)

- Preparation and characterization of new $Mo_xCT/g\text{-}C_3N_4$ with Mo_2C and/or MoC phases with different crystallite size. Study of $Mo_xCT/g\text{-}C_3N_4$ in the H_2 production from $ethanol_{(aq)}$ under visible light irradiation. (**Chapter 4**)

- Preparation and characterization of new Mo_xC/TiO_2(NS)-X and Mo_xC/TiO_2(bipy) photocatalysts using anatase TiO_2 nanosheets with dominant (001) facets and anatase TiO_2 nanoparticles with bipyramidal shape, and, different Mo_xC nanoparticles previously synthesized. Study of Mo_xC/TiO_2(NS)-X and Mo_xC/TiO_2(bipy) in the photocatalytic H_2 production from ethanol$_{(aq)}$. (**Chapter 5**)

Besides the above-mentioned chapters (**Chapter 3-5**) in which the main results obtained are presented and discussed, in the present **Chapter 1**, the background, which motivated this work is presented. **Chapter 2** describes the different techniques and methods used in the characterization of catalysts; in addition, the reaction system used for the photocatalytic tests and the analysis of reaction products are reported. Finally, in **Chapter 6** the most relevant conclusions of this thesis are summarized.

1.6 References

1. https://iea.blob.core.windows.net/assets/3a2ed84c-9ea0-458c-9421-d166a9510bc0/GlobalHydrogenReview2021.pdf. Global Hydrogen Review 2021, 2021. (Accessed on 10 October 2021)
2. Abdalla A M, Hossain S, Nisfindy O B, et al. Hydrogen production, storage, transportation and key challenges with applications: A review. Energy Conversion and Management, 2018, 165: 602-627..
3. Dawood F, Anda M, GM Shafiullah. Hydrogen production for energy: An overview. International Journal of Hydrogen Energy, 2020, 45: 3847-3869.
4. Santhanam K S V, Press R J, Miri M J, et al. Introduction to hydrogen technology. John Wiley & Sons, 2017.

5. https://aureliaturbines.com/articles/for-the-green-deal-hydrogen-also-needs-to-be-green. For the Green Deal, hydrogen also needs to be green, 2019. (Accessed on 16 Septemper 2021)
6. https://www.iea.org/reports/the-future-of-hydrogen. The Future of Hydrogen, 2019, IEA, Paris. (Accessed on 5 Septemper 2021)
7. Shibata Y. Economic Analysis of Hydrogen Production from Variable Renewables. IEEJ Energy Journal, 2015, 10: 26-46.
8. Hisatomi T, Domen K. Reaction systems for solar hydrogen production via water splitting with particulate semiconductor photocatalysts. Nature Catalysis, 2019, 2: 387–399.
9. Fujishima A, Honda K. Electrochemical photolysis of water at a semiconductor electrode. Nature, 1972, 238: 37-38.
10. Kudo A, Miseki Y. Heterogeneous photocatalyst materials for water splitting. Chemical Society Reviews, 2009, 38: 253-78.
11. Navarro Yerga R M, Álvarez Galván M C, Del Valle F, et al. Water splitting on semiconductor catalysts under visible‐light irradiation. ChemSusChem, 2009, 2: 471-485.
12. Hoffmann M R, Martin S T, Choi W, et al. Environmental applications of semiconductor photocatalysis. Chemical Reviews, 1995, 95: 69-96.
13. Henderson M A. A surface science perspective on TiO_2 photocatalysis. Surface Science Reports, 2011, 66: 185-297.
14. Serpone N, Emeline A V. Semiconductor photocatalysis-Past, present, and future outlook. The Journal of Physical Chemistry Letters, 2012, 3: 673-677.
15. Ran J, Zhang J, Yu J, et al. Earth-abundant cocatalysts for semiconductor-based photocatalytic water splitting. Chemical Society Reviews, 2014, 43: 7787-7812.
16. Yuan Y J, Chen D, Yu Z T, et al. Cadmium sulfide-based nanomaterials for photocatalytic hydrogen production. Journal of Materials Chemistry A, 2018,

6: 11606-11630.

17. Habisreutinger S N, Schmidt‐Mende L, Stolarczyk J K. Photocatalytic reduction of CO_2 on TiO_2 and other semiconductors. Angewandte Chemie International Edition, 2013, 52: 7372-7408.

18. Tian J, Zhao Z, Kumar A, et al. Recent progress in design, synthesis, and applications of one-dimensional TiO_2 nanostructured surface heterostructures: a review. Chemical Society Reviews, 2014, 43: 6920-6937.

19. Dhakshinamoorthy A, Navalon S, Corma A, et al. Photocatalytic CO_2 reduction by TiO_2 and related titanium containing solids. Energy & Environmental Science, 2012, 5:9217-9233.

20. Yi M, Wang X, Jia Y, et al. Titanium Dioxide-Based Nanomaterials for Photocatalytic Fuel Generations. Chemical Reviews, 2014, 114: 9987-10043.

21. Liu S, Yu J, Jaroniec M. Anatase TiO_2 with dominant high-energy {001} facets: synthesis, properties, and applications. Chemistry of Materials, 2011, 23: 4085-4093.

22. Wang Z, Li C, Domen K. Recent developments in heterogeneous photocatalysts for solar-driven overall water splitting. Chemical Society Reviews, 2019, 48: 2109-2125.

23. Gomathisankar P, Hachisuka K, Katsumata H, et al. Photocatalytic Hydrogen Production from Aqueous Na_2S + Na_2SO_3 Solution with B-Doped ZnO. ACS Sustainable Chemistry & Engineering, 2013, 1: 982-988.

24. Bajorowicz B, Nadolna J, Lisowski W, et al. The effects of bifunctional linker and reflux time on the surface properties and photocatalytic activity of CdTe quantum dots decorated $KTaO_3$ composite photocatalysts. Applied

Catalysis B: Environmental, 2017, 203: 452-464.

25. Takata T, Jiang J, Sakata Y, et al. Photocatalytic water splitting with a quantum efficiency of almost unity. Nature, 2020, 581: 411-414.
26. Xie Y P, Liu G, Yin L, et al. Crystal facet-dependent photocatalytic oxidation and reduction reactivity of monoclinic WO_3 for solar energy conversion. Journal of Materials Chemistry, 2012, 22: 6746-6751.
27. Zhu N, Tang J, Tang C, et al. Combined CdS nanoparticles-assisted photocatalysis and periphytic biological processes for nitrate removal. Chemical Engineering Journal, 2018, 353: 237-245.
28. Hainer A S, Hodgins J S, Sandre V, et al. Photocatalytic hydrogen generation using metal-decorated TiO_2: sacrificial donors vs true water splitting. ACS Energy Letters, 2018, 3: 542-545.
29. Wang Y, Vogel A, Sachs M, et al. Current understanding and challenges of solar-driven hydrogen generation using polymeric photocatalysts. Nature Energy, 2019, 4: 746-760
30. Kumar S, Karthikeyan S, Lee A F. g-C_3N_4-based nanomaterials for visible light-driven photocatalysis. Catalysts, 2018, 8: 74.
31. Ong W J, Tan L L, Ng Y H, et al. Graphitic carbon nitride (g-C_3N_4)-based photocatalysts for artificial photosynthesis and environmental remediation: are we a step closer to achieving sustainability? Chemical Reviews, 2016, 116: 7159-7329.
32. Fu J, Yu J, Jiang C, et al. g-C_3N_4-Based heterostructured photocatalysts. Advanced Energy Materials, 2018, 8: 1701503.
33. Park S S, Moorthy M S, Ha C S . Periodic mesoporous organosilica (PMO) for catalytic applications. Korean Journal of Chemical Engineering, 2014, 31: 1707-1719.
34. Matsuoka M, Anpo M, Local Structures, Excited States, and Photocatalytic reactivities of highly dispersed catalysts constructed within zeolites, Journal

of Photochemistry and Photobiology C: Photochemistry Reviews, 2003, 3: 225-252.

35. Yang J, Yan H, Zong X, et al. Roles of cocatalysts in semiconductor-based photocatalytic hydrogen production. Philosophical Transactions of the Royal Society A: Mathematical, Physical and Engineering Sciences, 2013, 371: 20110430.
36. Yu J, Ran J. Facile preparation and enhanced photocatalytic H_2-production activity of $Cu(OH)_2$ cluster modified TiO_2. Energy & Environmental Science, 2011, 4: 1364-1371.
37. Yu J, Hai Y, Cheng B. Enhanced photocatalytic H_2-production activity of TiO_2 by $Ni(OH)_2$ cluster modification. The Journal of Physical Chemistry C, 2011, 115: 4953-4958.
38. Hou Y, Laursen A B, Zhang J, et al. Layered nanojunctions for hydrogen‐evolution catalysis. Angewandte Chemie International Edition, 2013, 125: 3709-3713.
39. Lingampalli S R, Gautam U K, Rao C N R. Highly efficient photocatalytic hydrogen generation by solution-processed ZnO/Pt/CdS, ZnO/Pt/$Cd_{1-x}Zn_xS$ and ZnO/Pt/$CdS_{1-x}Se_x$ hybrid nanostructures. Energy & Environmental Science, 2013, 6: 3589-3594.
40. Gao G, Jiao Y, Waclawik E R, et al. Single atom (Pd/Pt) supported on graphitic carbon nitride as an efficient photocatalyst for visible-light reduction of carbon dioxide. Journal of the American Chemical Society, 2016, 138: 6292-6297.
41. Sayed F N, Jayakumar O D, Sasikala R, et al. Photochemical hydrogen generation using nitrogen-doped TiO_2–Pd nanoparticles: facile synthesis and effect of Ti^{3+} incorporation. The Journal of Physical Chemistry C, 2012, 116: 12462-12467.
42. Bai S, Wang X, Hu C, et al. Two-dimensional g-C_3N_4: an ideal platform for

examining facet selectivity of metal co-catalysts in photocatalysis. Chemical communications, 2014, 50: 6094-6097.

43. Murdoch M, Waterhouse G I N, Nadeem M A, et al. The effect of gold loading and particle size on photocatalytic hydrogen production from ethanol over Au/TiO_2 nanoparticles. Nature Chemistry, 2011, 3: 489-492.
44. Cao L, Sahu S, Anilkumar P, et al. Carbon nanoparticles as visible-light photocatalysts for efficient CO_2 conversion and beyond. Journal of the American Chemical Society, 2011, 133: 4754-4757.
45. Onsuratoom S, Puangpetch T, Chavadej S. Comparative investigation of hydrogen production over Ag-, Ni-, and Cu-loaded mesoporous-assembled TiO_2–ZrO_2 mixed oxide nanocrystal photocatalysts. Chemical Engineering Journal, 2011, 173: 667-675.
46. Li K, Peng T, Ying Z, et al. Ag-loading on brookite TiO_2 quasi nanocubes with exposed {210} and {001} facets: Activity and selectivity of CO_2 photoreduction to CO/CH_4. Applied Catalysis B: Environmental, 2016, 180: 130-138.
47. Tsuji I, Kato H, Kudo A. Visible‐light‐induced H_2 evolution from an aqueous solution containing sulfide and sulfite over a ZnS–$CuInS_2$–$AgInS_2$ solid‐solution photocatalyst. Angewandte Chemie International Edition, 2005, 117: 3631-3634.
48. Baran T, Wojtyła S, Dibenedetto A, et al. Zinc sulfide functionalized with ruthenium nanoparticles for photocatalytic reduction of CO_2. Applied Catalysis B: Environmental, 2015, 178: 170-176.
49. Maeda K, Sakamoto N, Ikeda T, et al. Preparation of Core–Shell‐Structured Nanoparticles (with a Noble‐Metal or Metal Oxide Core and a Chromia Shell) and Their Application in Water Splitting by Means of Visible Light. Chemistry–A European Journal, 2010, 16: 7750-7759.
50. Liu J Y, Garg B, Ling Y C. $Cu_xAg_yIn_zZn_kS_m$ solid solutions customized with

RuO_2 or $Rh_{1.32}Cr_{0.66}O_3$ co-catalyst display visible light-driven catalytic activity for CO_2 reduction to CH_3OH. Green Chemistry, 2011, 13: 2029-2031.

51. Kumar D P, Shankar M V, Kumari M M, et al. Nano-size effects on CuO/TiO_2 catalysts for highly efficient H_2 production under solar light irradiation. Chemical Communications, 2013, 49: 9443-9445.
52. Garcia‐Esparza A T, Cha D, Ou Y, et al. Tungsten carbide nanoparticles as efficient cocatalysts for photocatalytic overall water splitting. ChemSusChem, 2013, 6: 168-181.
53. Pajares A, Wang Y, Kronenberg M J, et al. Photocatalytic H_2 production from ethanol aqueous solution using TiO_2 with tungsten carbide nanoparticles as co-catalyst. International Journal of Hydrogen Energy, 2020, 45: 20558-20567.
54. Yue X, Yi S, Wang R, et al. A novel architecture of dandelion-like Mo_2C/TiO_2 heterojunction photocatalysts towards high-performance photocatalytic hydrogen production from water splitting. Journal of Materials Chemistry A, 2017, 5: 10591-10598.
55. Ma B, Xu H, Lin K, et al. Mo_2C as Non‐Noble Metal Co‐Catalyst in Mo_2C/CdS Composite for Enhanced Photocatalytic H_2 Evolution under Visible Light Irradiation. ChemSusChem, 2016, 9: 820-824.
56. Yi S S, Yan J M, Wulan B R, et al. Efficient visible-light-driven hydrogen generation from water splitting catalyzed by highly stable CdS@ Mo_2C–C core–shell nanorods. Journal of Materials Chemistry A, 2017, 5: 15862-15868.
57. Yue X, Yi S, Wang R, et al. Well-controlled $SrTiO_3$@ Mo_2C core-shell nanofiber photocatalyst: boosted photo-generated charge carriers transportation and enhanced catalytic performance for water reduction.

Nano Energy, 2018, 47: 463-473.

58. Dong J, Shi Y, Huang C, et al. A new and stable Mo-Mo_2C modified g-C_3N_4 photocatalyst for efficient visible light photocatalytic H_2 production. Applied Catalysis B: Environmental, 2019, 243: 27-35.

59. Zou Y, Ma D, Sun D, et al. Carbon nanosheet facilitated charge separation and transfer between molybdenum carbide and graphitic carbon nitride toward efficient photocatalytic H_2 production. Applied Surface Science, 2019, 473: 91-101.

60. Song Y, Xia K, Gong Y, et al. Controllable synthesized heterostructure photocatalyst Mo_2C@C/2D g-C_3N_4: enhanced catalytic performance for hydrogen production. Dalton Transactions, 2018, 47(41): 14706-14712.

61. Zhang J, Wu M, He B, et al. Facile synthesis of rod-like g-C_3N_4 by decorating Mo_2C co-catalyst for enhanced visible-light photocatalytic activity. Applied Surface Science, 2019, 470: 565-572.

62. Pellegrin Y, Odobel F. Sacrificial electron donor reagents for solar fuel production. Comptes Rendus Chimie, 2017, 20: 283-295.

63. Galińska A, Walendziewski J. Photocatalytic water splitting over Pt−TiO_2 in the presence of sacrificial reagents. Energy & Fuels, 2005, 19: 1143-1147.

64. Ocaña I R, Beltram A, Jaén J J D, et al. Photocatalytic H_2 production by ethanol photodehydrogenation: Effect of anatase/brookite nanocomposites composition. Inorganica Chimica Acta, 2015, 431: 197-205.

65. Chen W T, Chan A, Sun-Waterhouse D, et al. Ni/TiO_2: A promising low-cost photocatalytic system for solar H_2 production from ethanol–water mixtures. Journal of Catalysis, 2015, 326: 43-53.

66. Sola A C, Ramírez de la Piscina P, Homs N. Behaviour of Pt/TiO_2 catalysts with different morphological and structural characteristics in the

photocatalytic conversion of ethanol aqueous solutions. Catalysis Today, 2020, 341: 13-20.

67. Sola A C, Homs N, Ramírez de la Piscina P. Photocatalytic H_2 production from ethanol$_{(aq)}$ solutions: The effect of intermediate products. International Journal of Hydrogen Energy, 2016, 41: 19629-19636.
68. https://apps.fas.usda.gov/newgainapi/api/report/downloadreportbyfilename?filename=Biofuels%20Annual_The%20Hague_EU-28_8-9 2019.pdf. EU Biofuels annual 2019, USDA Foreign Agricultural Service, Gain Report number: NL1902. (Accessed on 5 Septemper 2021)
69. Wang X, Li Z, Shi J, et al. One-dimensional titanium dioxide nanomaterials: nanowires, nanorods, and nanobelts. Chemical Reviews, 2014, 114: 9346-9384.
70. Yang H G, Liu G, Qiao S Z, et al. Solvothermal synthesis and photoreactivity of anatase TiO_2 nanosheets with dominant {001} facets. Journal of the American Chemical Society, 2009, 131: 4078-4083.
71. Pan J, Liu G, Lu G Q, et al. On the true photoreactivity order of {001},{010}, and {101} facets of anatase TiO_2 crystals. Angewandte Chemie International Edition, 2011, 50: 2133-2137.
72. Yu J, Low J, Xiao W, et al. Enhanced photocatalytic CO_2-reduction activity of anatase TiO_2 by coexposed {001} and {101} facets. Journal of the American Chemical Society, 2014, 136: 8839-8842.
73. Yang H G, Sun C H, Qiao S Z, et al. Anatase TiO_2 single crystals with a large percentage of reactive facets. Nature, 2008, 453: 638-641.
74. Hengerer R, Kavan L, Krtil P, et al. Orientation dependence of charge‐transfer processes on TiO_2 (Anatase) single crystals. Journal of the Electrochemical Society, 2000, 147: 1467.

75. Jiang Z, Lv X, Jiang D, et al. Natural leaves-assisted synthesis of nitrogen-doped, carbon-rich nanodots-sensitized, Ag-loaded anatase TiO_2 square nanosheets with dominant {001} facets and their enhanced catalytic applications. Journal of Materials Chemistry A, 2013, 1: 14963-14972.

76. Liu M, Piao L, Zhao L, et al. Anatase TiO_2 single crystals with exposed {001} and {110} facets: facile synthesis and enhanced photocatalysis. Chemical Communications, 2010, 46: 1664-1666.

77. Shi H, Zhang S, Zhu X, et al. Uniform gold-nanoparticle-decorated {001}-faceted anatase TiO_2 nanosheets for enhanced solar-light photocatalytic reactions. ACS Applied Materials & Interfaces, 2017, 9: 36907-36916.

78. Xiong F, Yin L L, Li F, et al. Anatase TiO_2 (001)-(1× 4) Surface Is Intrinsically More Photocatalytically Active than the Rutile TiO_2 (110)-(1× 1) Surface. The Journal of Physical Chemistry C, 2019, 123: 24558-24565.

79. He H, Zapol P, Curtiss L A. A theoretical study of CO_2 anions on anatase (101) surface. The Journal of Physical Chemistry C, 2010, 114: 21474-21481.

80. He H, Zapol P, Curtiss L A. Computational screening of dopants for photocatalytic two-electron reduction of CO_2 on anatase (101) surfaces. Energy & Environmental Science, 2012, 5: 6196-6205.

81. Yang C T, Wood B C, Bhethanabotla V R, et al. CO_2 adsorption on anatase TiO_2 (101) surfaces in the presence of subnanometer Ag/Pt clusters: implications for CO_2 photoreduction. The Journal of Physical Chemistry C, 2014, 118: 26236-26248.

82. Dozzi M V, Selli E. Specific facets-dominated anatase TiO_2: fluorine-mediated synthesis and photoactivity. Catalysts, 2013, 3: 455-485.

83. Wang X, Li T, Yu R, et al. Highly efficient TiO_2 single-crystal photocatalyst with spatially separated Ag and F^- bi-cocatalysts: orientation transfer of photogenerated charges and their rapid interfacial reaction. Journal of Materials Chemistry A, 2016, 4: 8682-8689.

84. Liu L, Jiang Y, Zhao H, et al. Engineering coexposed {001} and {101} facets in oxygen-deficient TiO_2 nanocrystals for enhanced CO_2 photoreduction under visible light. ACS Catalysis, 2016, 6: 1097-1108.

85. Ye L, Mao J, Liu J, et al. Synthesis of anatase TiO_2 nanocrystals with {101},{001} or {010} single facets of 90% level exposure and liquid-phase photocatalytic reduction and oxidation activity orders. Journal of Materials Chemistry A, 2013, 1: 10532-10537.

86. D'Arienzo M, Carbajo J, Bahamonde A, et al. Photogenerated defects in shape-controlled TiO_2 anatase nanocrystals: a probe to evaluate the role of crystal facets in photocatalytic processes. Journal of the American Chemical Society, 2011, 133: 17652-17661.

87. Nowotny M K, Sheppard L R, Bak T, et al. Defect chemistry of titanium dioxide. Application of defect engineering in processing of TiO_2-based photocatalysts. The Journal of Physical Chemistry C, 2008, 112: 5275-5300.

88. Sun D, Yang W, Zhou L, et al. The selective deposition of silver nanoparticles onto {101} facets of TiO_2 nanocrystals with co-exposed {001}/{101} facets, and their enhanced photocatalytic reduction of aqueous nitrate under simulated solar illumination. Applied Catalysis B: Environmental, 2016, 182: 85-93.

89. Mino L, Pellegrino F, Rades S, et al. Beyond shape engineering of TiO_2 nanoparticles: post-synthesis treatment dependence of surface hydration, hydroxylation, Lewis acidity and photocatalytic activity of TiO_2 anatase

nanoparticles with dominant {001} or {101} facets. ACS Applied Nano Materials, 2018, 1: 5355-5365.

90. Tong H, Ouyang S, Bi Y, et al. Nano‐photocatalytic materials: possibilities and challenges. Advanced Materials, 2012, 24: 229-251.
91. Ganguly P, Harb M, Cao Z, et al. 2D nanomaterials for photocatalytic hydrogen production. ACS Energy Letters, 2019, 4: 1687-1709.
92. Ye S, Wang R, Wu M Z, et al. A review on g-C_3N_4 for photocatalytic water splitting and CO_2 reduction. Applied Surface Science, 2015, 358: 15-27.
93. Zhu J, Xiao P, Li H, et al. Graphitic carbon nitride: synthesis, properties, and applications in catalysis. ACS Applied Materials & Interfaces, 2014, 6: 16449-16465.
94. Dong G, Zhang Y, Pan Q, et al. A fantastic graphitic carbon nitride (g-C_3N_4) material: electronic structure, photocatalytic and photoelectronic properties. Journal of Photochemistry and Photobiology C: Photochemistry Reviews, 2014, 20: 33-50.
95. Zhu B, Zhang L, Cheng B, et al. First-principle calculation study of tri-s-triazine-based g-C_3N_4: a review. Applied Catalysis B: Environmental, 2018, 224: 983-999.
96. Liu J, Liu Y, Liu N, et al. Metal-free efficient photocatalyst for stable visible water splitting via a two-electron pathway. Science, 2015, 347: 970-974.
97. Martin D J, Reardon P J T, Moniz S J A, et al. Visible light-driven pure water splitting by a nature-inspired organic semiconductor-based system. Journal of the American Chemical Society, 2014, 136: 12568-12571.
98. Wang K, Li Q, Liu B, et al. Sulfur-doped g-C_3N_4 with enhanced photocatalytic CO_2-reduction performance. Applied Catalysis B: Environmental, 2015, 176: 44-52.
99. Yang P, Wang L, Zhuzhang H, et al. Photocarving nitrogen vacancies in a

polymeric carbon nitride for metal-free oxygen synthesis. Applied Catalysis B: Environmental, 2019, 256: 117794.

100. Lin L , Ren W , Wang C , et al. Crystalline carbon nitride semiconductors prepared at different temperatures for photocatalytic hydrogen production. Applied Catalysis B: Environmental, 2018, 231: 234 – 241.
101. Matsuoka M, Anpo M, Local Structures, Excited States, and Photocatalytic reactivities of highly dispersed catalysts constructed within zeolites, Journal of Photochemistry and Photobiology C: Photochemistry Reviews, 2003, 3: 225-252.
102. Rhodes C J. Zeolites: physical aspects and environmental applications. Annual Reports Section" C"(Physical Chemistry), 2007, 103: 287-325.
103. Gargiulo N, Pepe F, Caputo D. CO_2 adsorption by functionalized nanoporous materials: a review. Journal of Nanoscience and Nanotechnology, 2014, 14: 1811-1822.
104. Corma A, Garcia H. Zeolite-based photocatalysts. Chemical Communications, 2004: 1443-1459.
105. Ikeue K, Yamashita H, Anpo M, et al. Photocatalytic reduction of CO_2 with H_2O on Ti-β zeolite photocatalysts: Effect of the hydrophobic and hydrophilic properties. The Journal of Physical Chemistry B, 2001, 105: 8350-8355.
106. Hwang J S, Chang J S, Park S E, et al. Photoreduction of carbondioxide on surface functionalized nanoporous catalysts. Topics in Catalysis, 2005, 35: 311-319.
107. Anpo M. Photocatalytic reduction of CO_2 with H_2O on highly dispersed Ti-oxide catalysts as a model of artificial photosynthesis. Journal of CO_2 Utilization, 2013, 1: 8-17.
108. Fu Y, Sun D, Chen Y, et al. An amine‐functionalized titanium metal–

organic framework photocatalyst with visible-light-induced activity for CO_2 reduction. Angewandte Chemie International Edition, 2012, 51: 3364-3367.

109. Zhu J, Li P Z, Guo W, et al. Titanium-based metal–organic frameworks for photocatalytic applications. Coordination Chemistry Reviews, 2018, 359: 80-101.

110. Asefa T, MacLachlan M J, Coombs N, et al. Periodic mesoporous organosilicas with organic groups inside the channel walls. Nature, 1999, 402: 867-871.

111. Inagaki S, Guan S, Fukushima Y, et al. Novel mesoporous materials with a uniform distribution of organic groups and inorganic oxide in their frameworks. Journal of the American Chemical Society, 1999, 121: 9611-9614.

112. Inagaki S, Guan S, Ohsuna T, et al. An ordered mesoporous organosilica hybrid material with a crystal-like wall structure. Nature, 2002, 416: 304-307.

113. Polarz S, Kuschel A. Preparation of a periodically ordered mesoporous organosilica material using chiral building blocks. Advanced Materials, 2006, 18: 1206-1209.

114. Hunks W J, Ozin G A. Challenges and advances in the chemistry of periodic mesoporous organosilicas (PMOs). Journal of Materials Chemistry, 2005, 15: 3716-3724.

115. Mizoshita N, Ikai M, Tani T, et al. Hole-transporting periodic mesostructured organosilica. Journal of the American Chemical Society, 2009, 131: 14225-14227.

116. Yamanaka K, Okada T, Goto Y, et al. Dynamics in the excited electronic state of periodic mesoporous biphenylylene-silica studied by time-resolved diffuse reflectance and fluorescence spectroscopy. Physical Chemistry Chemical Physics, 2010, 12: 11688-11696.

117. Okada T, Yamanaka K, Hirose Y, et al. Fluorescence studies on phenylene moieties embedded in a framework of periodic mesoporous organosilica. Physical Chemistry Chemical Physics, 2011, 13: 7961-7967.

118. Kapoor M P, Yang Q, Inagaki S. Self-assembly of biphenylene-bridged hybrid mesoporous solid with molecular-scale periodicity in the pore walls. Journal of the American Chemical Society, 2002, 124: 15176-15177.

119. Okamoto K, Goto Y, Inagaki S. Self-organization of crystal-like aromatic–silica hybrid materials. Journal of Materials Chemistry, 2005, 15: 4136-4140.

120. Bhaumik A, Kapoor M P, Inagaki S. Ammoximation of ketones catalyzed by titanium-containing ethane bridged hybrid mesoporous silsesquioxane. Chemical Communications, 2003: 470-471.

121. Zhai S R, Park S S, Park M, et al. Direct Synthesis of Zr-Containing Hybrid Periodic Mesoporous Organosilicas with Tunable Zirconium Content. European Journal of Inorganic Chemistry, 2007, 5: 5480-5488.

122. Morishita M, Shiraishi Y, Hirai T. Ti-containing mesoporous organosilica as a photocatalyst for selective olefin epoxidation. The Journal of Physical Chemistry B, 2006, 110: 17898-17905.

123. https://ourworldindata.org/co2-and-other-greenhouse-gas-emissions. CO_2 and greenhouse gas emissions. Our world in data, 2017 (last revised in August 2020). (Accessed on 5 Septemper 2021)

124. https://iea.blob.core.windows.net/assets/7e802f6a-0b30-4714-abb1-

46f21a7a9530/Global_Energy_Review_2020.pdf. Global energy and CO_2 emissions in 2020. (Accessed on 5 Septemper 2021)

125. Halmann M. Photoelectrochemical reduction of aqueous carbon dioxide on p-type gallium phosphide in liquid junction solar cells. Nature, 1978, 275: 115-116.
126. Roy S C, Varghese O K, Paulose M, et al. Toward solar fuels: photocatalytic conversion of carbon dioxide to hydrocarbons. ACS Nano, 2010, 4: 1259-1278.
127. Hoffmann M R, Martin S T, Choi W, et al. Environmental applications of semiconductor photocatalysis. Chemical Reviews, 1995, 95: 69-96.
128. Christoforidis K C, Fornasiero P. Photocatalysis for hydrogen production and CO_2 reduction: the case of copper-catalysts. ChemCatChem, 2019, 11: 368-382.
129. Chang X, Wang T, Gong J. CO_2 photo-reduction: insights into CO_2 activation and reaction on surfaces of photocatalysts. Energy & Environmental Science, 2016, 9: 2177-2196.
130. Kubacka A, Fernandez-Garcia M, Colon G. Advanced nanoarchitectures for solar photocatalytic applications. Chemical Reviews, 2012, 112: 1555-1614.
131. Zhou H, Guo J, Li P, et al. Leaf-architectured 3D hierarchical artificial photosynthetic system of perovskite titanates towards CO_2 photoreduction into hydrocarbon fuels. Scientific Reports, 2013, 3: 1667.
132. Zhang X, Han F, Shi B, et al. Photocatalytic conversion of diluted CO_2 into light hydrocarbons using periodically modulated multiwalled nanotube arrays. Angewandte Chemie International Edition, 2012, 51: 12732-12735.
133. Izumi Y. Recent advances in the photocatalytic conversion of carbon dioxide to fuels with water and/or hydrogen using solar energy and beyond. Coordination Chemistry Reviews, 2013, 257: 171-186.

134. Das R, Chakraborty S, Peter S C. Systematic Assessment of Solvent Selection in Photocatalytic CO_2 Reduction. ACS Energy Letters, 2021, 6: 3270-3274.

Chapter 2.

Experimental section

This chapter gives a brief description of the techniques used for the characterization of materials prepared in this work. Moreover, the photocatalytic reaction system and the analytical methods used to study the photocatalytic behaviour of different materials are described.

2.1 Characterization techniques

2.1.1 Inductively coupled plasma optical emission spectrometry (ICP-OES)

Ti content in Ti-PMOs, and Mo content in $Mo_xCT/g\text{-}C_3N_4$ and Mo_xC/TiO_2-X were determined by ICP-OES [1].

The dissolution of samples was carried out as follows:

1) For Ti-PMOs materials, about 50 mg of samples were digested with 4 mL of HF and 4 mL of HNO_3, the mixture was treated with microwave at 210 °C for 20 min (heating ramp of 10 °C·min^{-1}).

2) For $Mo_xCT/g\text{-}C_3N_4$ materials, about 50 mg of samples were digested with 5 mL HNO_3 and 3 mL H_2SO_4 and then treated with microwave at 210 °C for 20 min (heating ramp of 10 °C·min^{-1}).

3) For Mo_xC/TiO_2-X samples, about 50 mg of samples were digested with 2.5 mL HNO_3 and 0.5 mL HF and then treated at 90 °C overnight (almost 12 hours).

The resulting solutions were diluted to 50 mL with HPLC grade water and used for the final analysis. Different standardized solutions were used for a proper quantification. All acids used in the digestion process were concentrated.

In this work, the ICP-OES spectrometer employed was a Perkin Elmer Optima 3200RL. The analysis was carried out in the Scientific and Technological Centers of the University of Barcelona (CCiTUB).

2.1.2 Powder X-ray diffraction (XRD)

Powder X-ray diffraction (XRD) is one of the most frequently applied techniques for the characterization of solids. In this work, it is used to identify crystalline phases of materials from lattice structural parameters, to obtain an indication of crystallite size, and to analyze the ordered mesoporosity of Ti-PMOs materials.

The size (*D*) of the diffracting crystallite can be determined using the Debye-Scherrer equation [2]:

$$D = \frac{K\lambda}{b\cos\theta}$$

Where λ is the X-ray wavelength and *K* is a dimensionless shape factor, with a value close to 1. In this work, a constant value *K*=1 is used for a specific diffraction peak; *b* is the full width at the half of the maximum intensity (FWHM).

Ti-PMOs samples were analyzed in the small-angle zone (0.2°<2θ<5°) in order to detect their mesoscopical order [3].

The XRD measurements were carried out in the CCiTUB. The standard measurements (5-90°) were performed with a PANalytical X'Pert PRO MPD Alpha1 powder diffractometer equipped with a Cu $K_{\alpha 1}$ radiation (α = 1.5406 Å) in Bragg-Brentano θ/2θ geometry of 240 millimeters of radius. The small-angle measurements (0.2°<2θ<5°) were obtained using a PANalytical X'Pert PRO

MPD *θ/θ* powder diffractometer of 240 millimeters of radius, in a configuration of the convergent beam with a focalizing mirror and a transmission geometry with flat samples sandwiched between low absorbing films.

The indexation of diffraction peaks and phase identification was performed using the International Centre for Diffraction Data, PDF and JCPDS files [4].

2.1.3 Fourier-transform infrared spectroscopy (FTIR)

Infrared spectroscopy was used in this work for the characterization of Mo_xCT/g-C_3N_4 and Ti-PMOs materials in transmission and attenuated total reflectance (ATR) modes, respectively. The measurements were carried out in the Inorganic and Organic Chemistry Department of UB.

FTIR in transmission mode was performed with a Thermo Nicolet 5700 FTIR instrument; KBr was used as diluent for the pellet preparation. ATR-FTIR measurements were performed using a Thermo Scientific Nicolet iS5 FTIR Spectrometer with an iD7 ATR accessory; the ATR accessory allows the direct examination of the sample without any preparation.

2.1.4 N_2 adsorption-desorption isotherms

The determination of the specific surface area of the catalysts was carried out from the physical adsorption of N_2 on the surface of the solid at -196 °C, which corresponds with that of N_2 condensation.

The Brunauer, Emmet and Teller (BET) method [5] was used according to:

$$\frac{P}{V(P^0 - P)} = \frac{1}{V_m C} + \frac{(C-1)}{V_m C} \times \frac{P}{P^0}$$

Where V is the volume of gas adsorbed under standard conditions of pressure and temperature; V_m is the volume of gas adsorbed when the monolayer is formed; P/P^0 is the relative pressure of the gas and C is a constant that depends on the heat of adsorption of the gas on the solid.

The specific surface area (S_{BET}) is expressed in $m^2 \cdot g^{-1}$ of the solid and is calculated as:

$$S_{BET} = \frac{N_m \cdot N_A \cdot \sigma_m}{m}$$

$$N_m = \frac{V_m \cdot \rho}{M_m}$$

Where N_m is the number of moles of gas adsorbed per gram of solid when a monolayer is formed; N_A is the Avogadro constant; σ_m is the area occupied by an adsorbed gas molecule (σ_m (N_2) = 0.162 nm^2 at -196 °C); ρ is the density of adsorbed N_2; M_m is the molecular mass of the gas and m is the mass of the solid.

The pore characteristics of the materials (pore volume and pore size) have been determined by the method of Barret, Joyner and Halenda (BJH) [6] using the desorption data of the adsorption-desorption isotherm of N_2.

Before the measurement, the materials were degassed under N_2 flow (20 $mL \cdot min^{-1}$) using the following conditions: Ti-PMOs at 150 °C for 10 hours, $Mo_xCT/g\text{-}C_3N_4$ at 250 °C for 5 hours and Mo_xC/TiO_2-X at 100 °C for 24 hours.

Adsorption-desorption isotherms were performed using a Tristar II 3020 Micromeritics instrument, available in our group at the Catalonia Energy Research Institute (IREC).

2.1.5 Raman spectroscopy

Raman spectroscopy is a characterization technique, which is based on the study of the radiation scattered by a sample after the incidence of a monochromatic light beam of frequency (ν_0). When a light beam interacts with matter, much of the scattered radiation has a frequency equal to that of the incident light beam (ν_0), known as Rayleigh scattering. However, a small fraction of the radiation exhibits a change in frequency (Raman scattering) that provides information of the bonds present in the sample. Raman spectroscopy is thus a technique of broad application in the characterization of solids, and, is complementary to infrared spectroscopy and X-ray diffraction in the structural characterization of materials.

In this work, Raman spectroscopy was used for the characterization of Ti-PMOs samples. Raman spectroscopy measurements were performed with a Jobin-Yvon LabRaman HR 800 spectrometer in CCiTUB. The spectra were resulted by 3 accumulations of 5s each with a magnification of 50x. Samples were excited with a 532 nm solid-state laser with power limited to 1.5 mW to avoid heating effects.

2.1.6 Ultraviolet-visible diffuse reflectance spectroscopy (UV-vis DRS)

When a beam of UV-visible radiation impinges on a material, different phenomena occur, such as reflection, scattering or transmission through the sample. Diffuse reflectance corresponds to the radiation that is absorbed by the material and emerges by multiple scattering. The diffuse reflectance spectrum of a powder semiconductor is characterized by increased diffuse reflectance at a given wavelength, attributed to the decrease in the absorption coefficient. The Kubelka–Munk (K-M) model allows the transformation of reflectance spectrum into the corresponding absorption spectrum:

$$F(R_\infty) = \frac{(1-R_\infty)^2}{2R_\infty} = \frac{K}{S}$$

$$R_\infty = \frac{R_{sample}}{R_{reference}}$$

Where R_∞ is the reflectance of an extremely thin sample; K and S are the absorption and scattering coefficients.

E_g values were determined using the Tauc plot, $(F(R_\infty)\ h\nu)^{\frac{1}{2}}$ versus hν [7].

The analysis of Ti-PMOs samples was carried out using a Perkin-Elmer Lambda 19 Series spectrometer in the Department of Chemical Engineering and Analytical Chemistry of UB with the help of Prof. Anna de Juan Capdevila. The samples were prepared in the middle of two quartz glass coating the window of the detector. Mo_xCT/g-C_3N_4 samples were analyzed in IREC with a Perkin Elmer Lambda 950 UV-vis spectrophotometer equipped with an integrating sphere and a Praying Mantis accessory. The analysis of Mo_xC/TiO_2-X samples was carried out with a Shimadzu UV3600 UV–vis/NIR apparatus equipped with a diffuse reflectance cell in the Polytechnic University of Catalonia (UPC). In all cases, $BaSO_4$ was used as reference.

2.1.7 X-ray photoelectron spectroscopy (XPS)

X-ray photoelectron spectroscopy (XPS) is among the most frequently used techniques in catalysis. XPS is restricted to the analysis of the first layers of solid materials, making it widely used to determine the chemical state and the atomic concentration of different elements present on the surface [8].

In general, the emission of electrons is caused by a monochromatic beam of X-rays, which hits the sample. The kinetic energy of the emitted electrons is

determined by means of an energy analyzer. The fundamental equation that relates the BE of the emitted photoelectron with the measured electron kinetic energy (KE) is given by:

$$BE = h\nu - KE - \phi$$

Where $h\nu$ is the incident photon (X-ray) energy and ϕ is the work function of the spectrometer.

The atomic concentration of the elements on the surface can be obtained by applying the following equation:

$$C_x = \frac{I_x/S_x}{\sum I_i/S_i}$$

Where C_x is the atomic concentration of the element (x), I is the area of the peak of a particular element and S is the corresponding atomic sensitivity factor.

XPS analysis were performed at the CCiTUB using a Perkin Elmer PHI-5500 spectrometer equipped with a monochromatic X-ray source (Al Kα line, $h\nu$ = 1486.6 eV and 350 W) positioned perpendicular to the analyzer. The pressure of the chamber during the acquisition of the spectra was kept below $1.33 \cdot 10^{-6}$ Pa. The binding energy values of the different elements were referred to C 1s at 284.8 eV. The C 1s peak position of Mo_xCT/g-C_3N_4 and Mo_xC/TiO_2-X was determined using Au $4f_{7/2}$ peak at 84.0 eV as reference. The MultiPak software processed the deconvolution of the spectra.

2.1.8 Transmission electron microscopy (TEM)

TEM is a technique that allows obtaining images and structural information at the nanometric scale of a solid. The system uses an accelerated beam of electrons, which passes through a very thin specimen to enable the observation of features such as structure and morphology. When working at high resolution (HR-TEM), it allows directly distinguishing the crystallographic planes of the sample and precisely determining the structure of the crystalline phases present by applying the Fourier transform [9].

Scanning TEM imaging (STEM) can be also used to analyze the surface element distribution when coupled to appropriate detectors.

The transmission electron microscope studies carried out in this work were performed in a JEOL JEM-2100 high-resolution microscope in CCiTUB using a potential electron acceleration of 300 kV. The samples were prepared by dispersing a small amount of solid in pure ethanol in an ultrasound bath. A dispersion of samples was deposited on a copper micro-grid for observation. The results were processed by software's of INCA and Digital Micrograph.

2.1.9 Photoluminescence (PL) spectroscopy

PL spectroscopy is a useful technique for the characterization of semiconductors. When a semiconductor is irradiated with light of energy higher than Eg, electron/hole pairs are generated, and then in the recombination process photons are emitted. The PL spectrum can provide information of the presence of impurities and defects in the sample. The intensity of PL spectrum can be used to compare the electron-hole recombination rate. A higher intensity of the PL band is related with a higher recombination rate [10,11].

PL measurements of Ti-PMOs and Mo_xCT/g-C_3N_4 samples were carried out in the Faculty of Physics of UB with the help of Dr. Frank Güell, using a

Kimmon IK Series He-Cd CW laser (325 nm and 40 mW) at room temperature. Fluorescence was dispersed through an Oriel Corner Stone 1/8 74000 or a Spectra2750 Pro monochromator, detected with a Hamamatsu R928 photomultiplier, and amplified through a Stanford Research Systems SR830 DSP lock-in amplifier. A 360 nm filter was used for filtering the stray light and the emission spectra were corrected using the optical transfer function of the PL setup. For Mo_xC/TiO_2-X samples, the measurements were obtained in CCiTUB at room temperature using a Jobin-Yvon LabRam HR 800 dispersive spectrometer, coupled to an optical microscope Olympus BXFM (40x NUV microscope objective). The CCD detector was cooled at -70 °C. The laser line used was 325 nm and the dispersive grating was 300 lines/mm.

2.1.10 Photoelectrochemical (PEC) characterization

The properties related with charge carriers' transport capability of a semiconductor under illumination conditions can be evaluated by photoelectrochemical (PEC) measurements. For PEC measurements, the semiconductor is used as the working electrode in an electrical circuit. The density of charge carriers and therefore the photocurrent generated by irradiating the semiconductor with light can be measured. Moreover, the measurements of the electron transfer in the semiconductor electrode and across the electrode/electrolyte interface are commonly determined by electrochemical impedance spectroscopy (EIS).

The transient photocurrent and electrochemical impedance spectroscopy measurements were carried out using a computer-controlled potentiostat (VMP3, BioLogic Science Instruments) with an undivided three-electrode cell. The counter electrode, reference electrode and working electrodes were a Pt wire, an Ag/AgCl (3 M KCl) electrode, and the prepared photocatalyst electrode (1 cm^2 geometric area), respectively. The working electrode was prepared on

fluorine-doped tin oxide (FTO) conductor glass as follows: 10 mg of samples were suspended in the deionized water (1 mL) with Nafion (0.1 mL) and ultrasonicated for dispersing. 0.1 mL of the mixture was then deposited onto the FTO glass and heated at 120 °C for 1 h to evaporate the solvent. A 0.5 M Na_2SO_4 aqueous solution was used as the electrolyte. Measurements under illumination were performed using a 150 W AM 1.5 G solar simulator (Solar Light Co., 16S-300-002 v4.0) with an incident light intensity set at 1 Sun (100 mW cm^{-2}). The equipment used is shown in Figure 2.1.

The PEC tests were performed in IREC with the help of Dr. Teresa Andreu and Dr. Sebastián Murcia-López.

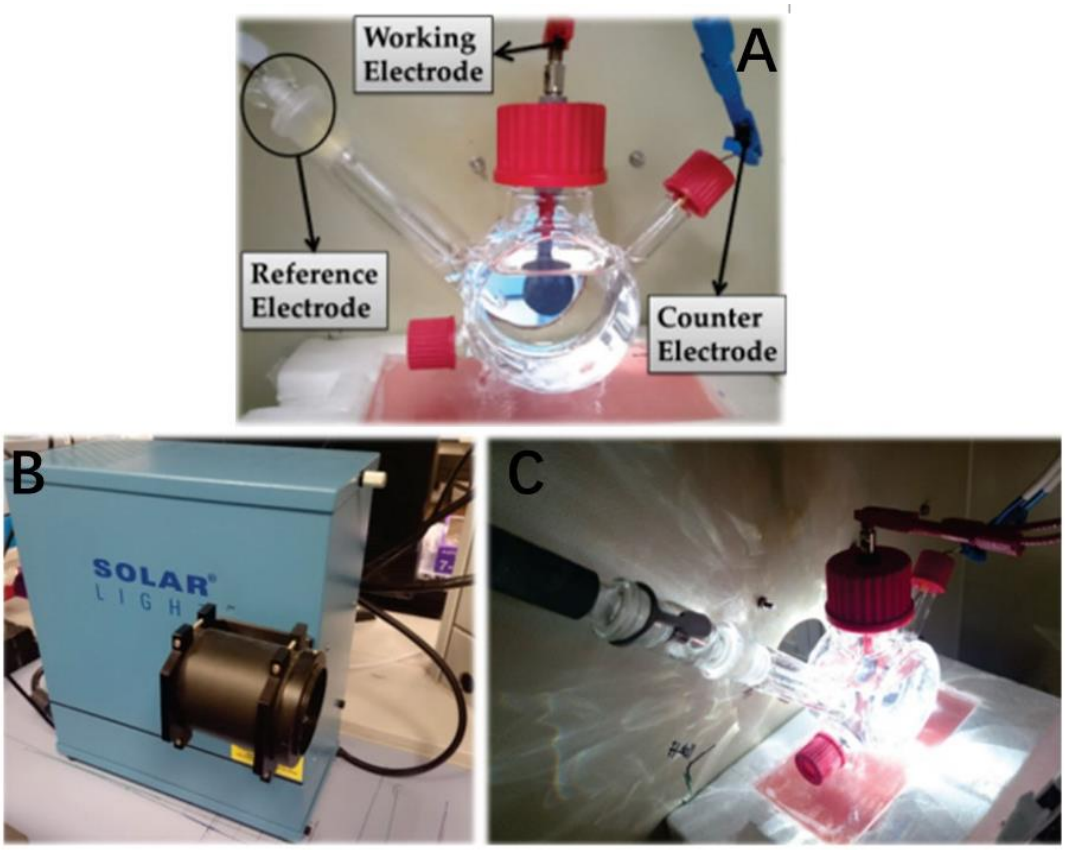

Figure 2.1. Equipment used for the PEC measurements. (**A**) three-electrode reactor; (**B**) solar simulator lamp; (**C**) a running experiment under illumination.

2.2 Photocatalytic reaction system

The study of the photocatalytic behaviour of the prepared materials was carried out in a designed system, which operates in the liquid phase with an online analysis of evolved gases (Figure 2.2).

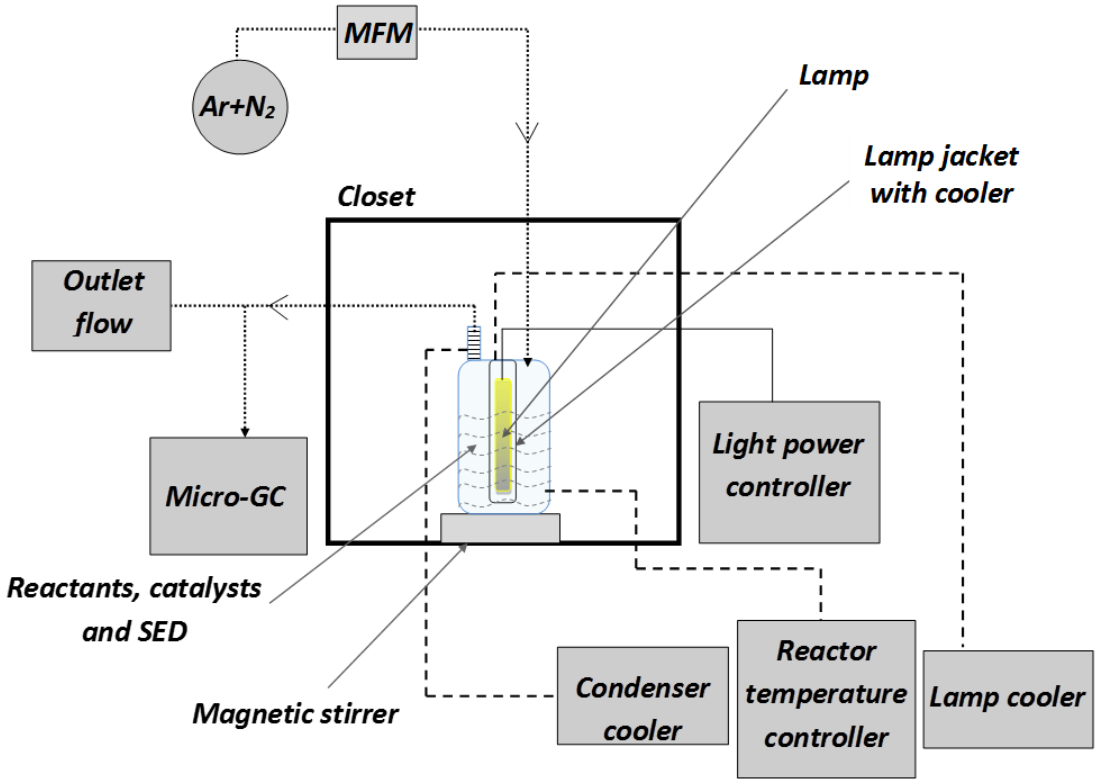

Figure 2.2. Photocatalytic reaction system.

The reaction system consists of a custom-made jacketed glass reactor (Figure 2.3A) with a volume of 300 mL (Trallero and Schlee S. L.), which is located inside a well-closed black wooden cabinet. The reaction temperature (20 °C) is maintained by a Huber MCP K6 thermostat bath, which continually recirculates water. The reactor has five openings for connection (Figure 2.3B). A thermocouple connected to the opening **1,** reads the temperature in the

solution during the photocatalytic test and allows it to be controlled by the thermostatic bath that recirculates water through the external jacket. In the opening **2**, there is a steel tube connection that leads to a pressure gauge located outside the cabinet, which reports a possible unwanted overpressure in the reactor; opening **3** allows the entry of gases. During the photocatalytic H_2 production, Ar was used as carrier and N_2 (40 % v/v) as internal standard. In CO_2 photoreduction reaction, pure CO_2 flow was used. The gas-phase products leave the reactor through opening **4**, where a condensation column is connected and kept at -15 °C by means of an ethylene glycol refrigerated recirculation system. The gas flow rate of the effluent can be periodically measured and the composition is analyzed using an online Varian CP-4900 micro gas chromatograph equipped with two modules (A and B) and micro-TCD detectors. A sample suction system sends an aliquot of samples to each of the modules. Module A contains a molecular sieve column (Molsieve 5Å, 10 m) and uses Ar as carrier gas, it is used for the analysis of H_2, O_2, N_2 and CO. Module B with a PPQ type column (10 m) uses He as a carrier gas and allows the analysis of CO_2 and hydrocarbons, such as CH_4 and olefins. The detection limits of both modules are about 10 ppm. The lamp jacket with double-wall is introduced into the reactor using the central opening **5** (Figure 2.3B).

In this work, two different lamp jackets (2 mm wall thickness) were used for different photoreaction conditions. One is made of highly purified quartz (No. 7854-25 ACE Glass) with a full spectrum transmittance; the second one is made of borosilicate glass (No. 7857-05 ACE Glass) which can act as a light filter, cutting the irradiation with wavenumber lower than 385 nm. The cooling of the lamp jacket is controlled by a Unichiller Huber 006-MPC cooler and a circulation system that allows the temperature outside the lamp jacket to be kept at 20 °C by recirculating water inside.

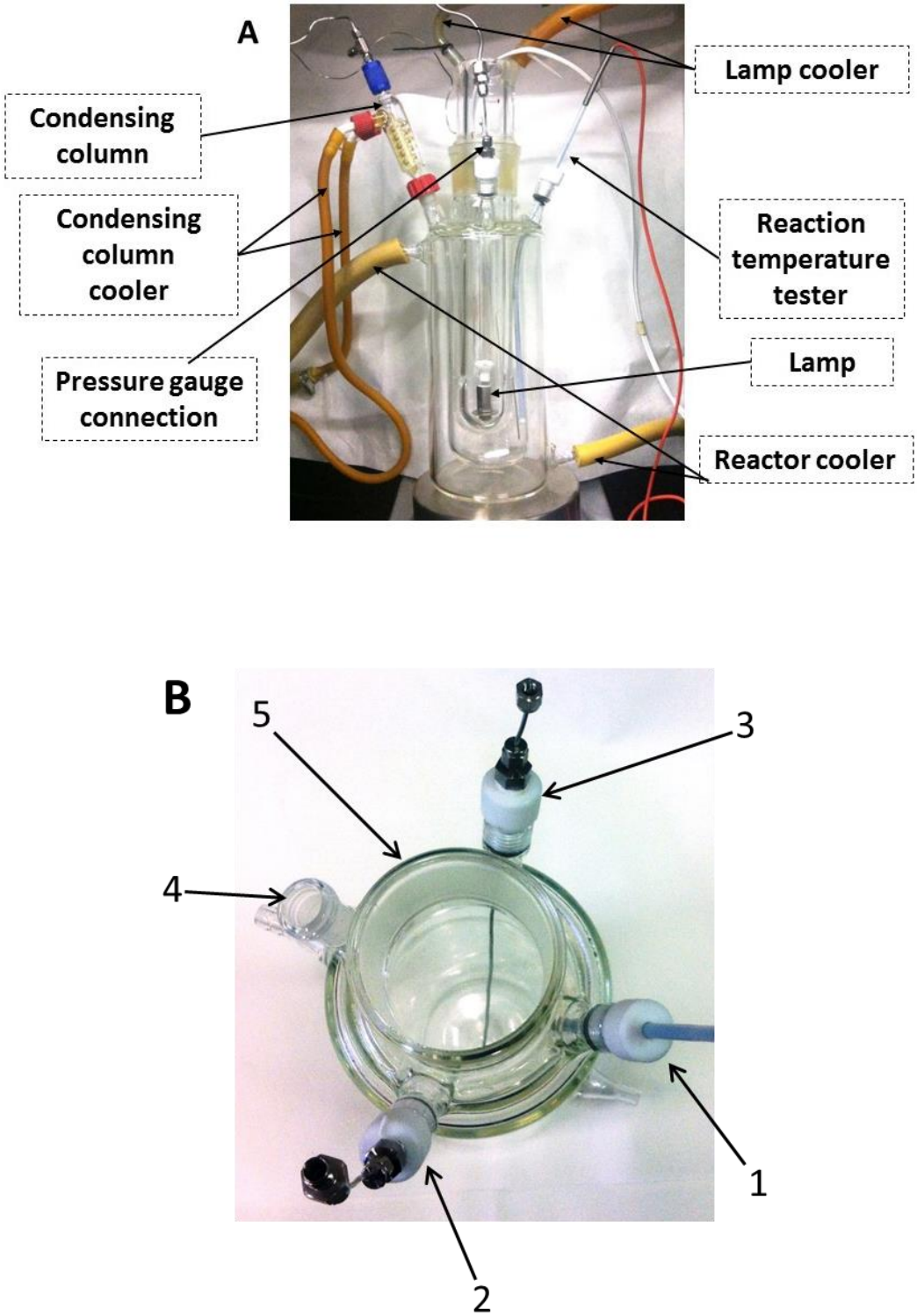

Figure 2.3. Photoreactor: (**A**) front view; (**B**) top view. **1**, thermocouple; **2**, connection with the pressure meter; **3**, gas inlet; **4**, gas outlet; **5**, central opening for jacketed lamp introduction (Photographs taken by Dr. Arberto).

The light radiation source is a broad-spectrum Hg Ace-Hanovia lamp powered by an ACE-GLASS 7830 Power Supply. Its emission spectrum is shown in Figure 2.4. The actual power radiation can be measured with a light density detector (LP471 Irradiance Probe, DELTA OHM).

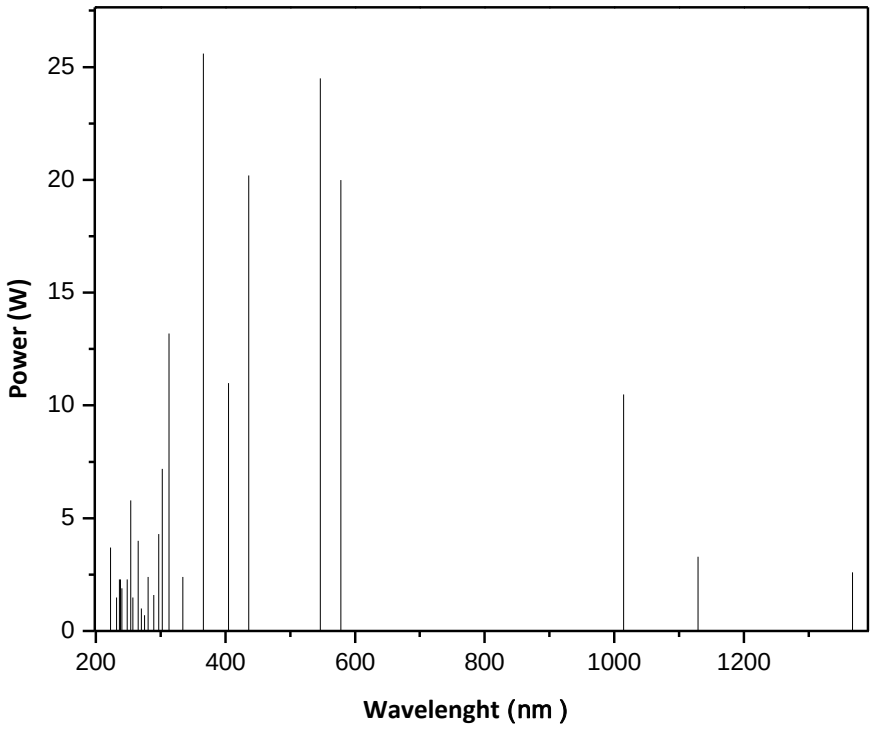

Figure 2.4. The emission spectrum of the 175.9 W Ace-Hanovia lamp from Ace glass inc.

For the photocatalytic experiments, 250 ml of the substrate solution and the appropriate amount of catalysts are used. The mixture is kept under constant stirring at 1080 rpm employing an OVAN MC08C external magnetic stirrer.

In Figure 2.5, a photograph of the experimental setup of the photocatalytic system is shown.

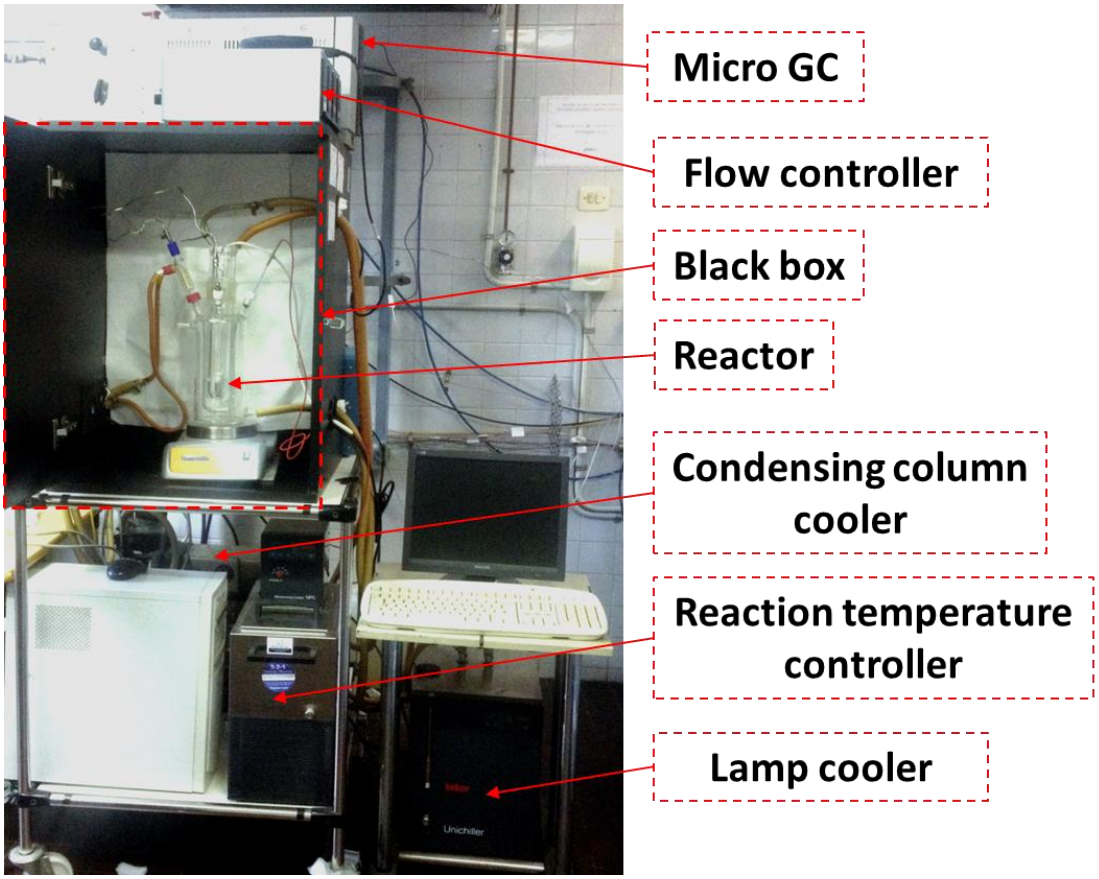

Figure 2.5. Assembly of the photocatalytic system (open) (Photographs taken by Dr. Arberto).

At the end of the reaction, the post-reaction solution is filtered and an aliquot is extracted through a PTFE (0.20 µm) filter and analyzed by gas chromatography (Varian 450) using a CP-Sil 8 CB 30 m x 0.25 mm CP5860 column with an FID detector.

The apparent quantum efficiency (AQE) is a common method to evaluate photoreaction efficiency [12]. It was calculated for the photocatalytic H_2

production taking into account the number of electrons used in the hydrogen generation:

$$\mathrm{AQE\%} = \left(\frac{\text{number of evolved } H_2 \text{ molecules x 2}}{\text{number of incident photons}}\right) \text{x100}$$

The estimated number of incident photons capable to generate a couple of e^-/h^+ for a given photocatalyst was calculated from the measured radiated watt density at the exterior wall of the lamp-jacket and the spectral lamp lines having energy higher than the Eg of the photocatalytic material used.

2.3 References

1. Olesik J W. Elemental analysis using ICP-OES and ICP/MS. Analytical Chemistry, 1991, 63: 12A-21A.
2. Niemantsverdriet J W. Spectroscopy in catalysis: an introduction. John Wiley & Sons, 2007.
3. Inagaki S, Guan S, Ohsuna T, et al. An ordered mesoporous organosilica hybrid material with a crystal-like wall structure. Nature, 2002, 416: 304-307.
4. Gates-Rector S, Blanton T. The powder diffraction file: a quality materials characterization database. Powder Diffraction, 2019, 34: 352-360.
5. Brunauer S, Emmett P H, Teller E. Adsorption of gases in multimolecular layers. Journal of the American Chemical Society, 1938, 60: 309-319.
6. Barrett E P, Joyner L G, Halenda P P. The determination of pore volume and area distributions in porous substances. I. Computations from nitrogen isotherms. Journal of the American Chemical Society, 1951, 73: 373-380.

7. Makuła P, Pacia M, Macyk W. How to correctly determine the band gap energy of modified semiconductor photocatalysts based on UV–Vis spectra. The Journal of Physical Chemistry Letters, 2018, 9: 6814-6817.

8. Hüfner S. Photoelectron spectroscopy: principles and applications. Springer, 2003.

9. Imelik B, Vedrine J C. Catalyst characterization: physical techniques for solid materials. Springer, 1994.

10. Anpo M, Dzwigaj S, Che M. Chapter 1: Applications of Photoluminescence Spectroscopy to the Investigation of Oxide‐Containing Catalysts in the Working State. Advances in catalysis, Elsevier, 2009, 52: 1-42.

11. Matsuoka M, Kamegawa T, Anpo M. Photoluminescence spectroscopy and its application to the characterization of active sites and reaction dynamics in catalysis. Handbook of Heterogeneous Catalysis, Wiley, 2008: 1065-1073.

12. Braslavsky S E, Braun A M, Cassano A E, et al. Glossary of terms used in photocatalysis and radiation catalysis (IUPAC Recommendations 2011). Pure and Applied Chemistry, 2011, 83: 931-1014.

Chapter 3.

Study of Ti-PMOs as photocatalysts for H_2 evolution and CO_2 photoreduction

In this chapter, we present the study of Ti-PMOs as photocatalysts for H_2 evolution and CO_2 photoreduction. A series of complex organic-inorganic mesoporous materials, Ti-PMOs, were successfully synthesized by a microwave-assisted method, which allowed the preparation of periodic mesoporous organosilicas (PMOs) with Ti (IV) forming part of the structure (Ti-PMOs).

Materials were characterized by N_2 physisorption, XRD, TEM-HRTEM, Raman, Infrared, UV-vis DRS, XPS and PL spectroscopy and PEC measurements. Ti-PMOs showed high surface-areas (742-829 m^2g^{-1}), molecular-scale periodicity in the pore walls and mesoscopically ordered structures.

Ti-PMOs were studied in the CO_2 photoreduction in the liquid phase under UV-visible irradiation using TEOA as SED agent. A detailed study of the TEOA degradation under irradiation conditions was carried out. The results evidenced that at least a part of C1 and C2 products obtained came from the TEOA transformation under the irradiation conditions used. However, Ti-PMOs were effective in the photocatalytic H_2 evolution from an ethanol aqueous solution under UV-visible irradiation. Ti-PMOs showed a better photocatalytic behaviour than PMO and P25 (TiO_2), which is related with the presence of well-dispersed tetrahedral Ti(IV) in the PMOs network.

For Ti-PMOs, the photocatalytic H_2 production depended on the Ti content and was related with the photoelectrochemical characteristics of the samples and with the presence of Ti (IV) in the PMO framework. The preparation, characterization and study in the photocatalytic H_2 production of Ti-PMOs from $ethanol_{aq}$ have been recently published [1].

3.1 Preparation of Ti-PMOs

Biphenyl-bridged Ti-PMOs, with Si/Ti molar ratios of about 10, 20 and 40 (Ti10-PMO, Ti20-PMO and Ti40-PMO), were prepared on the basis of the method proposed for the synthesis of biphenyl-bridged silsesquioxane silica with crystal-like pore walls (PMO), using 4,4′bis(triethoxysilyl)biphenyl and octadecyltrimethylammonium chloride (C18TMACl) as the surfactant in basic media [1,2]. In the present work, Ti was introduced by addition to the initial synthesis mixture of the appropriate amount of tetrabutyl titanate in 2-propanol solution, and the suspension was heated with microwaves.

In a typical procedure, the synthesis of the desired Ti-PMO was carried out adding 4,4′bis(triethoxysilyl) biphenyl (5 mmol) with stirring to a solution containing a mixture of C18TMACl surfactant (6.4 mmol), 6N NaOH (60.8 mmol) and distilled water (6.6 mol). Then, the desired amount of a solution of tetrabutyl titanate in 2-propanol was added, and kept under vigorous stirring at ambient temperature for 20 hours. After, the resulting mixture was transferred to a microwave reactor (Roto SYNTH Milestone) and treated under 100 °C (300W) for 1 h; the resulting solid was filtered and washed with deionized water. The surfactant was removed by treating the as-made material with an ethanol/HCl (2M) solution at ambient temperature for 8h, the suspension was filtered and the product was finally dried at 100 °C.

For comparative purposes, a non-containing Ti sample (PMO) was also prepared [1,2]. A scheme of the synthetic procedure is shown in Figure 3.1.

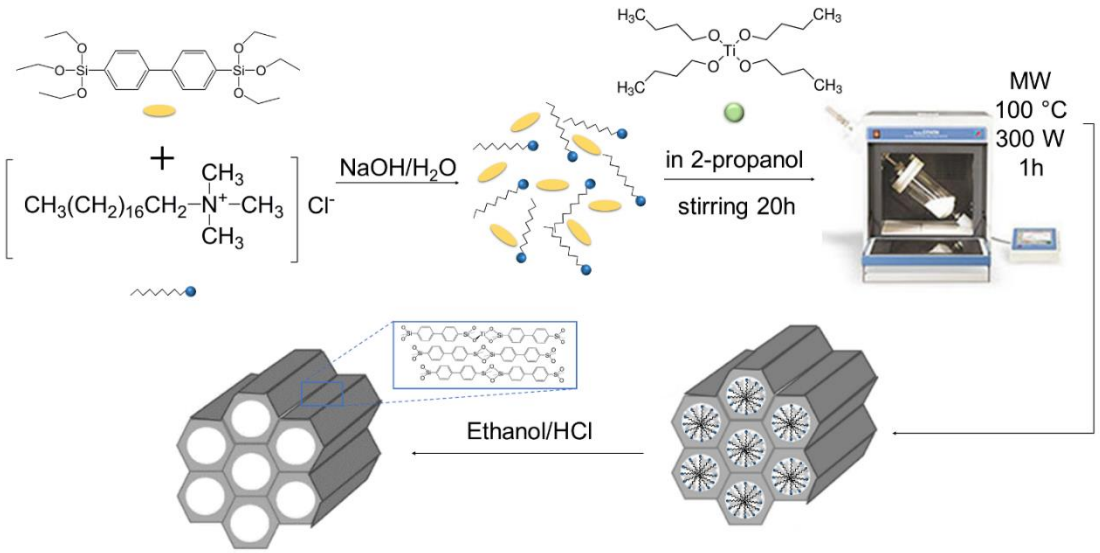

Figure 3.1. The synthetic procedure of Ti-PMOs.

3.2 Characterization of Ti-PMO photocatalysts

Figure 3.2 shows the N_2 adsorption-desorption isotherms of PMO and Ti-PMOs materials. The information about the textural characteristics of samples can be obtained by inspection of the characteristics of the N_2 adsorption-desorption isotherms.

All Ti-PMOs materials present high surface areas (742-829 m^2 g^{-1}) (Table 3.1), which are slightly lower than that of PMO (871 m^2 g^{-1}). All samples show typical type-IV curves (Figure 3.2) characteristic mesoporous materials. Except for Ti10-PMO, no evident hysteresis was observed, pointing to type-IVb isotherms, for which mesoporous below about 4 nm width are expected [3]. Ti10-PMO exhibited H1 hysteresis loop, indicating that wider (>4 nm) uniform mesoporous exist. Pore-size distribution curves are shown in Figure 3.3.

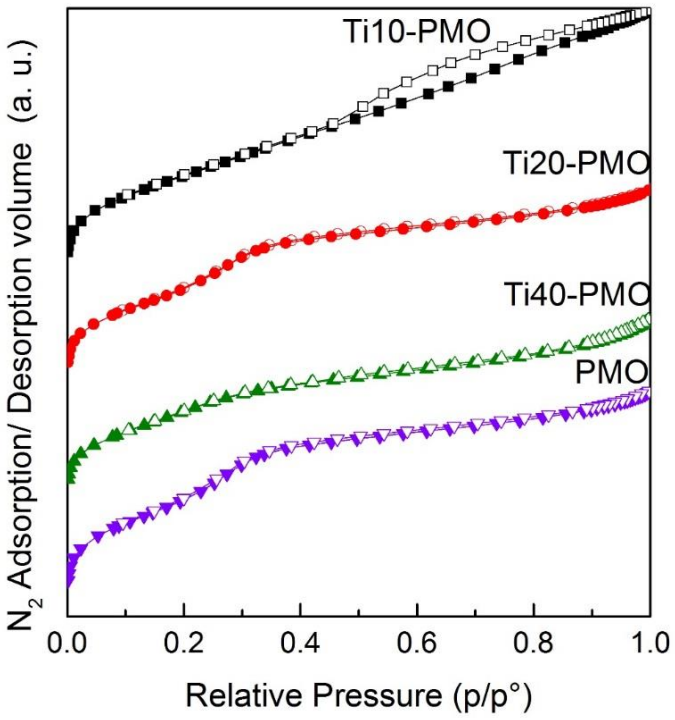

Figure 3.2. N_2 adsorption-desorption isotherms at -196 °C of PMO and Ti-PMOs materials.

The introduction of a small amount of Ti in the mesoporous structure of PMO produces for Ti40-PMO, a slight increase in the pore diameter and a slight lowering of the surface area and total pore volume, in comparison with the original PMO material (Table 3.1). A further increase of the Ti content produces an increase of surface area and total pore volume, always maintaining an increase of the pore diameter from Ti40-PMO through Ti10-PMO samples. This points out that for Ti-PMOs, blocking of the porous channels did not occur.

Table 3.1. Titanium content and textural properties of Ti-PMOs and PMO.

Sample	Ti (% wt)	Si/Ti (mol/mol)	S_{BET} ($m^2\ g^{-1}$)	Pore volume ($cm^3\ g^{-1}$)	Pore diameter (nm)
Ti10-PMO	1.65	10.83	829	0.84	4.2
Ti20-PMO	0.82	22.84	806	0.63	3.6
Ti40-PMO	0.52	35.48	742	0.52	3.1
PMO	---	---	871	0.69	2.9

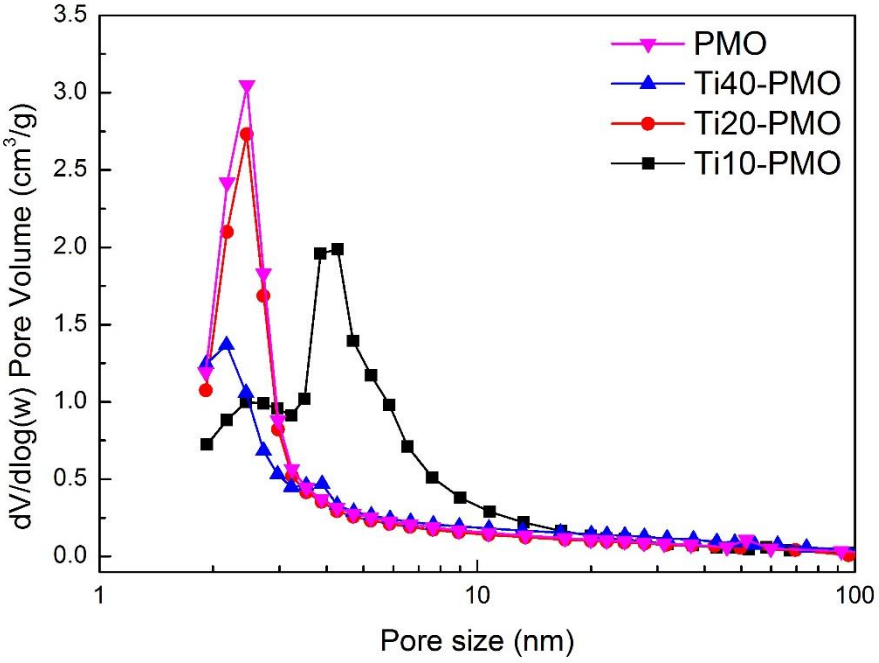

Figure 3.3. Pore-size distribution curves of Ti-PMOs and PMO catalysts.

XRD patterns of Ti-PMOs and PMO in the small-angle zone ($0.2<2\theta<5°$) and in the medium diffraction angles ($2\theta=4\text{-}50°$) are displayed in Figures 3.4 and 3.5, respectively. Diffraction patterns correspond well with that expected for biphenyl-bridged silsesquioxane with a mesoscopically ordered structure and molecular-scale periodicity in the pore-walls [2]. XRD patterns of Ti-PMOs

samples evidenced that the structural characteristics of PMO were mostly kept in Ti-PMOs with the incorporation of Ti in the PMO framework. The characteristic diffraction peak of as-prepared samples at about 2θ of 2°, indicates the existence of mesoscopically ordered structures [2]; the corresponding *d* spacing increased with the Ti content (*d*=41.8 Å, 44.6 Å and 49.9 Å for Ti40-PMO, Ti20-PMO and Ti10-PMO, respectively), this could be related with the introduction of Ti in the framework of PMO. However, the intensity and the shape of the peak of Ti10-PMO (Figure 3.4), with the highest Ti content, show a partial loss of the ordered structure. Besides the peak at about 2θ of 2°, other five diffraction peaks can be observed in XRD patterns of PMO and Ti-PMOs (2θ=4-50°) (Figure 3.5). The corresponding *d* spacing values of Ti-PMOs are similar to that of PMO, which are 11.5 Å, 5.9 Å, 3.9 Å, 2.9 Å and 2.5 Å [1,2]. XRD patterns of Ti-PMOs suggest that both the mesoscopically ordered structure and the crystal-like molecular-scale periodicity of the pore walls, already reported for biphenyl-bridged silsesquioxane [2], are kept in a major extension, at least in the new Ti40-PMO and Ti20-PMO samples.

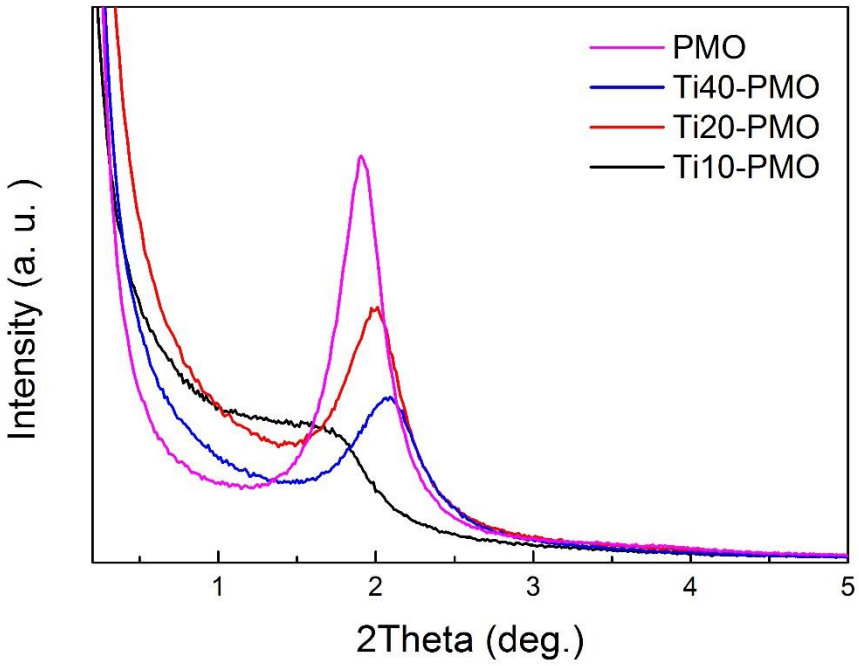

Figure 3.4. XRD patterns of Ti-PMOs and PMO in the low-angle region (0.2<2θ<5°).

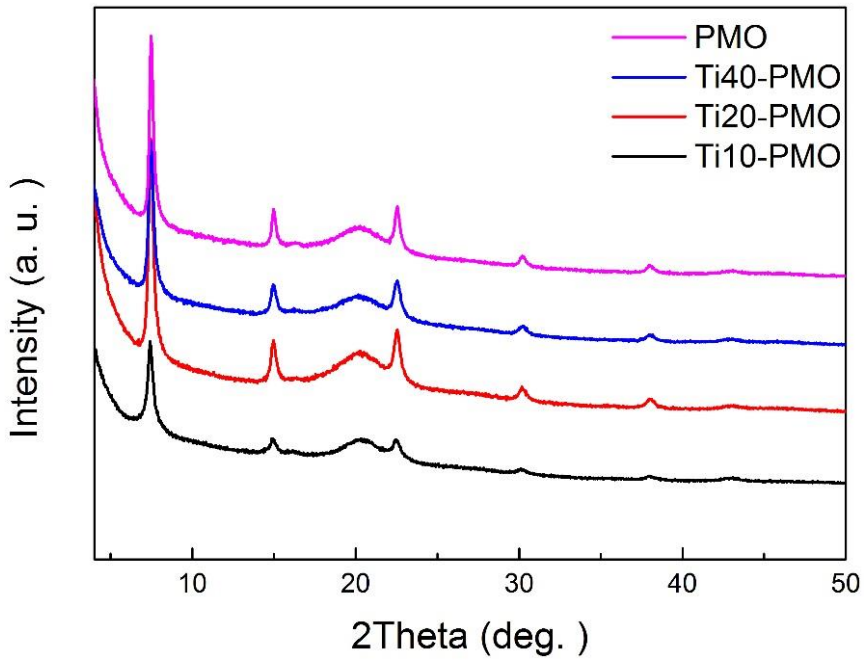

Figure 3.5. XRD patterns of Ti-PMOs and PMO in the range of 2θ=4-50°.

A representative material, Ti20-PMO, was deeper characterized by TEM-HRTEM. Uniform mesoporous channels regularly distributed can be clearly seen in TEM micrographs (Figure 3.6a). Figure 3.6b shows uniform and parallel channels with wavy contrast of 4.5 nm. The electron diffraction pattern in the inset of Figure 3.6b shows spots at 45 Å corresponding to the size of the parallel channels; the diffraction ring at 10.8 Å is consistent with the molecular periodicity of biphenyl groups determined by XRD.

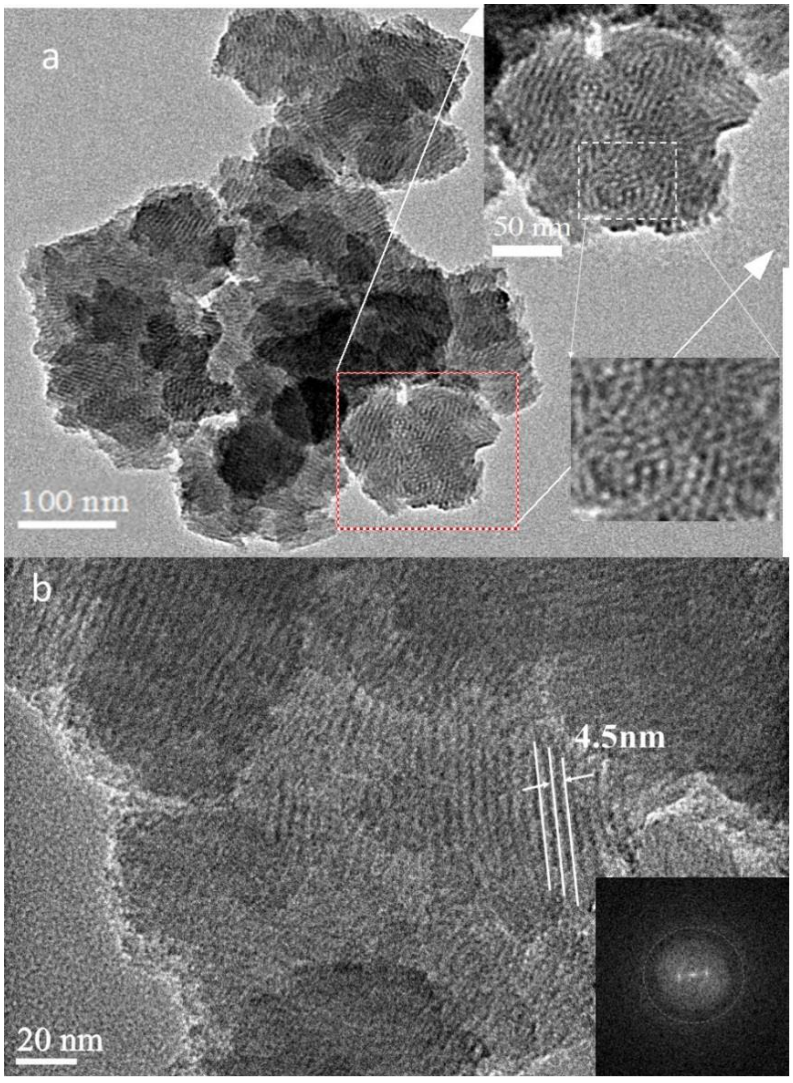

Figure 3.6. TEM images of the Ti20-PMO sample: **a)** in the inset, [001] incidental beam parallel to the channels; **b)** in the marked zone [100] incidental beam perpendicular to the channels, electron diffraction pattern with spots at 4.5 nm and ring diffraction at 1.08 nm.

The combined FTIR and Raman spectroscopy characterization helped us to analyze the organic functional groups present in the systems and give further information about structural details. FTIR spectra of PMO and Ti-PMOs are shown in Figure 3.7.

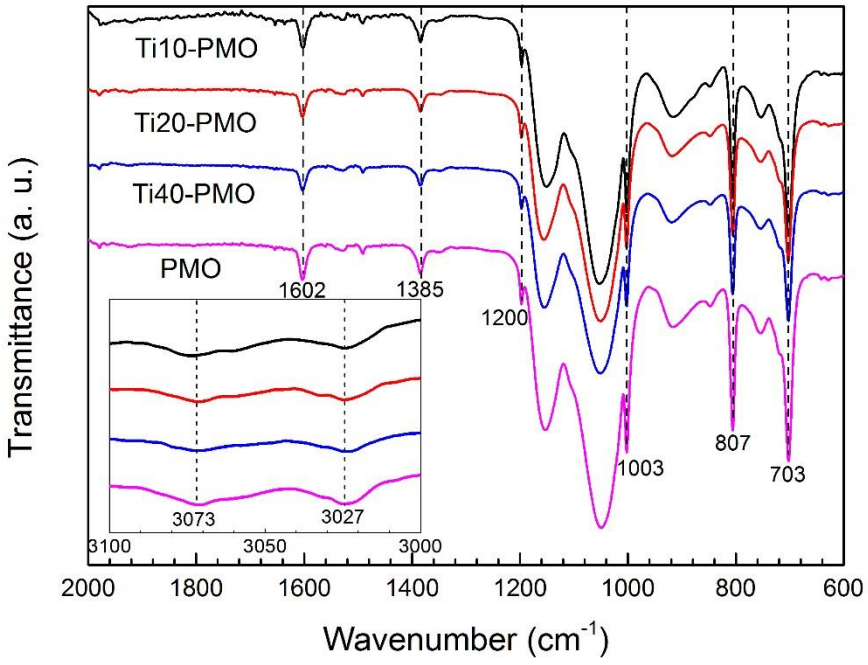

Figure 3.7. ATR-FTIR spectra of Ti-PMOs and PMO.

Besides the characteristic band due to Si-O-Si (1110-990 cm^{-1}), the infrared spectrum of PMO shows bands due to biphenyl group: 3073 and 3027 cm^{-1} (υ(C-H)), 1602 and 1003cm^{-1} (υ(ring-CC)), 1385cm^{-1} (δ(ring-CH)), 1200 cm^{-1} (inter ring stretching vibration), and 807 and 703 cm^{-1} bending C-C and C-H, respectively [4-6]. These bands are also present without apparent modification in the spectra of Ti-PMOs photocatalysts. This indicates that after the introduction of Ti into the PMO material, no changes occurred in the organic fragments.

Ti-PMOs show very similar Raman spectra to that of PMO (Figure 3.8). Raman bands of the bridged-biphenyl groups assigned to υ(ring C-C) at 1599 cm^{-1}, $\delta(C\text{-}H)_{i.p}$ at 1512 cm^{-1} and 1135 cm^{-1}, and central υ(C-C) at 1282 cm^{-1} can be identified in all cases [4].

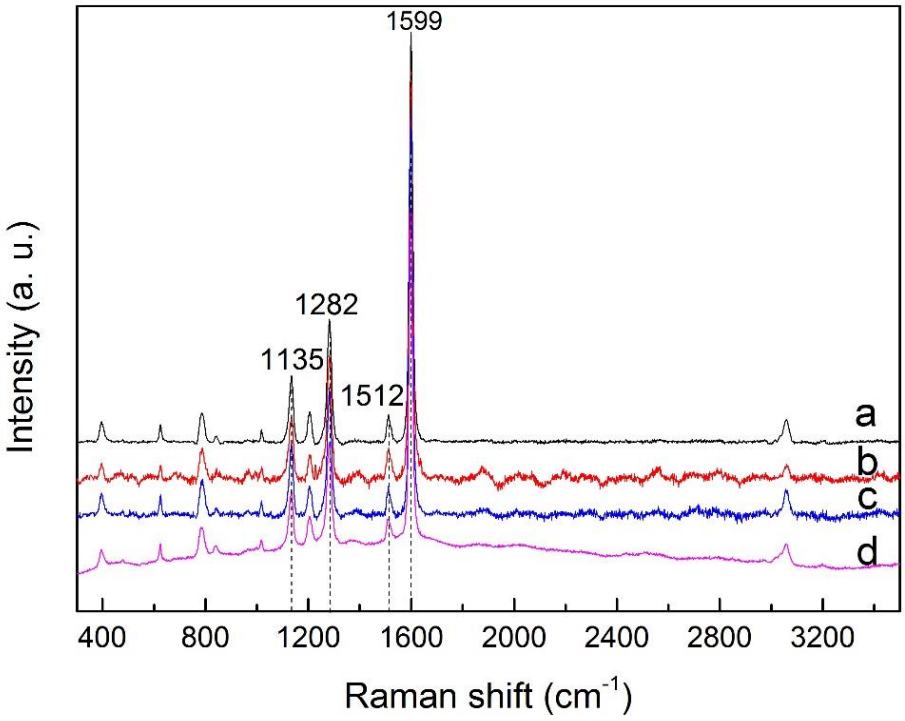

Figure 3.8. Raman spectra of samples: **a**) PMO; **b**) Ti10-PMO; **c**) Ti20-PMO; **d**) Ti40-PMO.

UV-vis DRS and XPS could be useful techniques to give information about the characteristics of Ti species in the mesoporous Ti-PMOs. The detection of tetrahedral Ti (IV) species could evidence the incorporation of Ti into the PMO structure.

However, the UV-vis DRS spectra of Ti-PMOs are very similar to that of PMO (Figure 3.9). The broad band centered at 250-300 nm, is related with the presence of biphenyl groups [7-9], but it could be also contributed by the presence of isolated tetrahedral Ti^{4+} species in the Ti-PMOs structure [10,11].

On the other hand, the Ti10-PMO photocatalyst which contains the highest Ti content shows a shoulder above 300 nm, which could be related with the presence of octahedral Ti^{4+} species [12].

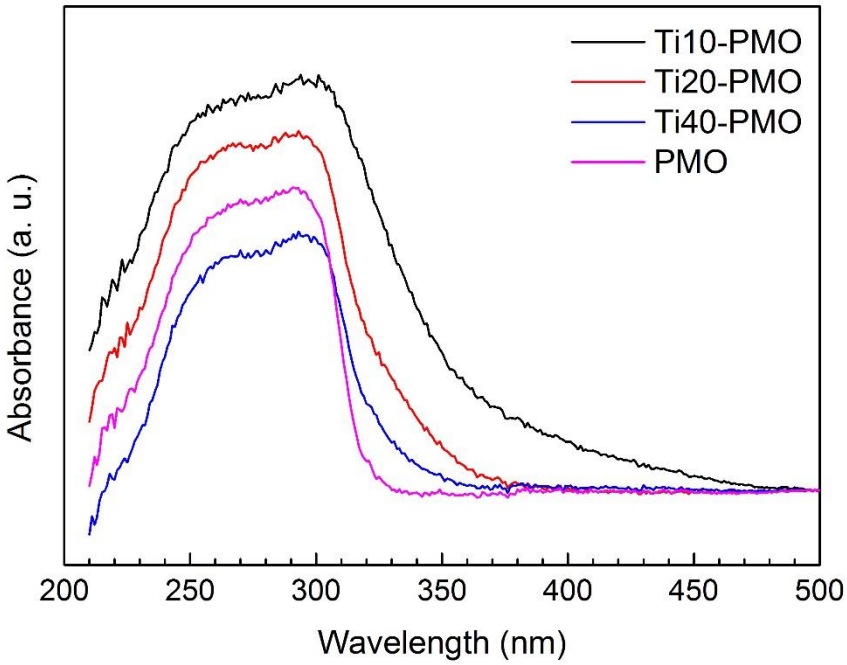

Figure 3.9. UV-visible diffuse reflectance spectra of Ti-PMOsand PMO.

As stated in the experimental section, for the determination of bandgap values, the corresponding Tauc plot, $(F(R\infty)\cdot h\nu)^n$ versus $h\nu$ was used (Figure 3.10) [13].

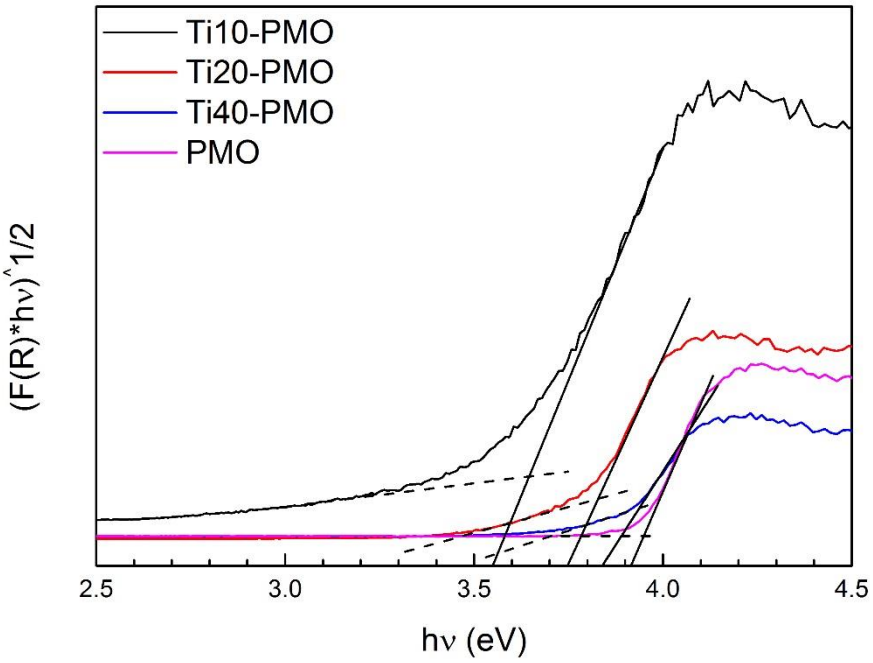

Figure 3.10. Tauc's plot of Ti-PMOs and PMO for bandgap determination.

The bandgap values of the catalysts (Table 3.2) were well-above those expected for pure TiO_2 anatase, or rutile, 3.2 eV and 3.0 eV, respectively [14, 15]. The bandgap of Ti-PMOs decreases with the increase of Ti content following the order: Ti40-PMO>Ti20-PMO>Ti10-PMO. The bandgap of PMO is similar to that determined for the Ti40-PMO photocatalyst with the lowest Ti loading.

Table 3.2. The Ti $2p_{3/2}$ binding energy values and bandgap of Ti-PMOs and PMO catalysts.

Sample	Ti $2p_{3/2}$ BE (eV)	Bandgap (eV)
PMO	--	3.95
Ti10-PMO	458.7, 459.5	3.65
Ti20-PMO	459.7	3.83
Ti40-PMO	460.2	3.91

Figure 3.11 shows Ti 2p core-level spectra of samples. The very low intensity of Ti 2p spectrum for Ti40-PMO does not allow an appropriate determination of the surface Ti species for this material.

However, for Ti10-PMO and Ti20-PMO, two well-resolved peaks corresponding to Ti $2p_{3/2}$ and Ti $2p_{1/2}$ levels can be observed (Figure 3.11). The Ti $2p_{3/2}$ peak of Ti20-PMO, centered at 459.7 eV, can be related with the presence of tetrahedral Ti(IV) [16-18], according to the intercalation of Ti(IV) in the PMO framework. For Ti10-PMO with the highest Ti content, the Ti $2p_{3/2}$ spectrum can be deconvoluted into two components. The component at the highest BE is related with the presence of tetrahedral Ti(IV); the component at about 458.0 eV could indicate the presence of octahedral Ti(IV) in Ti10-PMO [16-18] in agreement with the UV-vis DRS results.

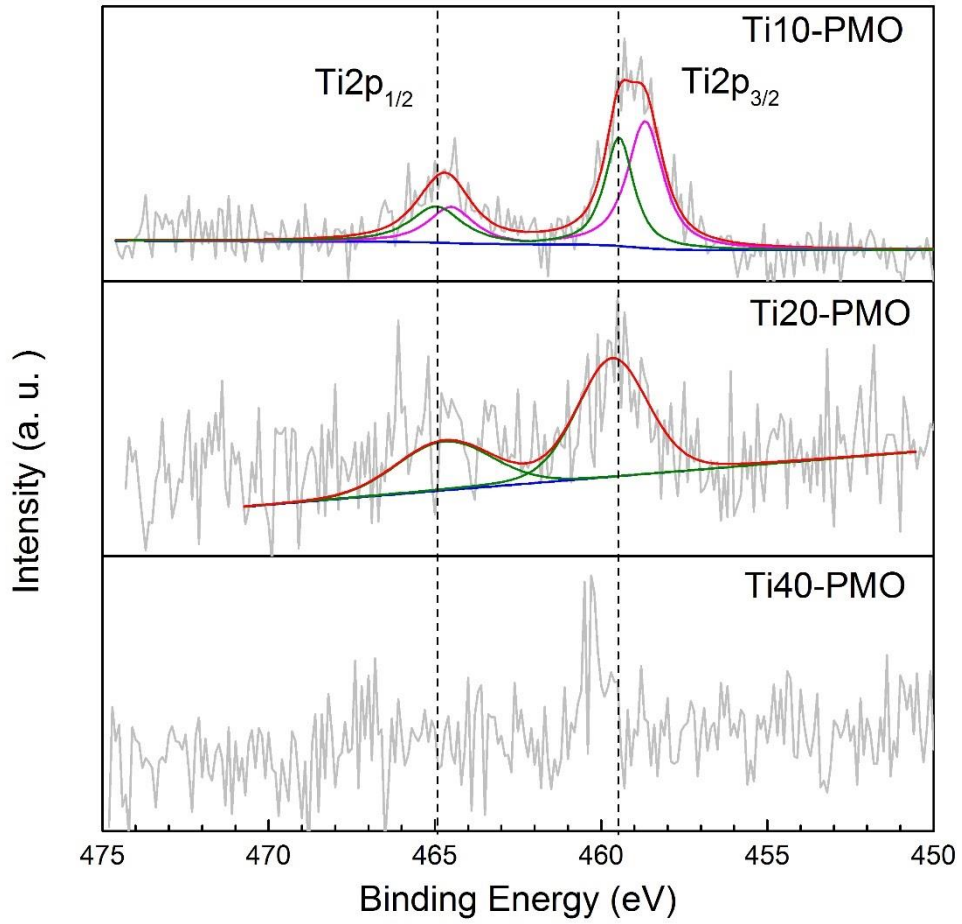

Figure 3.11. Ti 2p core-level spectra of Ti-PMOs.

The PL emission spectra of Ti-PMOs and PMO are shown in Figure 3.12. A broad emission band with maxima at about 440 nm can be observed for PMO. The PL emission spectra of Ti-PMOs exhibit bands with maxima in the 360-370 nm region. The excimer emission due to the interaction of close biphenyl groups could account for the observed bands [19-21].

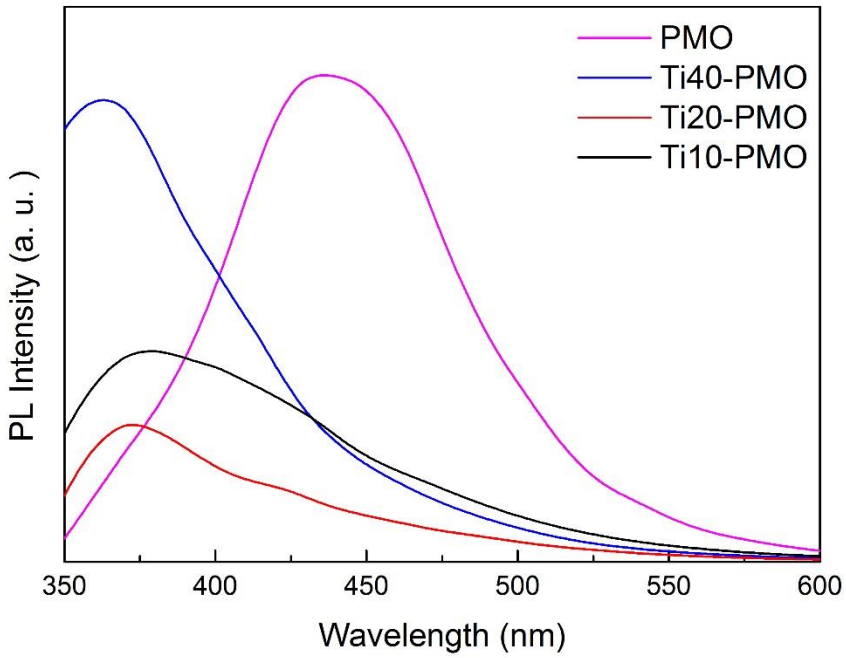

Figure 3.12. PL emission spectra of Ti-PMOs and PMO.

For Ti-PMO materials, the presence of Ti^{4+} into the framework of the PMO could modify in some extension the interaction within vicinal biphenyl-bridge groups.

The PL analysis of Ti-PMOs (Figure 3.12) shows that the intensity of the band depends on the Ti(IV) content of the samples, following the order PMO>Ti40-PMO>>Ti10-PMO>Ti20-PMO. The PL band intensity is usually related with the recombination rate of photo-induced charge carriers [22]. In general, the weaker the PL band intensity, the lower the recombination rate of the photo-induced charges; that is, the generated photoelectron has a longer lifetime. For Ti-PMOs photocatalysts, upon light absorption, a ligand-to-metal charge transfer could occur with a long-lived excited charge separation state, transferring the electron from the organic entity to the Ti^{4+} center. The radiative decay process from the excited state to the ground state could be slow down

when highly dispersed Ti^{4+} species having tetrahedral coordination are introduced into the PMO framework [23-25].

The transient photocurrent response spectra of Ti-PMOs and PMO samples under simulated solar irradiation in a pulse light on-off process are shown in Figure 3.13. Ti-PMOs samples show larger photocurrent density than PMO, with the order: Ti20-PMO>Ti10-PMO>Ti40-PMO>>PMO. Ti20-PMO which shows the lowest recombination rate of the photoinduced charge also has the highest photocurrent response.

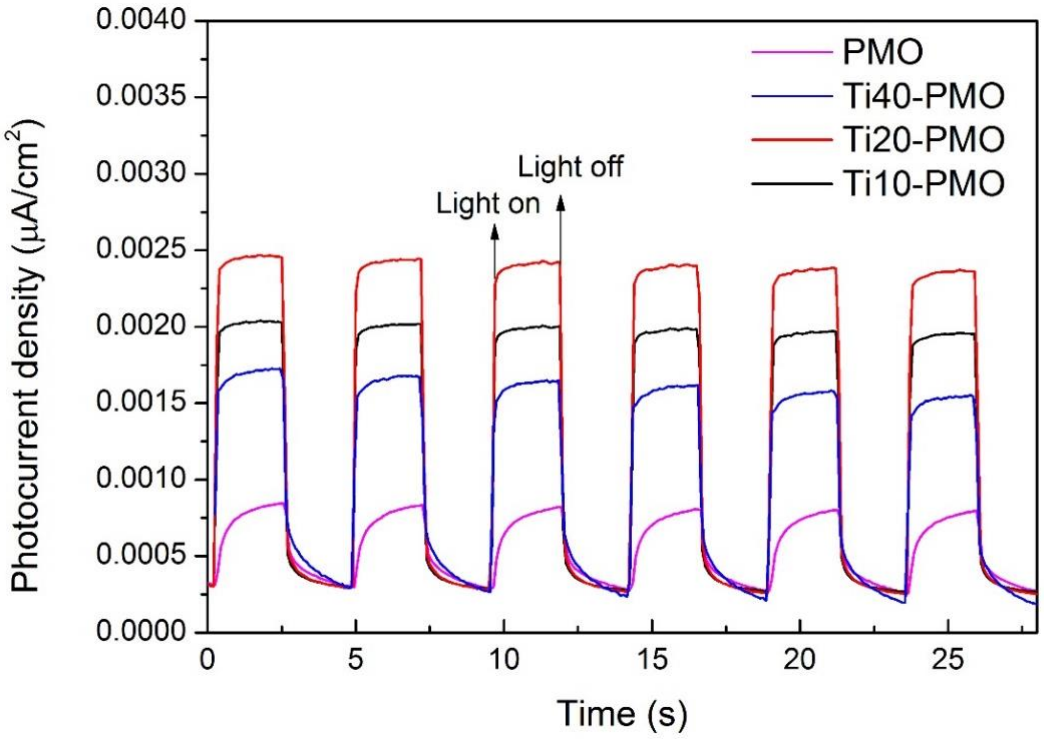

Figure 3.13. Photocurrent response of Ti-PMOs and PMO samples.

Figures 3.14 and 3.15 show the EIS Nyquist plots of Ti-PMOs and PMO which were obtained in dark and under simulated solar irradiation, respectively.

The barrier for the transfer of photogenerated electrons is related with the arc radius of the curve, the lower the transfer resistance, the smaller the arc radius.

In all cases, the arc radius under irradiation is smaller than in dark conditions. Ti-PMOs show smaller arc radius than PMO, which suggests that the presence of Ti^{4+} species can reduce the transfer resistance of the photogenerated charge and facilitate its transfer in Ti-PMOs materials. The Nyquist arc radius follows the order: PMO>>Ti40-PMO>Ti10-PMO>Ti20-PMO in both, dark and irradiated conditions. The presence of isolated Ti(IV) in the framework of Ti20-PMO is related with the lower barrier for the transfer of the photogenerated electrons.

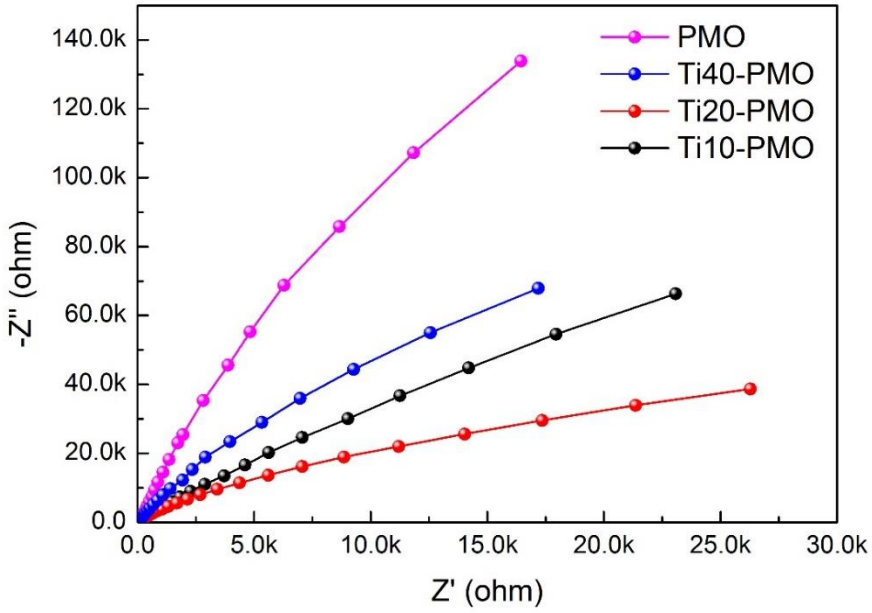

Figure 3.14. EIS Nyquist plots of Ti-PMOs and PMO samples in dark.

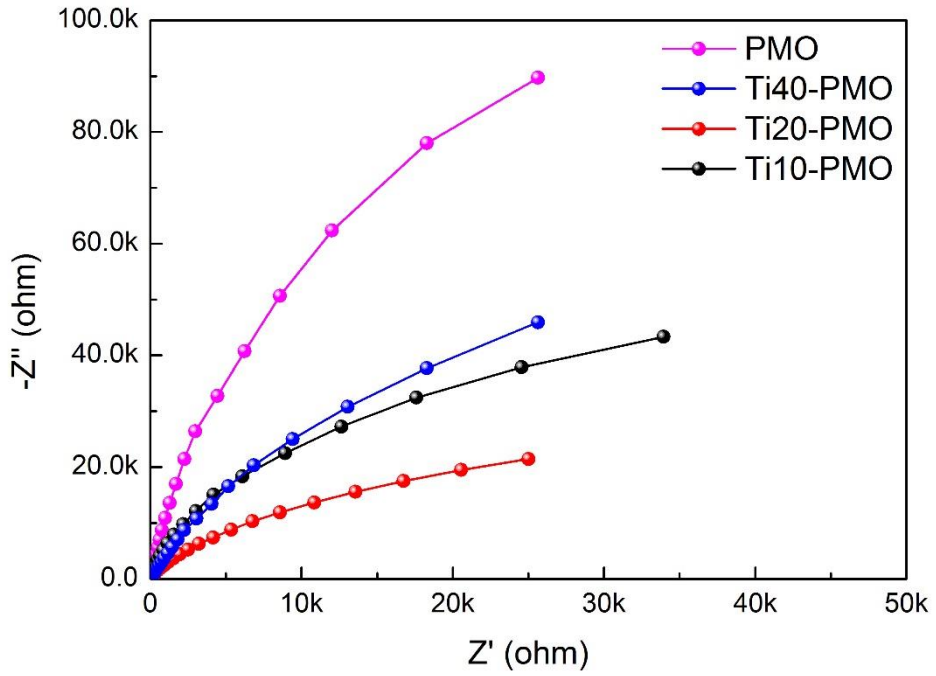

Figure 3.15. EIS Nyquist plots of Ti-PMOs and PMO samples under simulated solar irradiation.

3.3 Photocatalytic CO_2 reduction over Ti-PMOs

As stated above, we analyzed the photocatalytic behaviour of Ti-PMOs in the CO_2 photoreduction using the widely employed TEOA as SED. For comparative purposes, not only PMO but also commercial TiO_2 (P25) as references, were tested.

Photocatalysts (300 mg) were dispersed in 200 mL of a 10% v/v triethanolamine (TEOA) aqueous solution previously purged with Ar; the mixture was stirred under Ar flow for 30 min and then the flow was switched to CO_2 (50 mL min^{-1}) keeping stirring and dark conditions for 90 min more. Afterward, the light was switched on, and after 10 min, the evolved gaseous products were periodically sampled and online analyzed. No products in the

gas phase were detected under dark. A blank experiment using Ti20-PMO and Ar instead of CO_2 was also carried out.

Table 3.3 shows the products detected during the CO_2 photoreaction after 4 h of irradiation using a 10% v/v solution of TEOA over different photocatalysts. In all cases, besides C1 compounds (CO, CH_4), H_2 and unexpected C2 products (C_2H_4, CH_3CHO) were determined; the presence of O_2 was not detected. In the photocatalytic tests carried out using Ti20-PMO and Ar instead of CO_2, CO, CH_4, C_2H_4 and CH_3CHO were also found. However, the amount of carbon-containing products was much lower than when CO_2 was used (Table 3.3). This denotes that a part of the C1 and C2 found could be related with the transformation of CO_2. However, the transformation of TEOA under the irradiation conditions could also contribute to the C1 and C2 formation.

Table 3.3. Products obtained ($\mu mol/g_{cat}$) during the photocatalytic CO_2 reduction tests using a 10% v/v TEOA solution and different photocatalysts under UV-vis irradiation. Other reaction conditions: 50 mL min^{-1} CO_2, 20 °C, t=4 h.

Catalyst	H_2	CO	CH_4	C_2H_4	CH_3CHO
Ti10-PMO	2507	4252	2431	1298	4276
Ti20-PMO	1920	2210	2405	1248	4026
Ti40-PMO	2312	3968	2232	1250	4282
PMO	1765	3247	1861	1019	4189
P25	2688	3870	2095	1098	4439
Ti20-PMO*	1219	662	454	379	459

*test carried out with Ar instead of CO_2

In order to study the degradation of TEOA under UV-vis irradiation, we carried out three more tests with different TEOA concentrations (2.5, 5, 10 % v/v) in the absence of photocatalyst and keeping all the other experimental conditions.

Results in Table 3.4 point to the TEOA degradation under UV-vis irradiation forming small amounts of H_2, CO, CH_4, C_2H_4 and CH_3CHO. One could propose an easy formation of C2 species from TEOA irradiation, which could further produce CH_4, CO and H_2 [26]. These results bring to light the difficulty of determining the photocatalytic performance in the CO_2 reduction using TEOA as SED under UV-Vis irradiation conditions. In the light of these results, we investigated the behaviour of the Ti-PMOs in the photocatalytic production of H_2 from aqueous solutions of ethanol.

Table 3.4. Products determined (μmol) from the degradation of aqueous solutions of TEOA at different concentrations under irradiation without catalyst under UV-vis irradiation. Other reaction conditions: 50 mL min^{-1} CO_2, 20 °C, t=4 h.

TEOA (% v/v)	H_2	CO	CH_4	C_2H_4	CH_3CHO
10	708	1088	624	327	1075
5	337	991	508	275	1027
2.5	192	766	416	228	605

3.4 Photocatalytic H_2 production over Ti-PMOs

The photocatalytic H_2 production was studied using in all cases 370 mg of photocatalyst and 250 mL of an $ethanol_{(aq)}$ (25% v/v) solution, previously purged with Ar. After 30 min of stirring under Ar flow and dark conditions, the

suspension was irradiated, and after 10 min of light-on, the evolved gaseous products were periodically sampled and online analyzed. At the end of the reaction test (4 h), the solution was also analyzed by gas chromatography.

Figures 3.16 and 3.17 show the total H_2 yield and the rate of H_2 production, respectively, during the 4h of the photocatalytic test. As can be observed, all Ti-PMOs presented higher activity than PMO, which in turn was more active than P25. The amount of H_2 produced followed the order: Ti20-PMO>Ti10-PMO>Ti40-PMO>>PMO> P25.

This order was also kept when the H_2 yield per m^2 is considered (Figure 3.18). Among the Ti-PMOs, Ti20-PMO produced the highest amount of H_2. This is related with photoelectrochemical characteristics of Ti20-PMO discussed above. Ti20-PMO showed the lowest rate of charge recombination and the easiest charge transfer.

For the more active Ti20-PMO and Ti10-PMO photocatalysts analyzed, no apparent deactivation occurs along the reaction time (Figure 3.17).

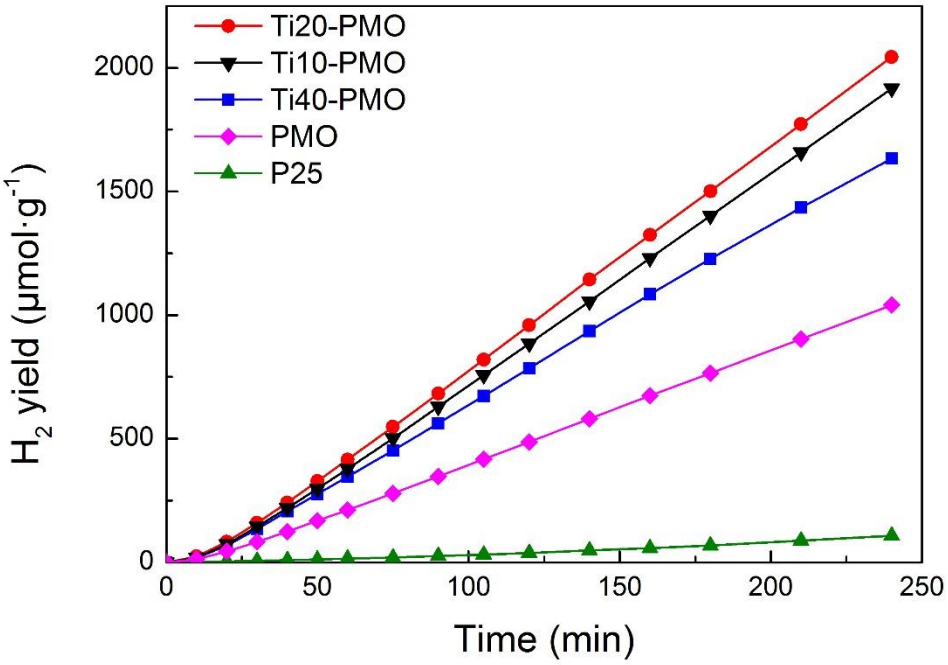

Figure 3.16. Total H_2 yield per gram of catalysts produced from ethanol$_{(aq)}$ 25% v/v over Ti-PMOs, PMO and P25. t= 4 h, T= 20 °C, UV-vis irradiation.

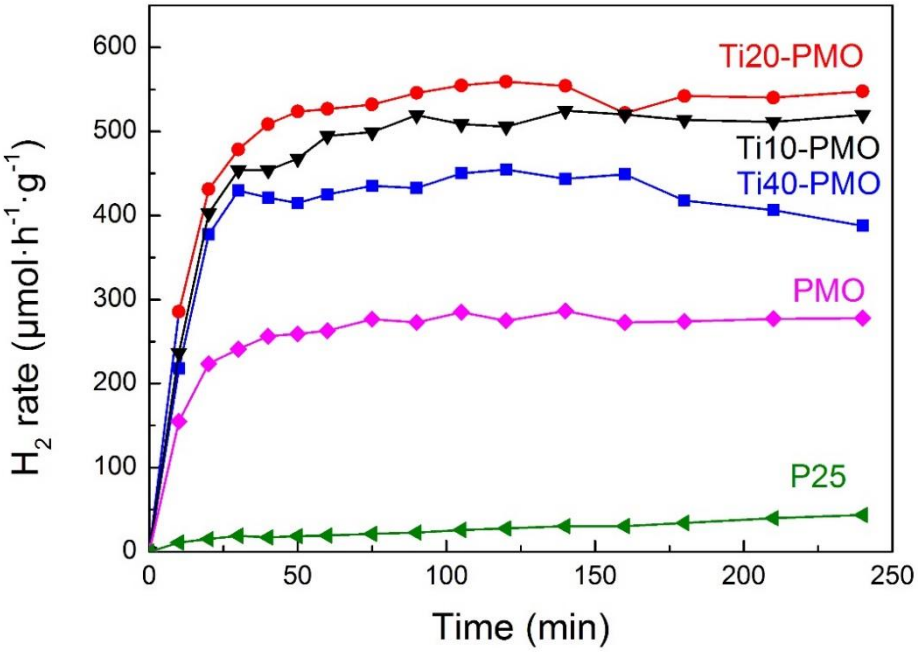

Figure 3.17. Rate of H_2 production from ethanol$_{(aq)}$ 25% v/v over Ti-PMOs, PMO and P25 photocatalysts. t= 4 h, T= 20 °C, UV-vis irradiation.

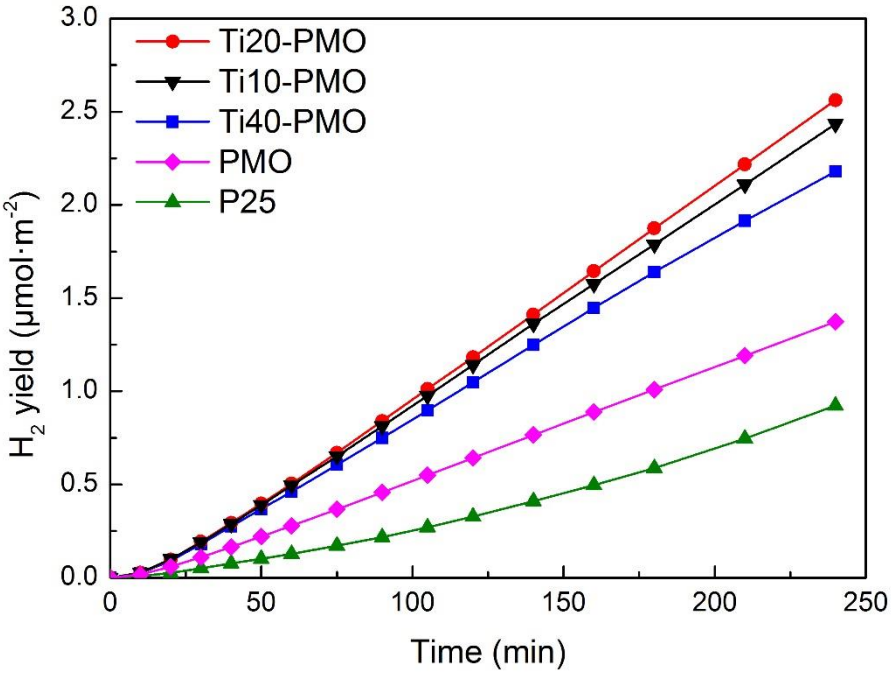

Figure 3.18. Total H_2 yield per m^2 produced from ethanol$_{(aq)}$ 25% v/v over Ti-PMOs, PMO and P25. t= 4 h, T= 20 °C, UV-vis irradiation.

The calculated AQE values are shown in Figure 3.19. Ti-PMOs are much more efficient photocatalytic systems than TiO_2 (P25); moreover, the introduction of Ti in the PMO framework enhances the photocatalytic activity. The highest AQE was 0.38% for Ti20-PMO photocatalyst, which is remarkably higher than that obtained for TiO_2 (P25) (<0.03%). On the other hand, the dependence of AQE on experimental details could hinder a straightforward comparison with data from other works, in particular when excitation sources with different intensities and wavelengths are used [27].

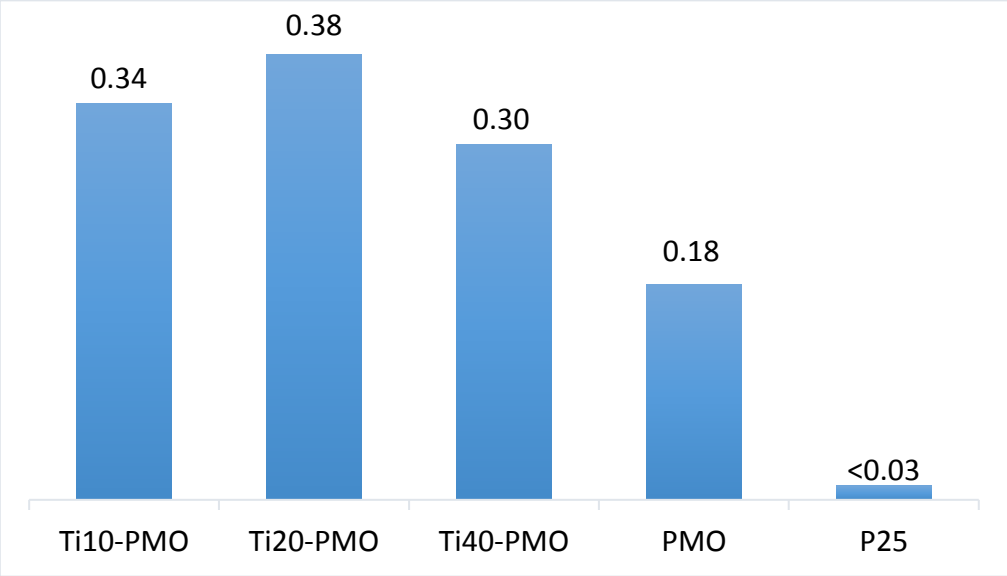

Figure 3.19. AQE (%) for H_2 production from ethanol$_{(aq)}$ 25% v/v for Ti-PMOs, PMO and P25 photocatalysts.

For a more complete analysis of the photocatalytic results, Figures 3.20 and 3.21 show the yield and rate of H_2 production referred to the Ti content of Ti-PMOs and the reference P25 during the 4 h of the photocatalytic tests, respectively. As can be observed, Ti-PMOs are much more effective per Ti centre than P25. Among Ti-PMOs, Ti10-PMO exhibited the lowest H_2 production rate per Ti centre. For this sample, with the highest Ti content among the Ti-PMOs materials, not all the Ti centres could be equally effective. As discussed above, the presence of extraframework octahedral Ti(IV) species can be proposed to be present in Ti10-PMO.

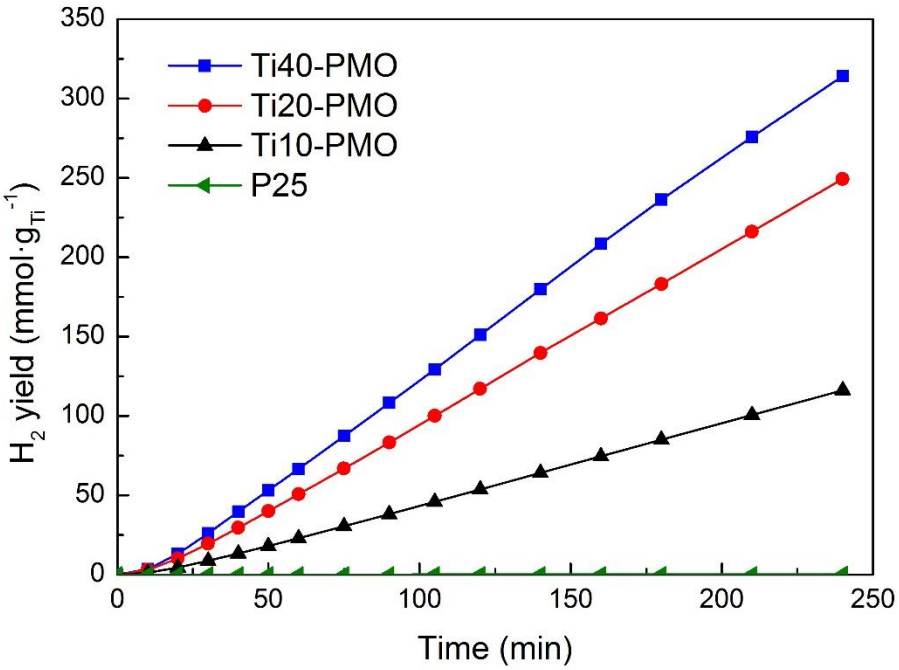

Figure 3.20. Total H_2 yield per gram of Ti produced from ethanol$_{(aq)}$ 25% v/v over Ti-PMOs and P25. t= 4 h, T= 20 °C, UV-vis irradiation.

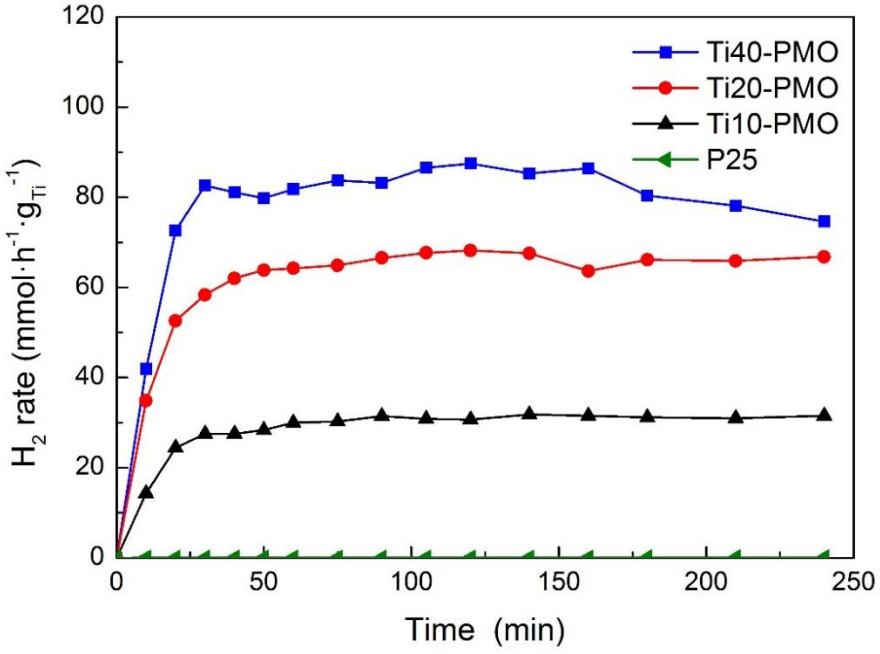

Figure 3.21. Rate of H_2 production per gram Ti from ethanol$_{(aq)}$ 25% v/v using Ti-PMOs, PMO and P25 photocatalysts. t= 4 h, T= 20 °C, UV-vis light irradiation.

Besides H_2, 2,3-butanediol and minor amounts of CO, CH_4, C_2H_4 and CH_3CHO were obtained (Table 3.5); O_2 or CO_2 were not detected. The coupling of two α-hydroxyethyl radicals ($\cdot CH(OH)CH_3$) could account for 2,3-butanediol formation [28].

$$CH_3CH_2OH + h^+ \rightarrow \cdot CH(OH)CH_3 + H^+ \qquad (\mathbf{3.1})$$

$$2 \cdot CH(OH)CH_3 \rightarrow CH_3CH(OH)CH(OH)CH_3 \qquad (\mathbf{3.2})$$

Once α-hydroxyethyl radicals are formed (Eq. 3.1), acetaldehyde could be also produced [26,28-30].

$$\cdot CH(OH)CH_3 + h^+ \rightarrow CH_3CHO + H^+ \qquad (\mathbf{3.3})$$

We relate the 2,3-butanediol formation with the pore characteristics of Ti-PMOs photocatalysts as it has been shown for other TiO_2-based systems; a higher amount of 2,3-butanediol has been found when Pt/TiO_2 photocatalysts with a smaller pore size (in the range 4.5-30 nm) have been used [29].

The no detection of acetic acid or CO_2 points that successive oxidation pathways of acetaldehyde are minor.

Table 3.5. Products obtained (μmol/g_{cat}) during the photocatalytic H_2 production tests using ethanol$_{(aq)}$ 25% v/v and different photocatalysts under UV-vis irradiation. Other reaction conditions: 20 °C, t=4 h.

Catalysts	H_2	CO	CH_4	C_2H_4	CH_3CHO	2,3-butanediol
Ti10-PMO	1916	97	79	25	46	819
Ti20-PMO	2044	71	88	24	44	1285
Ti40-PMO	1633	95	73	26	46	947
PMO	1041	56	58	18	46	1395
P25	108	163	102	105	<10	233

3.5 Characterization of post-reaction Ti-PMOs

Ti-PMOs were characterized by several techniques after the photocatalytic transformation of aqueous ethanol solution.

Fresh and used catalysts showed similar XRD patterns (Figure 3.22 and 3.23), adsorption-desorption N_2 isotherms (Figure 3.24) and FTIR spectra (Figure 3.25). No significant variation in the BET surface area was found after photocatalytic tests, see Table 3.6 and Table 3.1 (p. 80). These results indicate that Ti-PMOs keep their characteristics under the photocatalytic test conditions.

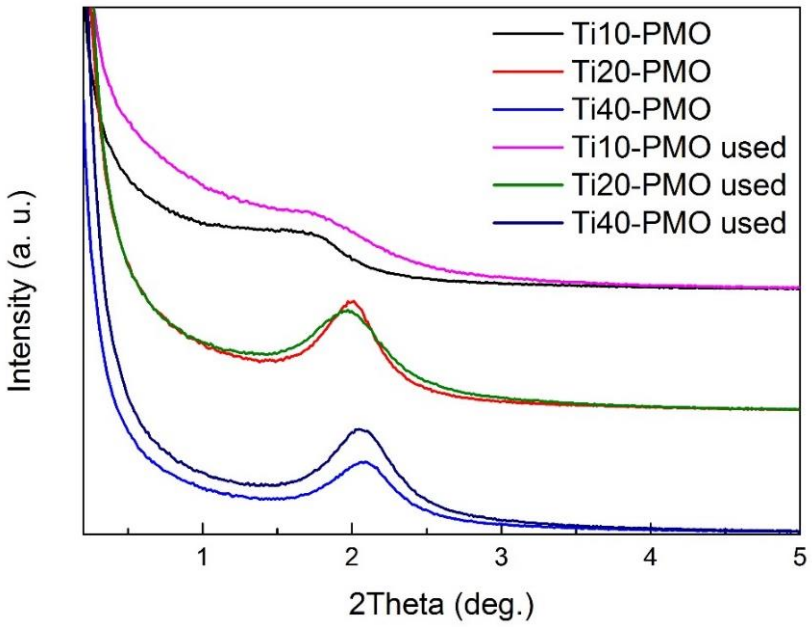

Figure 3.22. XRD patterns of Ti-PMOs materials in the low-angle region (0.2<2θ<5°) after the photocatalytic H_2 production from ethanol$_{(aq)}$ 25% v/v at 20 °C for 4 h.

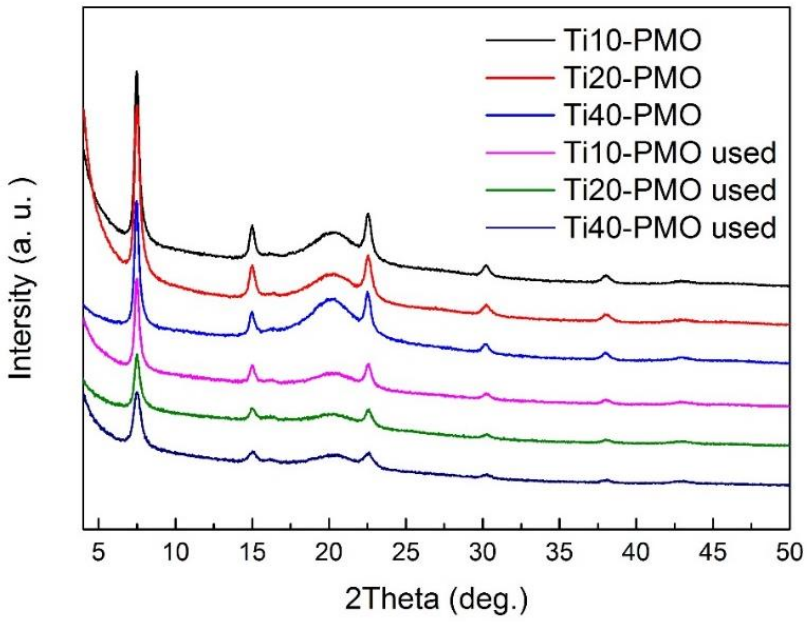

Figure 3.23. XRD patterns of Ti-PMOs materials in the region of 5<2θ<50° after the photocatalytic H_2 production from ethanol$_{(aq)}$ 25% v/v at 20 °C for 4 h.

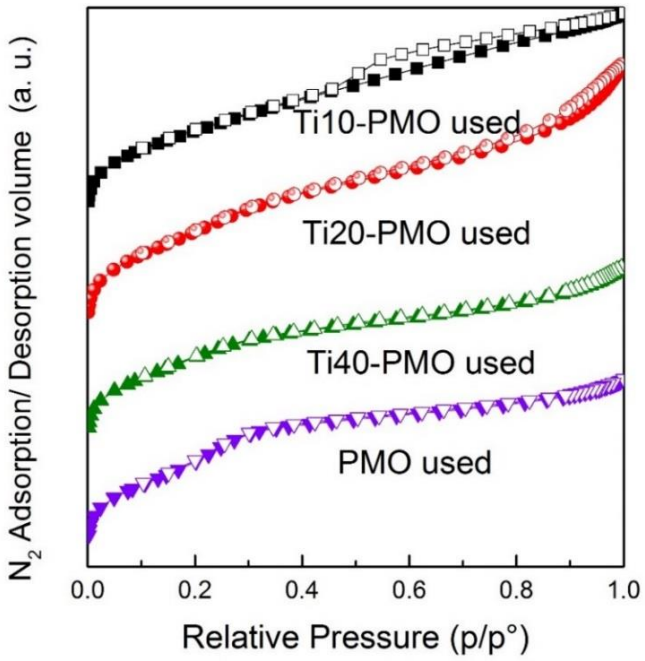

Figure 3.24. N_2 adsorption-desorption isotherms at -196 °C of PMO and Ti-PMOs materials after the photocatalytic H_2 production from ethanol$_{(aq)}$ 25% v/v at 20 °C for 4 h.

Table 3.6. BET surface area of Ti-PMOs and PMO materials after using (4 h) in the photocatalytic H_2 production from ethanol$_{(aq)}$ 25% v/v at 20 °C.

Post reaction photocatalyst	**S_{BET} m^2g^{-1}**
Ti10-PMO	748
Ti20-PMO	840
Ti40-PMO	749
PMO	758

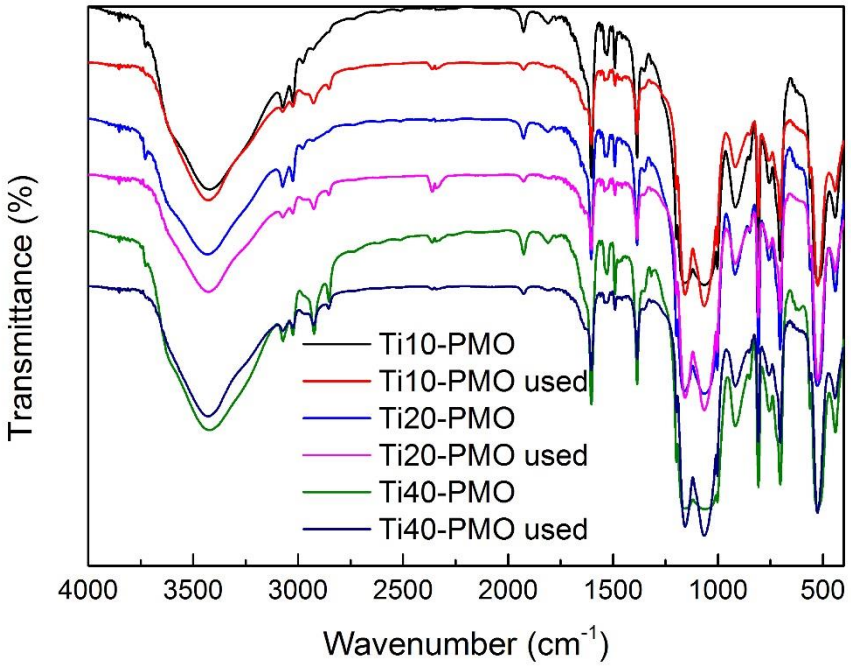

Figure 3.25. ATR-FTIR spectra of Ti-PMOs materials after the photocatalytic H_2 production from ethanol$_{(aq)}$ 25% v/v for 4 h at 20 °C.

For Ti10-PMO sample, after the photocatalytic reaction and before separating the catalysts from the liquid, it was possible to observe that the solid showed a greyish-blue colour (Figure 3.26).

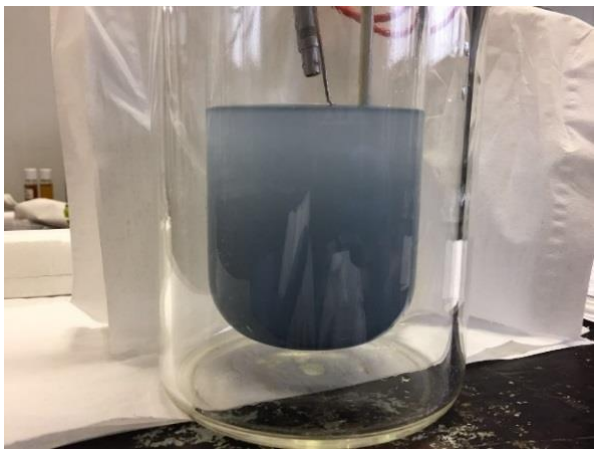

Figure 3.26. The reaction suspension of Ti10-PMO just turning off irradiation after the photocatalytic test of H_2 production from ethanol$_{(aq)}$ 25% v/v at 20 °C.

The corresponding XPS analysis of the post-reaction Ti10-PMO photocatalyst revealed a Ti $2p_{3/2}$ peak component at 457.1 eV (Figure 3.27), which could be assigned to the presence of Ti^{3+} species on the surface [31,32]. The existence of Ti^{3+} could play a main role in the photoreduction process, as has been reported for the CO_2 photoreduction [23-25].

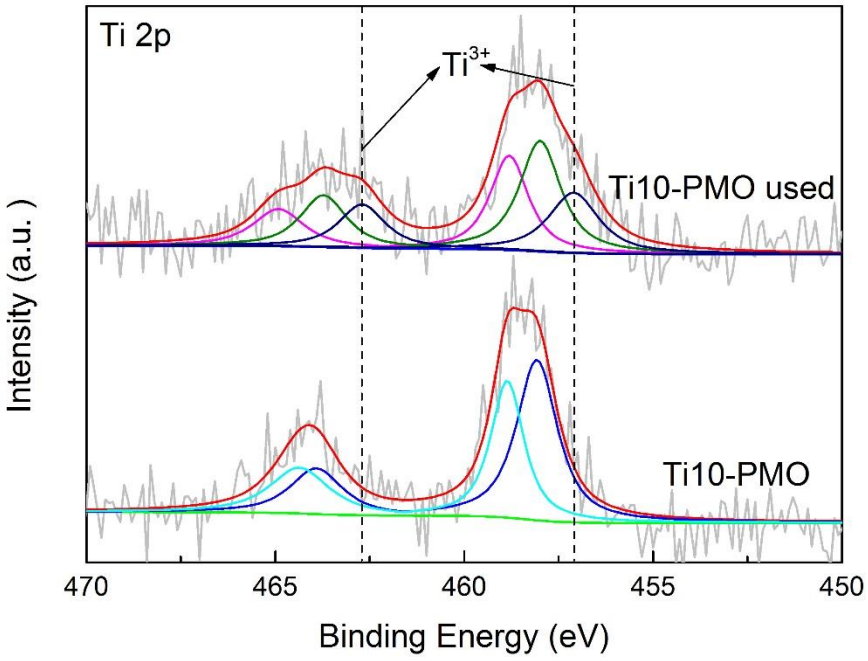

Figure 3.27. Ti 2p XPS spectrum of Ti10-PMO after the photocatalytic test of H_2 production from ethanol$_{(aq)}$ 25% v/v at 20 °C; the spectrum of fresh Ti10-PMO is also shown for comparison.

3.6 References

1. Wang Y, Homs N, Ramírez de la Piscina P. Ti-containing hybrid mesoporous organosilicas as photocatalysts for H_2 production from ethanol. Journal of Materials Research and Technology, 2021, 14: 2115-2123.

2. Kapoor M P, Yang Q, Inagaki S. Self-assembly of biphenylene-bridged hybrid

mesoporous solid with molecular-scale periodicity in the pore walls. Journal of the American Chemical Society, 2002, 124: 15176-15177.

3. Thommes M, Kaneko K, Neimark A V, et al. Physisorption of gases, with special reference to the evaluation of surface area and pore size distribution (IUPAC Technical Report). Pure and Applied Chemistry, 2015, 87: 1051-1069.

4. Hoffmann F, Güngerich M, Klar P J, et al. Vibrational Spectroscopy of Periodic Mesoporous Organosilicas (PMOs) and their precursors: a closer look. The Journal of Physical Chemistry C, 2007, 111: 5648-5660.

5. Constantinidis P, Schmitt H C, Fischer I, et al. Formation of polycyclic aromatic hydrocarbons from bimolecular reactions of phenyl radicals at high temperatures. Physical Chemistry Chemical Physics, 2015, 17: 29064-29071.

6. Katon J E, Lippincott E R. The vibrational spectra and geometrical configuration of biphenyl. Spectrochimica Acta, 1959, 15: 627-650.

7. Goto Y, Mizoshita N, Ohtani O, et al. Synthesis of mesoporous aromatic silica thin films and their optical properties. Chemistry of Materials, 2008, 20: 4495-4498.

8. Ohashi M, Aoki M, Yamanaka K, et al. A Periodic Mesoporous Organosilica-Based Donor–Acceptor System for Photocatalytic Hydrogen Evolution. Chemistry–A European Journal, 2009, 15: 13041-13046.

9. Gao M, Han S, Qiu X, et al. Biphenyl-bridged periodic mesoporous organosilicas: Synthesis and in situ charge-transfer properties. Microporous and Mesoporous Materials, 2014, 198: 92-100.

10. Morishita M, Shiraishi Y, Hirai T. Ti-containing mesoporous organosilica as

a photocatalyst for selective olefin epoxidation. The Journal of Physical Chemistry B, 2006, 110: 17898-17905.

11. Ikeue K, Yamashita H, Anpo M, et al. Photocatalytic reduction of CO_2 with H_2O on Ti−β Zeolite photocatalysts: effect of the hydrophobic and hydrophilic properties. The Journal of Physical Chemistry B, 2001, 105: 8350-8355.
12. Huang Y, Yuan P, Wu Z, et al. Preparation of surface-silylated and benzene-bridged Ti-containing mesoporous silica for cyclohexene epoxidation. Journal of Porous Materials, 2016, 23: 895-903.
13. Makuła P, Pacia M, Macyk W. How to correctly determine the band gap energy of modified semiconductor photocatalysts based on UV–Vis spectra. The Journal of Physical Chemistry Letters, 2018, 9: 6814-6817.
14. Leung D Y C, Fu X, Wang C, et al. Hydrogen production over titania-based photocatalysts. ChemSusChem, 2010, 3: 681-694.
15. Reyes-Coronado D, Rodríguez-Gattorno G, Espinosa-Pesqueira M E, et al. Phase-pure TiO_2 nanoparticles: anatase, brookite and rutile. Nanotechnology, 2008, 19: 145605.
16. Chu H Q, Yu C, Wan Y, et al. Synthesis of ordered mesoporous bifunctional TiO_2–SiO_2–polymer nanocomposites. Journal of Materials Chemistry, 2009, 19: 8610-8618.
17. Barrio L, Campos-Martín J M, de Frutos-Escrig M P, et al. Selective grafting of titanium on periodic nanoporous silica materials. Microporous and Mesoporous Materials, 2008, 113: 542-553.
18. Chandra D, Mal N K, Mukherjee M, et al. Titanium-rich highly ordered mesoporous silica synthesized by using a mixed surfactant system. Journal

of Solid State Chemistry, 2006, 179: 1802-1807.

19. Yamanaka K, Okada T, Goto Y, et al. Dynamics in the excited electronic state of periodic mesoporous biphenylylene-silica studied by time-resolved diffuse reflectance and fluorescence spectroscopy. Physical Chemistry Chemical Physics, 2010, 12: 11688-11696.

20. Cione A P P, Scaiano J C, Neumann M G, et al. The excimer emission of aromatic hydrocarbons on clays. Journal of Photochemistry and Photobiology A: Chemistry, 1998, 118: 205-209.

21. Okada T, Yamanaka K, Hirose Y, et al. Fluorescence studies on phenylene moieties embedded in a framework of periodic mesoporous organosilica. Physical Chemistry Chemical Physics, 2011, 13: 7961-7967.

22. Liqiang J, Yichun Q, Baiqi W, et al. Review of photoluminescence performance of nano-sized semiconductor materials and its relationships with photocatalytic activity. Solar Energy Materials and Solar Cells, 2006, 90: 1773-1787.

23. Fu Y, Sun D, Chen Y, et al. An amine-functionalized titanium metal–organic framework photocatalyst with visible-light-induced activity for CO_2 reduction. Angewandte Chemie International Edition, 2012, 51: 3364-3367.

24. Sorcar S, Hwang Y, Grimes C A, et al. Highly enhanced and stable activity of defect-induced titania nanoparticles for solar light-driven CO_2 reduction into CH_4. Materials Today, 2017, 20: 507-515.

25. Sorcar S, Thompson J, Hwang Y, et al. High-rate solar-light photoconversion of CO_2 to fuel: controllable transformation from C1 to C2 products. Energy & Environmental Science, 2018, 11: 3183-3193.

26. Sola A C, Homs N, Ramírez de la Piscina P. Photocatalytic H_2 production from ethanol$_{(aq)}$ solutions: The effect of intermediate products. International Journal of Hydrogen Energy, 2016, 41: 19629-19636.

27. Languer M P, Scheffer F R, Feil A F, et al. Photo-induced reforming of alcohols with improved hydrogen apparent quantum yield on TiO_2 nanotubes loaded with ultra-small Pt nanoparticles. International Journal of Hydrogen Energy, 2013, 38: 14440-14450.

28. Lu H, Zhao J, Li L, et al. Selective oxidation of sacrificial ethanol over TiO_2-based photocatalysts during water splitting. Energy & Environmental Science, 2011, 4: 3384-3388.

29. Sola A C, Ramírez de la Piscina P, Homs N. Behaviour of Pt/TiO_2 catalysts with different morphological and structural characteristics in the photocatalytic conversion of ethanol aqueous solutions. Catalysis Today, 2020, 341: 13-20.

30. Pajares A, Wang Y, Kronenberg M J, Ramírez de la Piscina P, et al. Photocatalytic H_2 production from ethanol aqueous solution using TiO_2 with tungsten carbide nanoparticles as co-catalyst. International Journal of Hydrogen Energy, 2020, 45: 20558-20567.

31. Diebold U. The surface science of titanium dioxide. Surface Science Reports, 2003, 48: 53-229.

32. Liu G, Pan J, Yin L, et al. Heteroatom-Modulated Switching of Photocatalytic Hydrogen and Oxygen Evolution Preferences of Anatase TiO_2 Microspheres. Advanced Functional Materials, 2012, 22: 3233-3238.

Chapter 4.

Study of Mo_xC/g-C_3N_4 nanocomposites in the photocatalytic H_2 production

In this chapter, the study of $Mo_xC/g\text{-}C_3N_4$ nanocomposites in the photocatalytic H_2 production is presented. The preparation of $Mo_xCT/g\text{-}C_3N_4$ nanocomposites containing hexagonal Mo_2C and/or cubic MoC nanoparticles onto graphitic carbon nitride nanosheets was carried out by using an ultrasonic-assisted method, and Mo_xC nanoparticles and $g\text{-}C_3N_4$ previously prepared. $Mo_xCT/g\text{-}C_3N_4$ photocatalysts were characterized using XRD, TEM, XPS, UV-Vis DRS, PL, and PEC measurements.

The $Mo_xCT/g\text{-}C_3N_4$ photocatalysts were active under visible irradiation (λ>385 nm) for the H_2 production from an ethanol aqueous solution (25% v/v). The photocatalytic behaviour of $Mo_xCT/g\text{-}C_3N_4$ was related with the characteristics of Mo_xC co-catalyst. Nanocomposites with smaller hexagonal Mo_2C particles presented a better photocatalytic behaviour. The most active photocatalyst was $Mo_xC700/g\text{-}C_3N_4$, containing both hexagonal Mo_2C and cubic MoC nanoparticles with a mean crystallite size of 11 and 4 nm, respectively. This photocatalyst showed the lowest rate of charge recombination, the lowest electron transfer resistance and the highest photocurrent response.

4.1 Preparation of $Mo_xC/g\text{-}C_3N_4$ photocatalysts

4.1.1 Synthesis of molybdenum carbides

Different phases of Mo_xC were synthesized on the basis of a sol-gel method previously developed in our group, using $MoCl_5$ and 4,5 dicyanoimidazole (DI) as molybdenum and carbon sources, respectively [1].

For Mo_xCT (T=700, 800, 900) preparation, 5.6 mmol of $MoCl_5$ and 2.8 mmol of DI were added into 15 mL of ethanol and treated at 60 °C in an oven under air to form a gel. Then, the gel was divided into three equal parts and treated respectively at different temperatures (700, 800, 900 °C) under Ar in a tubular furnace; the samples were named Mo_xCT (being T, the temperature of Ar treatment: 700, 800 and 900 °C). For Mo_xC1100 preparation, 5.6 mmol of $MoCl_5$ and 5.6 mmol of DI were added into 15 mL of ethanol. The gel obtained was placed in a tubular furnace and treated under Ar at 1100 °C.

4.1.2 Synthesis of $g\text{-}C_3N_4$ nanosheets

$g\text{-}C_3N_4$ nanosheets (named $g\text{-}C_3N_4$) were synthesized via the thermal polymerization of melamine [2]. In brief, melamine was heated under static air in a muffle furnace up to 520 °C (5 °C min^{-1}) and kept at this temperature for 4 h. After cooling down to room temperature, the yellow agglomerates were ground to a powder in a mortar. Then, the obtained samples were treated up to 520 °C again, following a similar procedure. Finally, $g\text{-}C_3N_4$ nanosheets with light yellow color were gotten.

4.1.3 Preparation of $Mo_xCT/g\text{-}C_3N_4$

$Mo_xCT/g\text{-}C_3N_4$ photocatalysts with about 3% wt of Mo_xCT were prepared using an ultrasonic-assisted method. Specifically, Mo_xCT (50 mg) and $g\text{-}C_3N_4$ (1 g) were dispersed in ethanol and treated under ultrasounds (SONICS VCX

500) at 20 °C for 1 h and 250W, then ethanol was carefully evaporated under continuous stirring at 50 °C. For comparative purposes, a photocatalyst prepared using commercial Mo_2C (Alfa-Aesar, 99.5%), Mo_2C-comm/g-C_3N_4, was similarly prepared. Figure 4.1 shows a schematic of the $Mo_xCT/g\text{-}C_3N_4$ synthetic procedure.

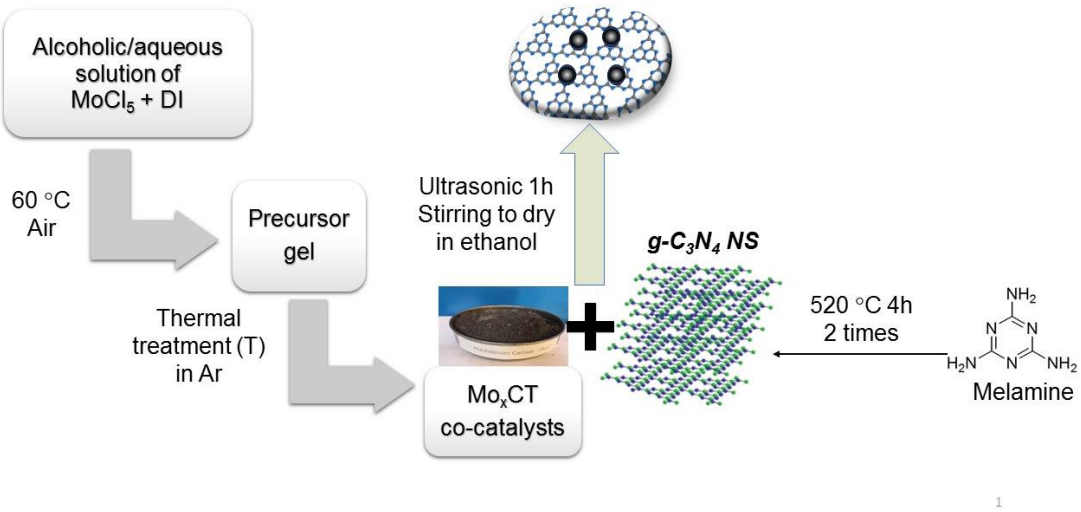

Figure 4.1. The synthesis procedure of $Mo_xCT/g\text{-}C_3N_4$ photocatalysts

4.2 Characterization of $Mo_xCT/g\text{-}C_3N_4$

XRD patterns of Mo_xCT and g-C_3N_4 used for the preparation of $Mo_xCT/g\text{-}C_3N_4$ photocatalysts are shown in Figures 4.2 and 4.3, respectively.

In the XRD patterns of Mo_xC800 and Mo_xC900, diffraction peaks at 2θ of 34.36, 37.98, 39.39, 52.12, 61.53, 69.57, 72.39, 74.65, 75. 52, 81.17 and 84.8° were detected. It indicates the presence of hexagonal Mo_2C (hcp, $P6_3/mmc$, PDF 04-014-1517) in Mo_xC800 and Mo_xC900, which from now are named Mo_2C800 and Mo_2C900, respectively. The XRD pattern of Mo_xC1100 shows diffraction peaks at 2θ of 36.42, 42.3, 61.36 and 73.5°, which can be attributed

to cubic MoC (ccp, Fm3m ,PDF 04-003-1480), from now this sample is named MoC1100. On the other hand, the coexistence of hexagonal Mo_2C and cubic MoC can be determined from the XRD pattern of Mo_xC700.

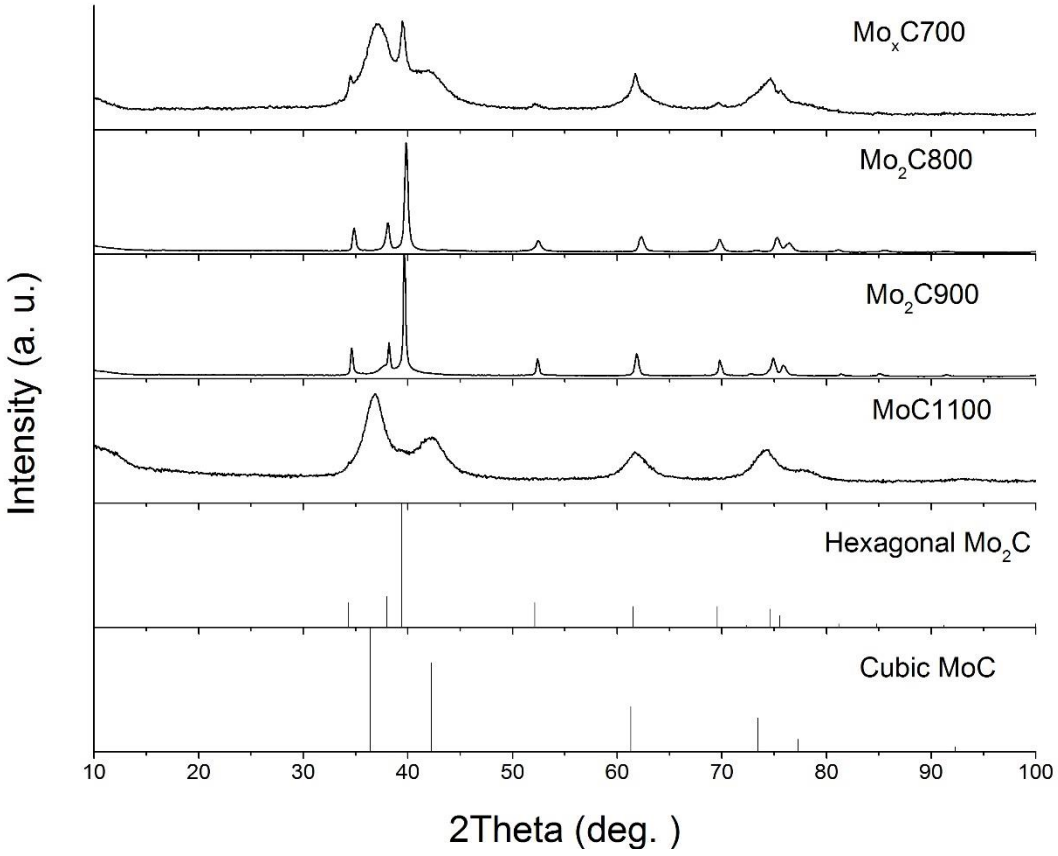

Figure 4.2. XRD patterns of Mo_xCT.

The diffraction pattern of g-C_3N_4 (Figure 4.3) shows a strong peak at 27.7°, corresponding to the (002) plane of graphitic materials, which is characteristic of the interplanar stacking of conjugated aromatic systems [2]. Bulk g-C_3N_4 presents the (002) XRD peak at 27,34°, this value of 2θ is slightly lower than the corresponding of g-C_3N_4 prepared in this work. It indicates a slight decrease in the interlayer distance for nanosheets with respect to bulk g-C_3N_4 [2-5]. The peak at 13.0° with very low intensity is indexed to the (100) plane and ascribed to intralayer periodicity [3].

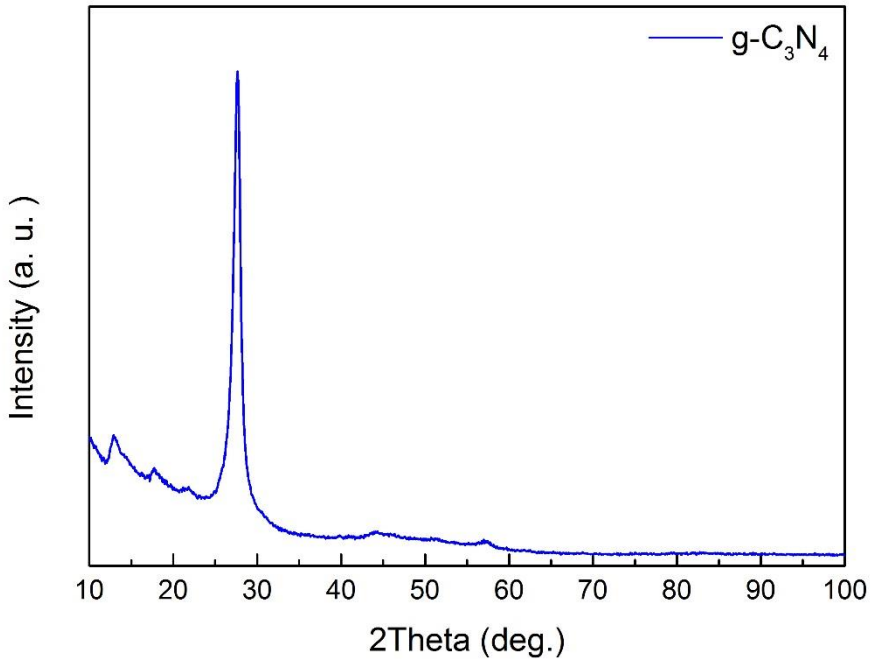

Figure 4.3. XRD pattern of $g\text{-}C_3N_4$.

The FTIR spectrum of $g\text{-}C_3N_4$ is shown in Figure 4.4. The broad absorption band from 3300 to 3000 cm^{-1} is attributed to the stretching vibration modes of N-H bonds resulting from the incomplete condensation of amino groups [2,4]. The sharp band at 807 cm^{-1} is assigned to the breathing mode of s-triazine rings in $g\text{-}C_3N_4$ and the bands in the 1800-900 cm^{-1} zone can be assigned to stretching C=N and C-N in the heterocycles [2,4,6,7].

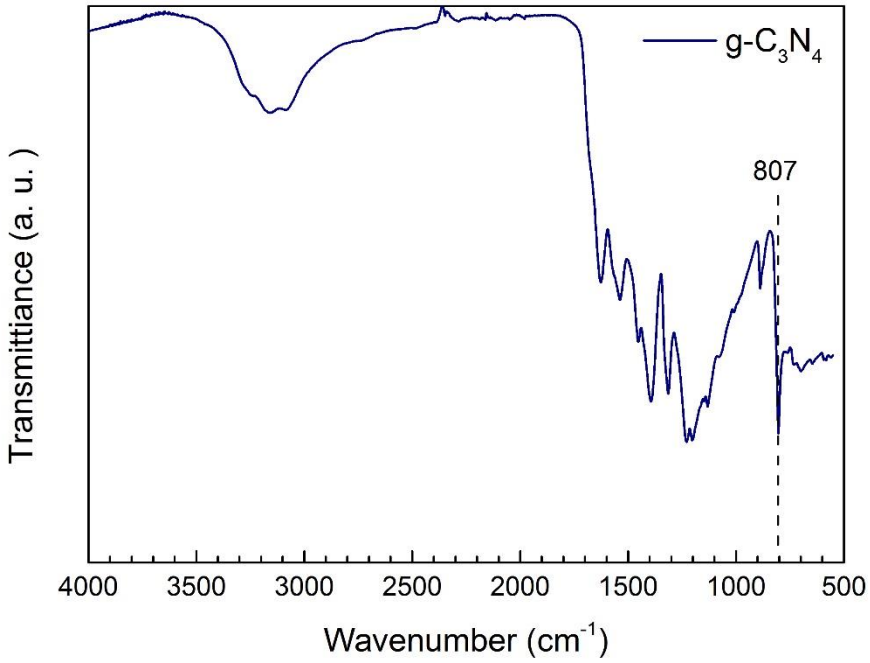

Figure 4.4. FTIR spectrum of g-C_3N_4.

Figure 4.5 shows the diffraction patterns of Mo_xCT/g-C_3N_4, Mo_2C-comm/g-C_3N_4 and g-C_3N_4 photocatalysts. In all cases, the initial crystalline phases in Mo_xCT were kept in Mo_xCT/g-C_3N_4 and Mo_2C-comm/g-C_3N_4. The two characteristic XRD peaks of g-C_3N_4 nanosheets were also present in all patterns. However, the (002) interlayer-stacking peak of Mo_xC900/g-C_3N_4, MoC1100/g-C_3N_4 and Mo_2C-comm/g-C_3N_4 samples were slightly shifted to lower angles comparing with g-C_3N_4 nanosheets (Table 4.1), which indicates a slight increase of g-C_3N_4 interlayer distance after the incorporation of Mo_2C900, MoC1100 and Mo_2C-comm.

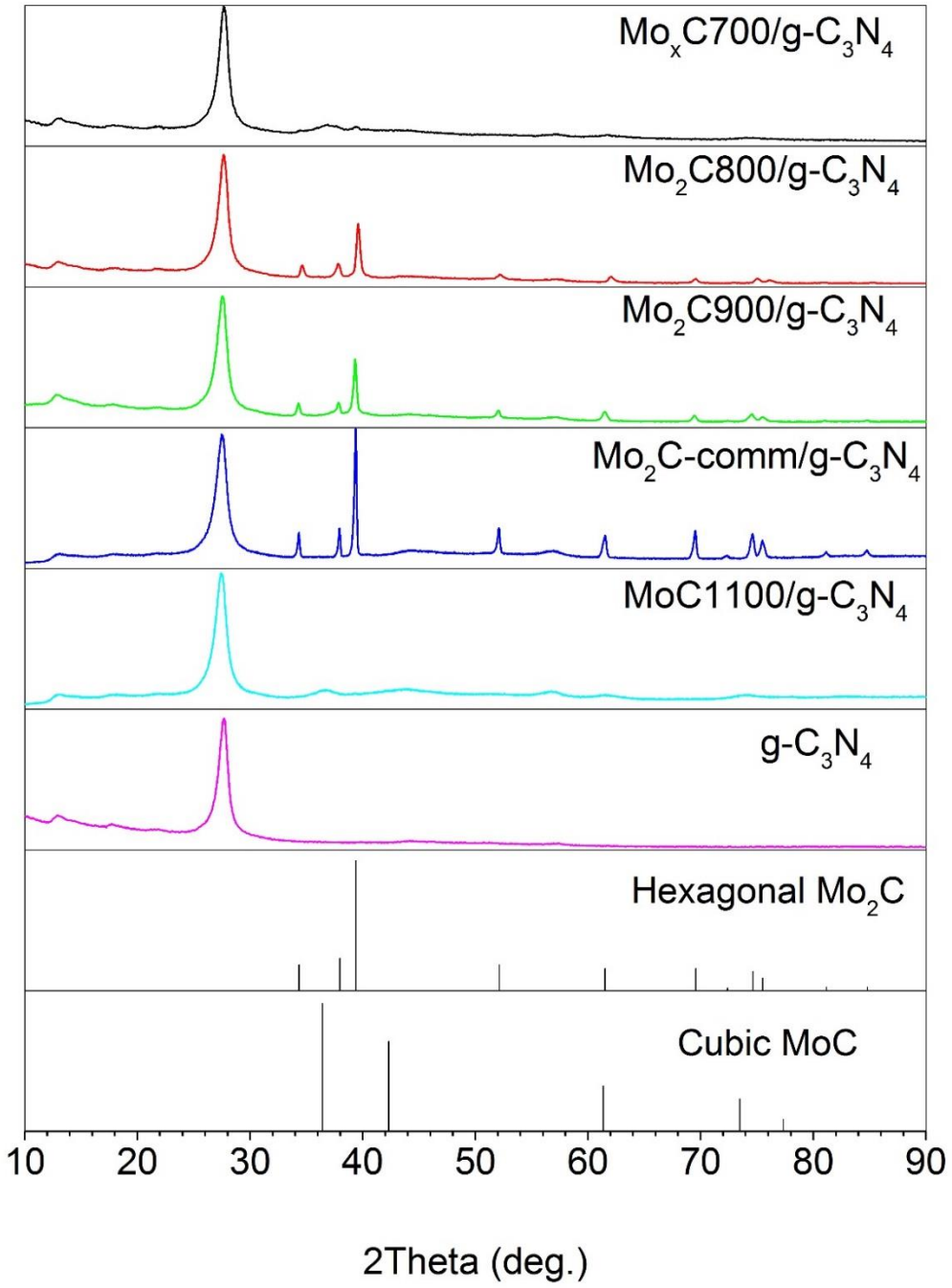

Figure 4.5. XRD patterns of $Mo_xCT/g\text{-}C_3N_4$, $Mo_2C\text{-comm}/g\text{-}C_3N_4$ and $g\text{-}C_3N_4$.

Table 4.1. Several characteristics of catalysts: Mo content, specific surface area, position of (002) XRD peak of g-C_3N_4, pore volume determined from N_2 adsorption-desorption isotherms, Mo_xC crystallite size determined from XRD patterns and bandgap.

Sample	Mo content (wt %)	S_{BET} (m^2/g)	(002) g-C_3N_4 (2θ deg.)	Pore volume (cm^3/g)	Crystallite size (nm)	Bandgap (eV)
$Mo_xC700/g\text{-}C_3N_4$	3.65	39	27.7	0.22	11 (Mo_2C) 4 (MoC)	2.79
$Mo_2C800/g\text{-}C_3N_4$	3.43	34	27.7	0.20	23 (Mo_2C)	2.79
$Mo_2C900/g\text{-}C_3N_4$	3.35	39	27.6	0.20	31 (Mo_2C)	2.78
$MoC1100/g\text{-}C_3N_4$	2.62	22	27.5	0.14	4 (MoC)	2.77
$Mo_2C\text{-}comm/g\text{-}C_3N_4$	3.33	22	27.5	0.15	37 (Mo_2C)	2.77
g-C_3N_4	--	31	27.7	0.21	--	2.75

The crystallite sizes of Mo_xCT in $Mo_xCT/g\text{-}C_3N_4$ were calculated using the Scherrer equation and the most intense peak for hexagonal Mo_2C and cubic MoC, the (101) at 39.39° and the (111) at 36.42°, respectively.

For $Mo_xC700/g\text{-}C_3N_4$, which contains both hexagonal Mo_2C and cubic MoC, using the accurate area intensities and the reference intensity ratios in the corresponding powder diffraction file, a semiquantitative phase analysis was carried out from the full profile analysis shown in Figure 4.6 [8]. The presence of about 14% and 86% of hexagonal Mo_2C and cubic MoC, respectively was determined.

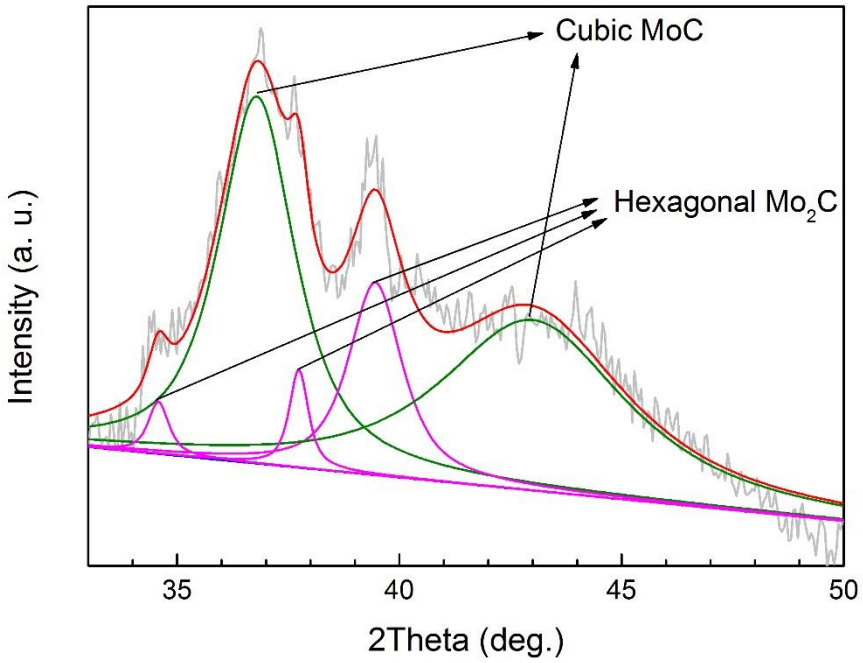

Figure 4.6. Full profile analysis of XRD pattern of $Mo_xC700/g\text{-}C_3N_4$.

Results of crystallite sizes for $Mo_xCT/g\text{-}C_3N_4$ (T=700-900 °C) (Table 4.1) indicate that the Mo_2C crystallite size increases with the rise of the treatment temperature used in the preparation of Mo_xCT; $Mo_xCT/g\text{-}C_3N_4$ (T=700-900 °C) had hexagonal Mo_2C crystallites with sizes in the range 11-31 nm. The biggest Mo_2C crystallite size was found for $Mo_2C\text{-comm}/g\text{-}C_3N_4$ (37 nm). Moreover, the crystallite size of MoC identified in $Mo_xC700/g\text{-}C_3N_4$ and $MoC1100/g\text{-}C_3N_4$ was similar (4 nm).

Figure 4.7 shows FTIR spectra of $Mo_xCT/g\text{-}C_3N_4$ and $Mo_2C\text{-comm}/g\text{-}C_3N_4$ composites. All the characteristic peaks of $g\text{-}C_3N_4$ are kept in the spectra of composited samples. XRD and FTIR results indicate that the structure of $g\text{-}C_3N_4$ is well kept after the deposition of Mo_xCT nanoparticles using the ultrasonic method proposed in this work.

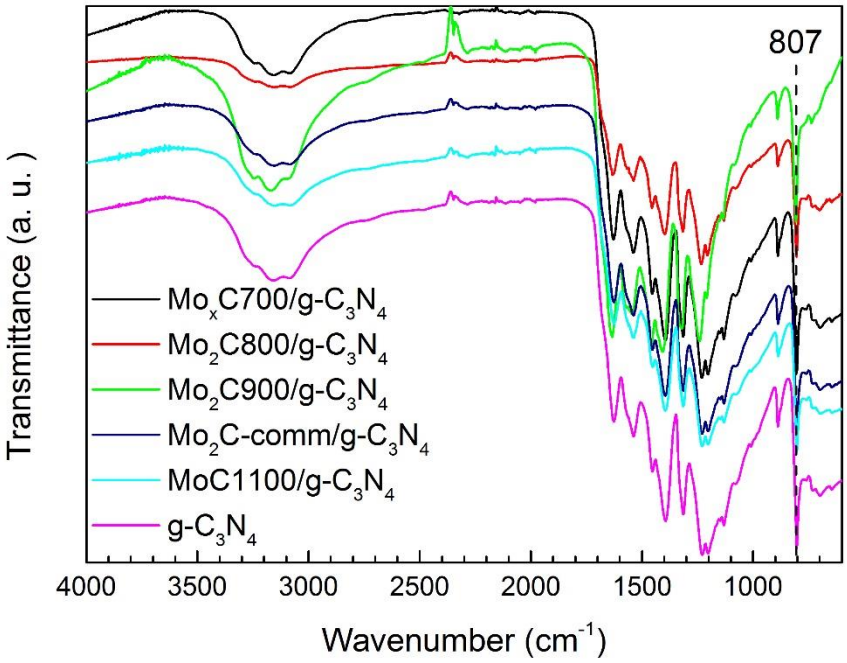

Figure 4.7. FTIR spectra of $Mo_xCT/g\text{-}C_3N_4$, $Mo_2C\text{-comm}/g\text{-}C_3N_4$ and $g\text{-}C_3N_4$.

Figure 4.8 presents N_2 adsorption-desorption isotherms for all materials studied. In all cases, type-IV isotherms with H3 hysteresis loops were found [9]. For all samples, a wide pore size distribution was determined (meso and macropores), as is shown in Figure 4.9, BET surface areas in the range of 22-39 m^2/g and pore volume values of 0.14-0.22 cm^3/g were obtained (Table 4.1).

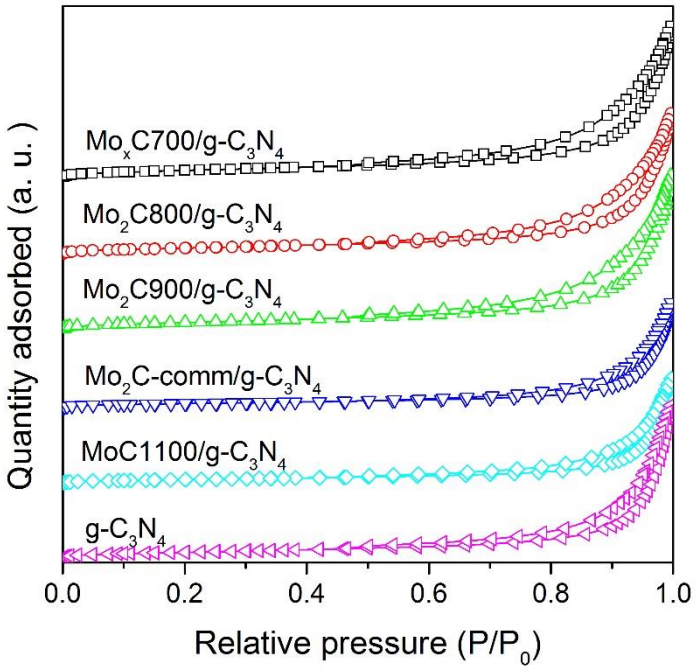

Figure 4.8. N_2 adsorption-desorption isotherms of $Mo_xCT/g\text{-}C_3N_4$, $Mo_2C\text{-}comm/g\text{-}C_3N_4$ and $g\text{-}C_3N_4$.

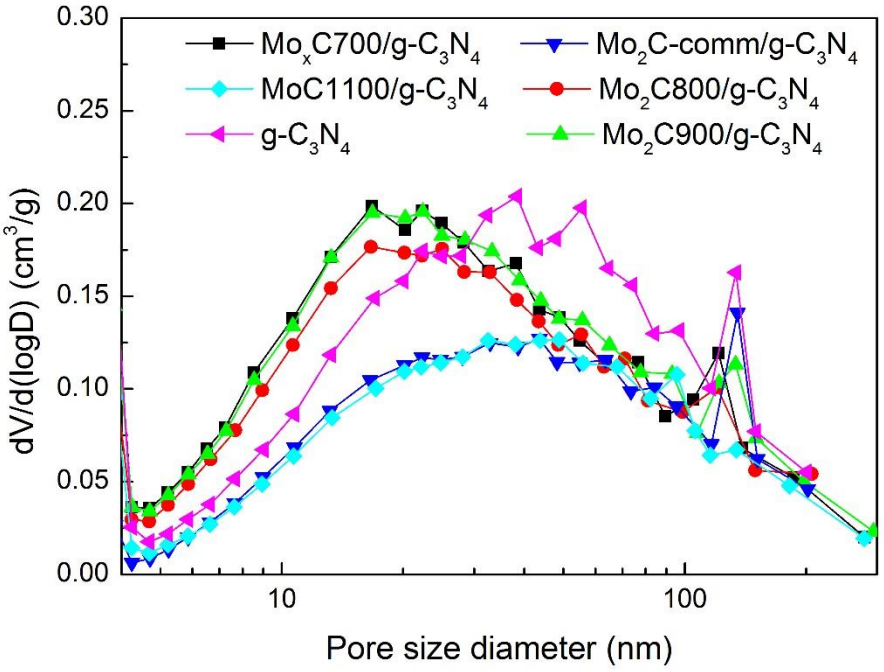

Figure 4.9. BJH pore size distribution plots of $Mo_xCT/g\text{-}C_3N_4$, $Mo_2C\text{-}comm/g\text{-}C_3N_4$ and $g\text{-}C_3N_4$.

Photocatalysts were analyzed by TEM for a more complete characterization. Figure 4.10 shows TEM, HRTEM images and EDX mapping of $Mo_xC700/g\text{-}C_3N_4$. In Figure 4.10A, small particles of Mo_xC onto $g\text{-}C_3N_4$ can be clearly observed. The Mo_xC particle size distribution in $Mo_xC700/g\text{-}C_3N_4$ show two domains with mean size of 4.3 and 13.0 nm (Figure 4.10B). The HRTEM analysis of Mo_xC700 particles allowed to identify different planes of hexagonal Mo_2C and cubic MoC phases (Figure 4.10C). Moreover, in $Mo_xC700/g\text{-}C_3N_4$ both hexagonal Mo_2C and cubic MoC in close contact were evidenced. The lattice fringes corresponding to the interplanar distances of 0.23 nm and 0.25 nm could be ascribed to the (101) crystal planes of hexagonal Mo_2C and the (111) crystal planes of cubic MoC, respectively [10]. These results accord with the XRD results exposed above. STEM image and EDX elemental mapping are shown in Figure 4.10D, a homogeneous distribution of Mo along the catalyst can be deduced.

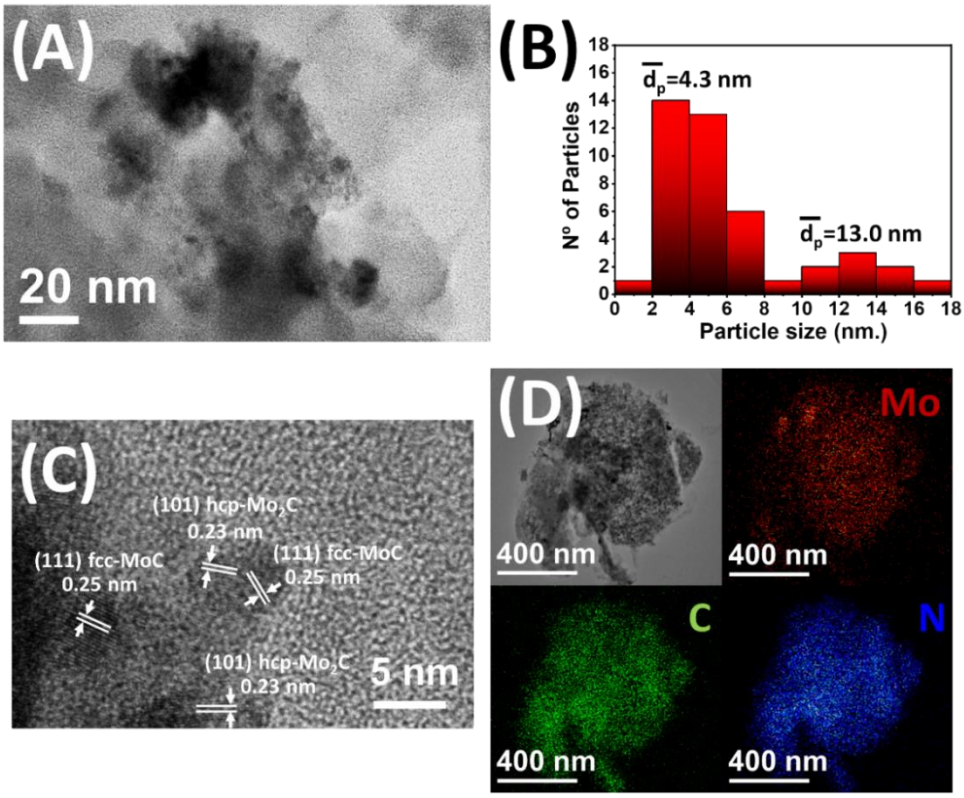

Figure 4.10. TEM, HRTEM and EDX elemental mapping of $Mo_xC700/g\text{-}C_3N_4$. **A)** TEM image; **B)** particle size distribution; **C)** HRTEM and **D)** STEM image and EDX mapping.

HRTEM micrographs and particle size distribution of $Mo_2C800/g\text{-}C_3N_4$, $Mo_2C900/g\text{-}C_3N_4$ and $MoC1100/g\text{-}C_3N_4$ are shown in Figure 4.11. Hexagonal Mo_2C nanoparticles can be identified in $Mo_2C800/g\text{-}C_3N_4$ and $Mo_2C900/g\text{-}C_3N_4$. On the other hand, only cubic MoC nanoparticles were observed in $MoC1100/g\text{-}C_3N_4$, which well agrees with XRD results. Moreover, it is easy to observe that the mean crystallite size of Mo_2C nanoparticles in $Mo_2C800/g\text{-}C_3N_4$ (24.1 nm) is smaller than in $Mo_2C900/g\text{-}C_3N_4$ (30.2 nm). MoC nanoparticles in $MoC1100/g\text{-}C_3N_4$ show a mean crystallite size of 5.1 nm, which is similar to that of cubic MoC in $Mo_xC700/g\text{-}C_3N_4$ and is in good agreement with XRD results.

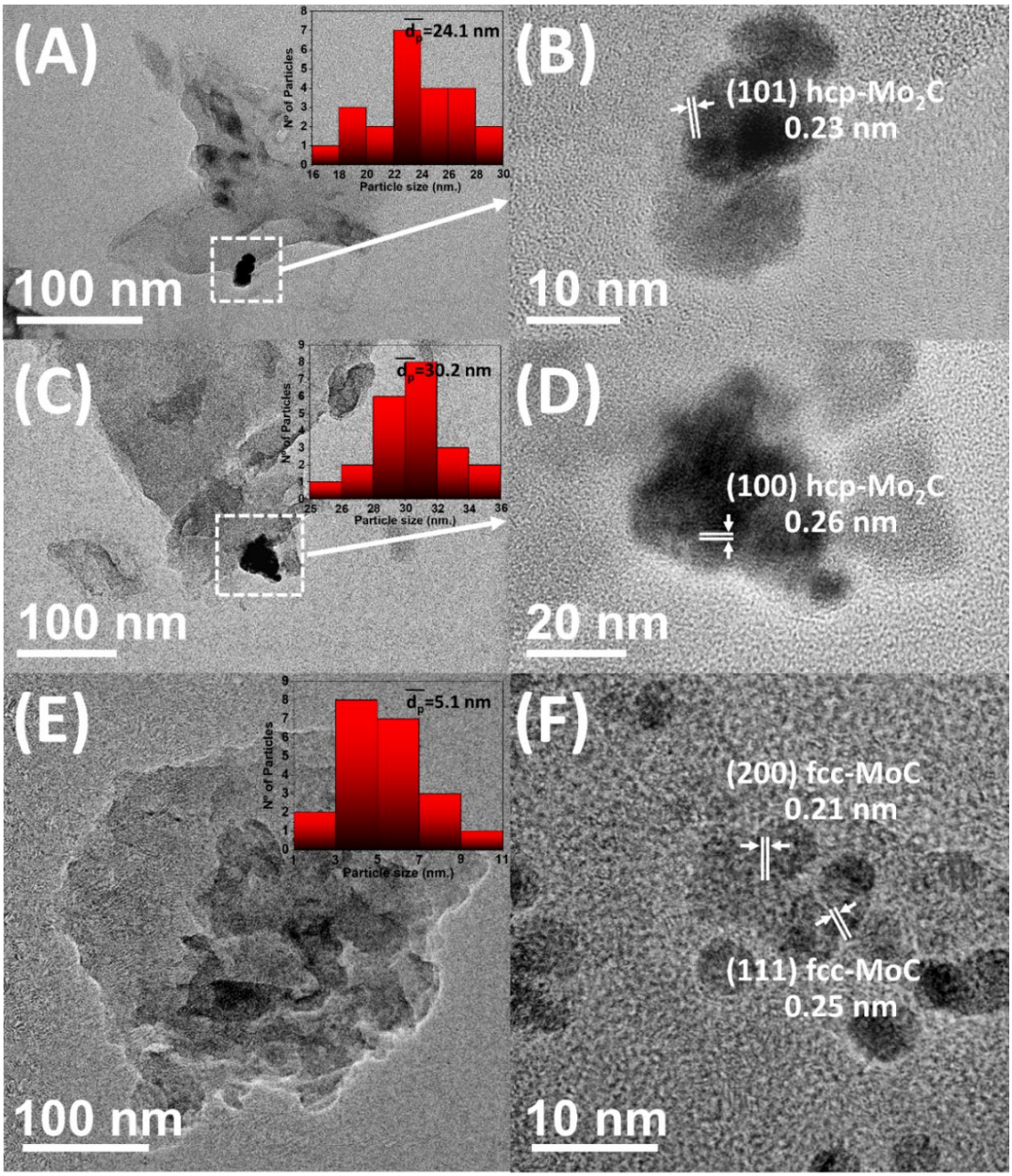

Figure 4.11. TEM and HRTEM images and particle size distribution of $Mo_2C800/g\text{-}C_3N_4$ (**A** and **B**); $Mo_2C900/g\text{-}C_3N_4$ (**C** and **D**); $MoC1100/g\text{-}C_3N_4$ (**E** and **F**) photocatalysts.

XPS survey spectra are shown in Figure 4.12. They confirm the presence of Mo, C, N and O in the as-prepared $Mo_xCT/g\text{-}C_3N_4$ samples.

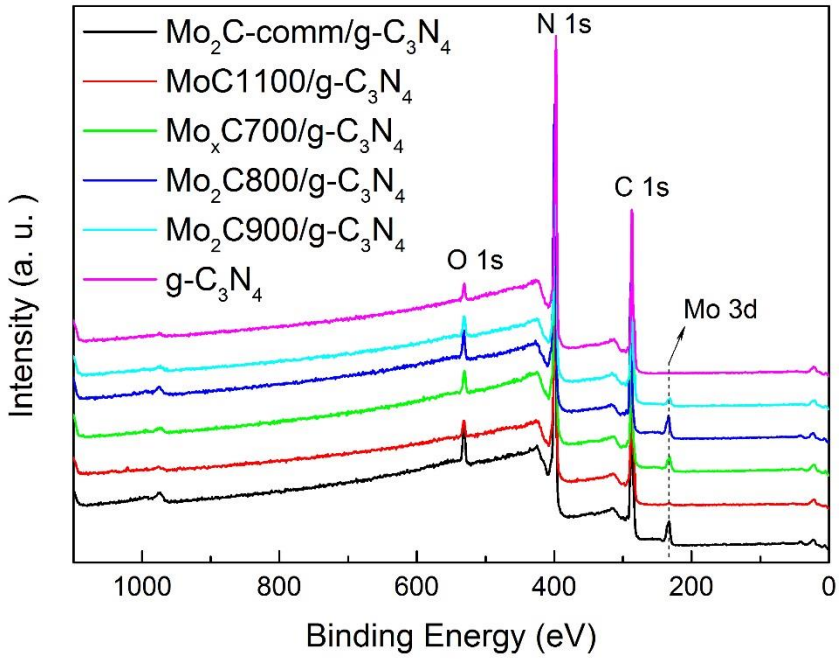

Figure 4.12. XPS survey spectra of $Mo_xCT/g\text{-}C_3N_4$, $Mo_2C\text{-comm}/g\text{-}C_3N_4$ and $g\text{-}C_3N_4$.

The high-resolution C 1s spectra of all samples are displayed in Figure 4.13. C 1s spectrum of $g\text{-}C_3N_4$ shows a main band at 288.1 eV, which is attributed to N-C=N of heterocycles in $g\text{-}C_3N_4$. The peak at 284.8 eV is associated with C-C bonds and the peak with low intensity at 286.0-287.5 eV to C-O bonds [11]. Besides bonds associated to the above-mentioned species, all C 1s spectra of Mo_xC-containing samples showed a small component at lower BE (283.4-283.8 eV) characteristic of carbides [12-14].

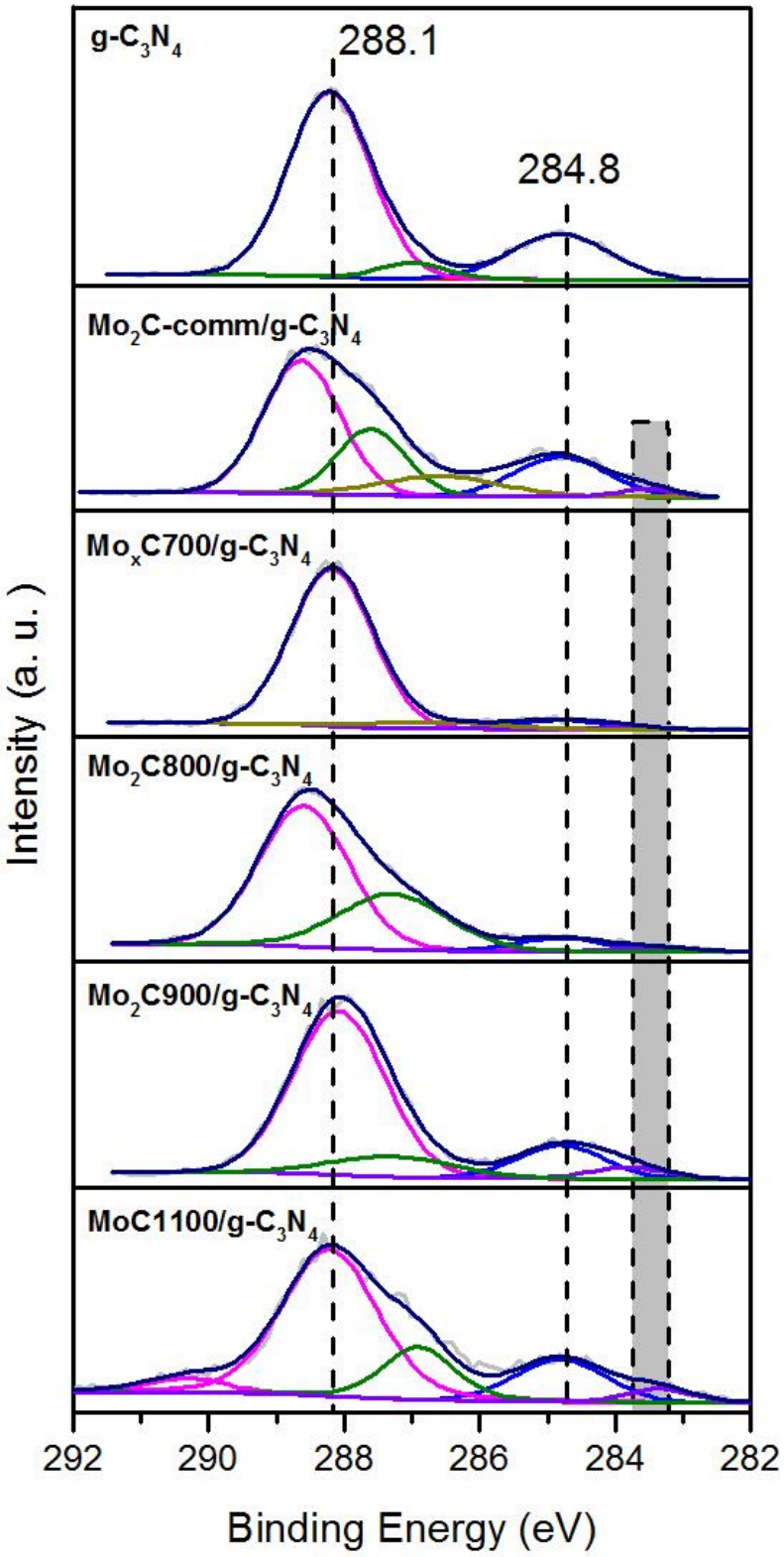

Figure 4.13. C 1s core-level spectra of $Mo_xCT/g\text{-}C_3N_4$, $Mo_2C\text{-comm}/g\text{-}C_3N_4$ and $g\text{-}C_3N_4$.

The N 1s spectrum of g-C_3N_4 (Figure 4.14) can be deconvoluted into four components. The main component at 398.7 eV is assigned to sp^2-bonded N (N-C=N) in heterocycles. The component at 399.4 eV is characteristic of tertiary nitrogen (N-$(C)_3$). Moreover, the component at 401.0 eV is related with the presence of amino-functional groups (C-N-H) from the defective condensation of heptazine substructures. The peak at 404.4 eV with very low intensity is related with charging effects or positive charge localization in the heterocycles. [11,15,16]. N 1s components characteristic of g-C_3N_4 were also found in the N 1s spectra of all Mo_xC-containing catalysts.

In all samples, the presence of surface oxygen could be evidenced by XPS (Figure 4.15). O 1s spectrum of g-C_3N_4 shows a broad peak with maximum of 532.6 eV, which could be related with the presence of adsorbed H_2O and carbon-bonded species [2]. The O 1s peaks of $Mo_xCT/g\text{-}C_3N_4$ and Mo_2C-comm/g-C_3N_4 samples are slightly shifted to lower BE, which could be assigned to the presence of O^{2-} bonded to Mo^{n+} in oxide and/or oxycarbide species [13].

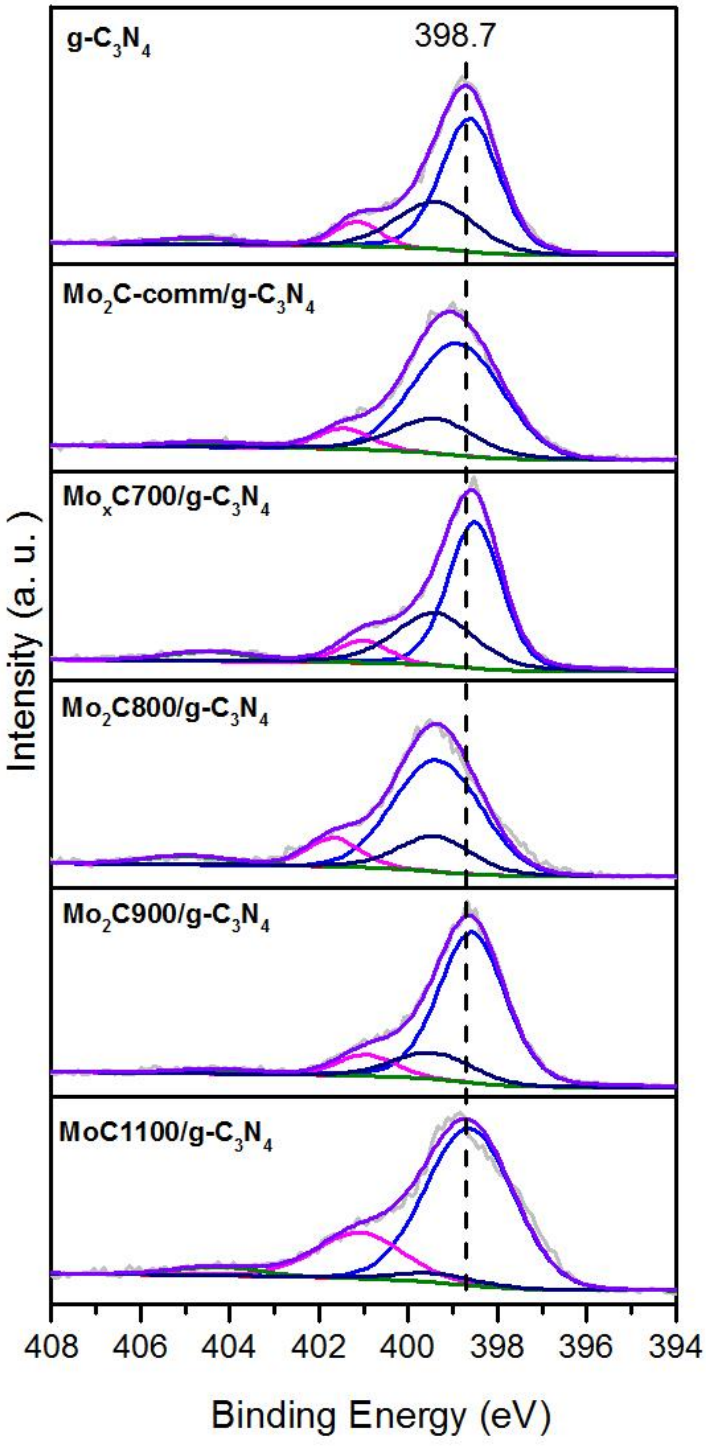

Figure 4.14. N 1s core-level spectra of $Mo_xCT/g\text{-}C_3N_4$, $Mo_2C\text{-comm}/g\text{-}C_3N_4$ and $g\text{-}C_3N_4$.

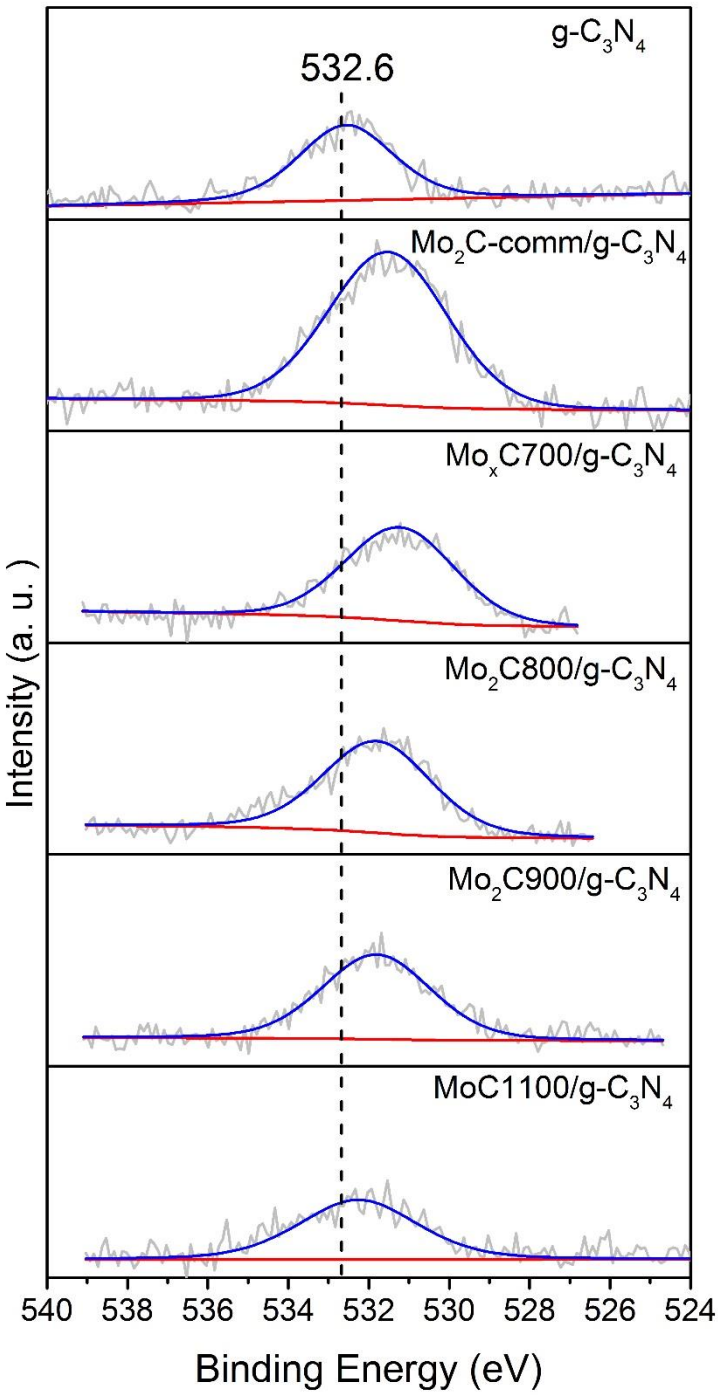

Figure 4.15. O 1s core-level spectra of $Mo_xCT/g\text{-}C_3N_4$, $Mo_2C\text{-comm}/g\text{-}C_3N_4$ and $g\text{-}C_3N_4$

Mo 3d core-level spectra of $Mo_xCT/g\text{-}C_3N_4$ and $Mo_2C\text{-}comm/g\text{-}C_3N_4$ samples are shown in Figure 4.16. Mo 3d spectra were deconvoluted into Mo $3d_{5/2}$/Mo $3d_{3/2}$ doublets setting a Mo $3d_{5/2}$/Mo $3d_{3/2}$ intensity ratio of 1.5 and an orbital splitting of 3.1 eV [17]. For $Mo_xCT/g\text{-}C_3N_4$ (T=700-900), the presence of Mo $3d_{5/2}$/Mo $3d_{3/2}$ doublets at 228.4-228.7/231.5-231.8 eV in $Mo_xCT/g\text{-}C_3N_4$ are indicative of the presence of surface carbides, Mo^{2+} and Mo^{3+} in Mo_2C and/or oxycarbide species. [18,19] Other doublets at higher binding energy are assigned to the presence of Mo^{4+}, Mo^{5+}, and Mo^{6+}, which suggests the presence of MoC and/or different oxycarbide and oxide species; surface oxycarbides and/or oxide species could be formed when samples were exposed to the air [20]. The poor Mo 3d spectrum of $MoC1100/g\text{-}C_3N_4$ did not allow a proper deconvolution of the different components. However, the presence of surface molybdenum carbide and oxide species could be also proposed in this sample.

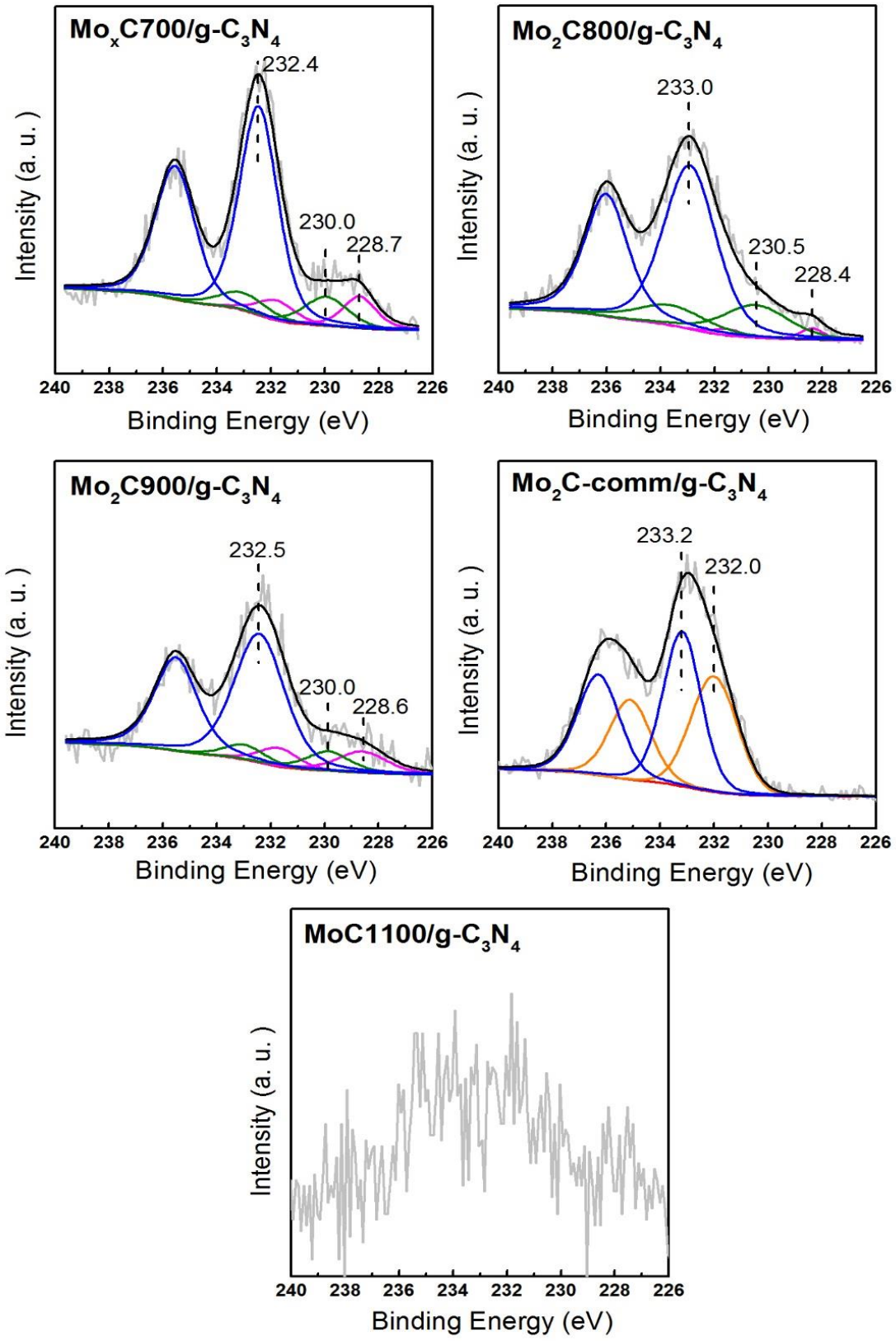

Figure 4.16. Mo 3d core-level spectra of $Mo_xCT/g\text{-}C_3N_4$ and $Mo_2C\text{-comm/g-}C_3N_4$.

Figure 4.17 displays the UV-vis DRS results of $Mo_xCT/g\text{-}C_3N_4$, $Mo_2C\text{-}comm/g\text{-}C_3N_4$ and $g\text{-}C_3N_4$. In all cases, the absorption edge is in the visible zone. Figure 4.18 shows the Tauc plots of the Kubelka-Munk function versus photonic energy (hu) used for the determination of bandgap values (Table 4.1, p. 121) [21]. The bandgap value determined for $g\text{-}C_3N_4$ is 2.75 eV, which is only slightly lower than those of $Mo_xCT/g\text{-}C_3N_4$ samples (2.77-2.79 eV).

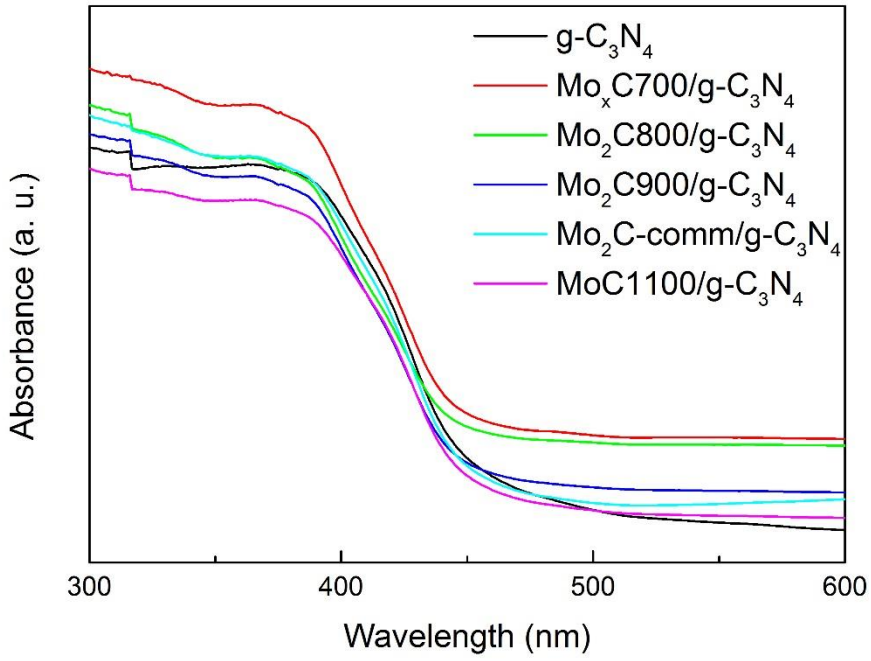

Figure 4.17. UV–vis diffuse reflectance spectra of $Mo_xCT/g\text{-}C_3N_4$, $Mo_2C\text{-}comm/g\text{-}C_3N_4$ and $g\text{-}C_3N_4$.

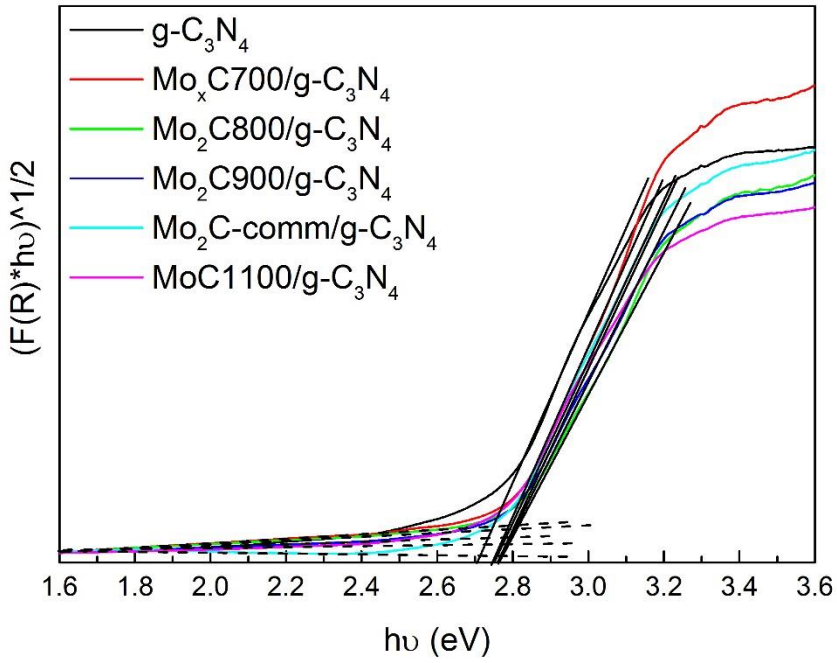

Figure 4.18. Tauc plots of the Kubelka-Munk function versus photonic energy (hυ) of $Mo_xCT/g\text{-}C_3N_4$, $Mo_2C\text{-comm}/g\text{-}C_3N_4$ and $g\text{-}C_3N_4$.

The recombination process of h^+/e^- pairs was studied by PL spectroscopy. Figure 4.19 shows PL spectra of $Mo_xCT/g\text{-}C_3N_4$, $Mo_2C\text{-comm}/g\text{-}C_3N_4$ and $g\text{-}C_3N_4$. In all cases, an emission peak in the visible zone (maximum at 455-465 nm) is shown, being the emission band of Mo_xC containing samples slightly blue-shifted with respect of $g\text{-}C_3N_4$. As can be observed, the intensity of the emission peaks of $Mo_xCT/g\text{-}C_3N_4$ is lower than that of the bare $g\text{-}C_3N_4$. The presence of Mo_xC on $g\text{-}C_3N_4$ decreases the rate of h^+/e^- recombination. The intensity of PL band follows the order: $g\text{-}C_3N_4$>$MoC1100/g\text{-}C_3N_4$>$Mo_2C\text{-comm}/g\text{-}C_3N_4$>$Mo_2C900/g\text{-}C_3N_4$>$Mo_2C800/g\text{-}C_3N_4$>$Mo_xC700/g\text{-}C_3N_4$, which indicates that the hexagonal Mo_2C in $Mo_xCT/g\text{-}C_3N_4$ is more effective in lowering the charge recombination than MoC in $MoC1100/g\text{-}C_3N_4$. Moreover, a smaller Mo_2C crystallite size and a close contact between hexagonal Mo_2C and

cubic MoC in $Mo_xCT/g\text{-}C_3N_4$ favor the decrease of the charge recombination rate.

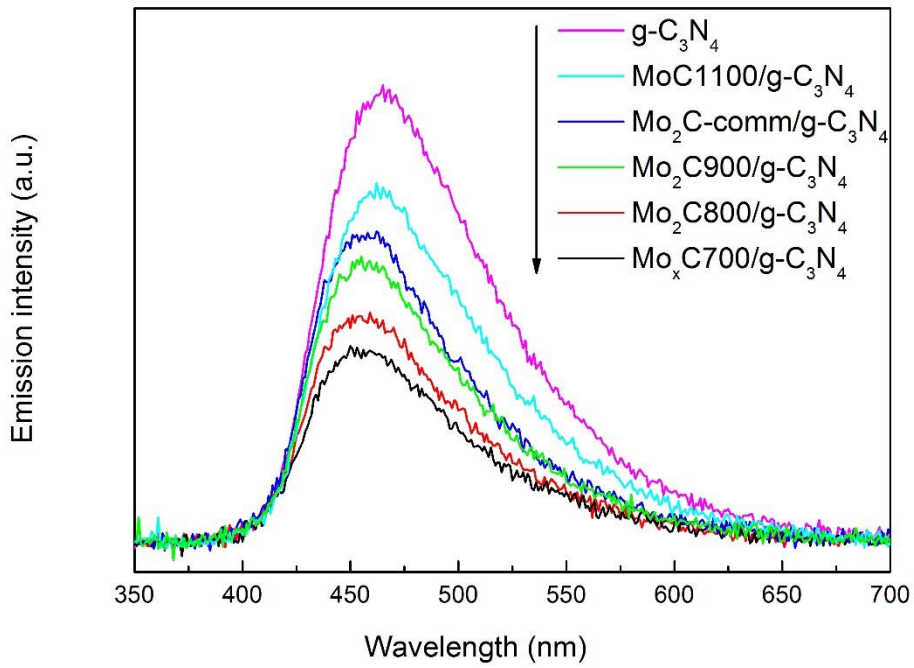

Figure 4.19. PL spectra of $Mo_xCT/g\text{-}C_3N_4$, $Mo_2C\text{-comm/g-}C_3N_4$ and $g\text{-}C_3N_4$.

Photoelectrochemical properties of samples were further evaluated by EIS and transient photocurrent response measurements.

The EIS Nyquist plots of $Mo_xCT/g\text{-}C_3N_4$, $Mo_2C\text{-comm/g-}C_3N_4$ and $g\text{-}C_3N_4$ are shown in Figures 4.20 and 4.21 in dark and under simulated solar irradiation, respectively. For all the catalysts, a smaller arc radius under simulated solar illumination than in dark conditions can be observed. Results for $Mo_xC700/g\text{-}C_3N_4$ and $g\text{-}C_3N_4$, with the smallest and the biggest arc radius, respectively, are illustrated as an example in Figure 4.22. The radiation used decreases the barrier of the electron transfer in all materials.

Moreover, all the $Mo_xCT/g\text{-}C_3N_4$ materials show a smaller arc radius than $g\text{-}C_3N_4$, which demonstrates that the presence of Mo_xCT onto $g\text{-}C_3N_4$ nanosheets decreases the resistance of electron transfer. The Nyquist arc radius follows the order: $g\text{-}C_3N_4$>$MoC1100/g\text{-}C_3N_4$>$Mo_2C\text{-comm}/g\text{-}C_3N_4$>$Mo_2C900/g\text{-}C_3N_4$>$Mo_2C800/g\text{-}C_3N_4$>$Mo_xC700/g\text{-}C_3N_4$. This order is similar to that of the intensity values of PL spectra. A lower barrier for the electron transfer could be related with a more efficient charge separation.

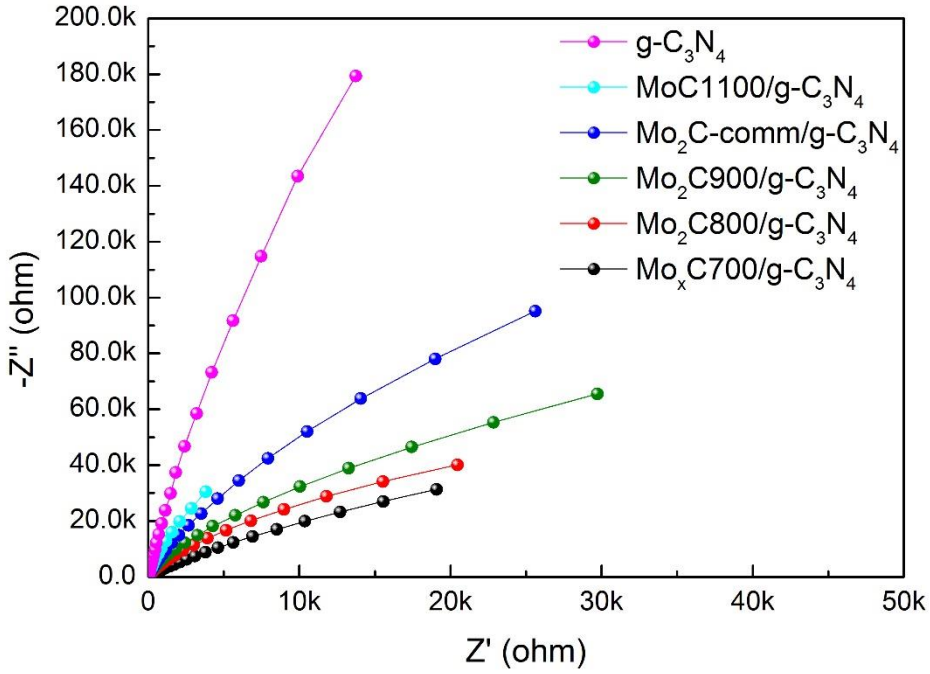

Figure 4.20. EIS Nyquist plots of $Mo_xCT/g\text{-}C_3N_4$, $Mo_2C\text{-comm}/g\text{-}C_3N_4$ and $g\text{-}C_3N_4$ samples in dark.

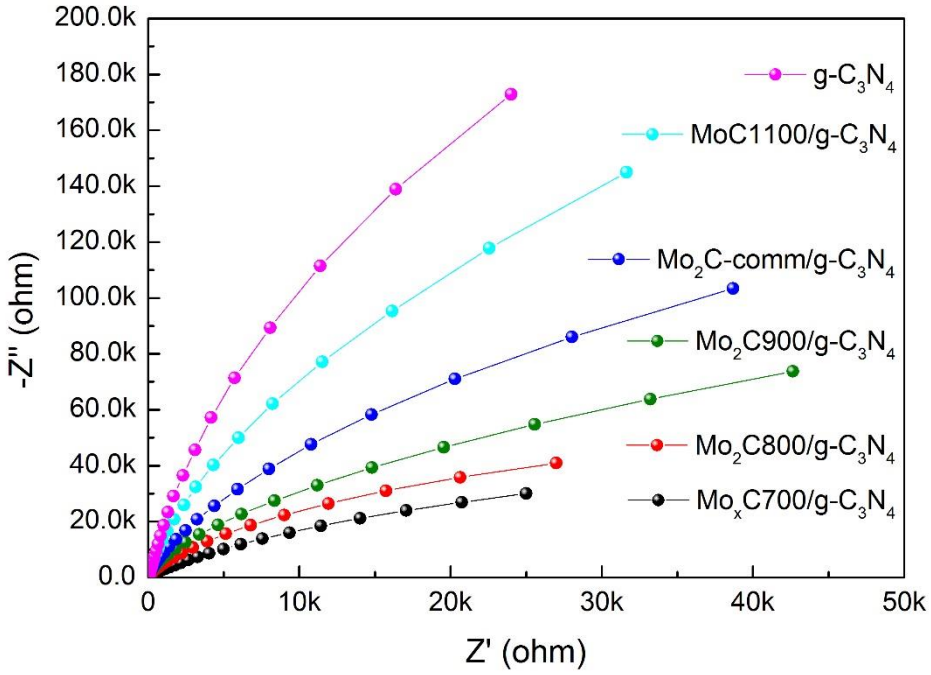

Figure 4.21. EIS Nyquist plots of $Mo_xCT/g\text{-}C_3N_4$, $Mo_2C\text{-comm}/g\text{-}C_3N_4$ and $g\text{-}C_3N_4$ samples under simulated solar irradiation.

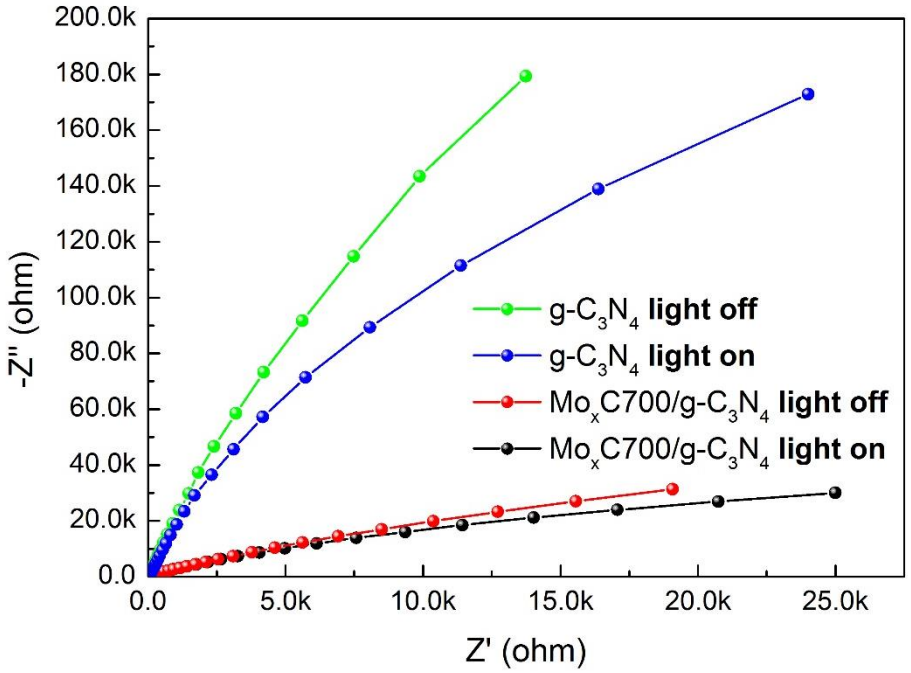

Figure 4.22. EIS Nyquist plots of samples $Mo_xC700/g\text{-}C_3N_4$ and $g\text{-}C_3N_4$ in dark and under simulated solar irradiation.

The transient photocurrent responses were determined and are shown in Figure 4.23. $Mo_xCT/g\text{-}C_3N_4$ photocatalysts show higher photocurrent density than $g\text{-}C_3N_4$, following the order: $g\text{-}C_3N_4$<$MoC1100/g\text{-}C_3N_4$<$Mo_2C\text{-comm}/g\text{-}C_3N_4$<$Mo_2C900/g\text{-}C_3N_4$≈$Mo_2C800/g\text{-}C_3N_4$<$Mo_xC700/g\text{-}C_3N_4$. $Mo_xC700/g\text{-}C_3N_4$, which showed the lowest electron/hole recombination rate and the lowest barrier for the electron transfer, shows the highest photocurrent density under illumination.

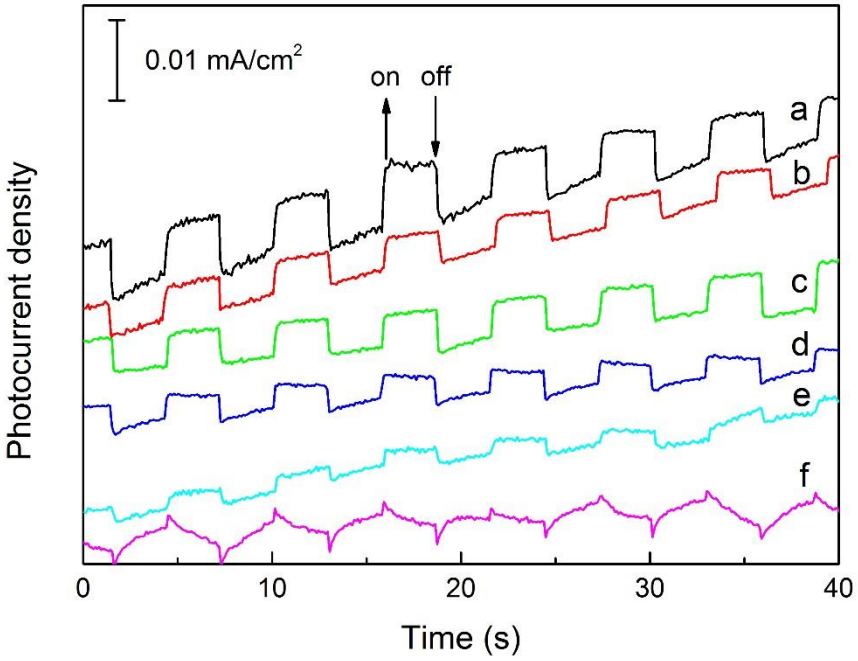

Figure 4.23. Transient photocurrent responses of photocatalysts **a**) $Mo_xC700/g\text{-}C_3N_4$; **b**) $Mo_2C800/g\text{-}C_3N_4$; **c**) $Mo_2C900/g\text{-}C_3N_4$; **d**) $Mo_2C\text{-comm}/g\text{-}C_3N_4$; **e**) $MoC1100/g\text{-}C_3N_4$; **f**) $g\text{-}C_3N_4$.

4.3 Photocatalytic H_2 production over $Mo_xCT/g\text{-}C_3N_4$

The photocatalytic behaviour of all the catalysts in the H_2 production from $ethanol_{(aq)}$ solution (25 % v/v, 250 mL) was determined under visible light irradiation (λ>385 nm). In all cases, 300 mg of photocatalysts were dispersed

into the ethanol$_{(aq)}$ solution. A photocatalytic test using pristine g-C_3N_4 and a blank test without photocatalyst were carried out using similar experimental conditions. Figure 4.24 shows the total amount of H_2 produced per gram of catalyst along time, during 4 h test.

As shown in Figure 4.24, a negligible amount of H_2 was produced when g-C_3N_4 was used as the photocatalyst or when a test without catalyst was carried out. Mo_xC700/g-C_3N_4 was the most active photocatalyst (1019 μmol H_2•g_{cat}^{-1}), being the H_2 yield over Mo_2C-comm/g-C_3N_4 and MoC1100/g-C_3N_4 much lower than that over Mo_xCT/g-C_3N_4 catalysts. The amount of H_2 produced followed the order: Mo_xC700/g-C_3N_4>Mo_2C800/g-C_3N_4>Mo_2C900/g-C_3N_4> Mo_2C-comm/g-C_3N_4>MoC1100/g-C_3N_4>g-C_3N_4.

A similar order was determined when the amount of H_2 produced was referred to gram of Mo (Figure 4.25).

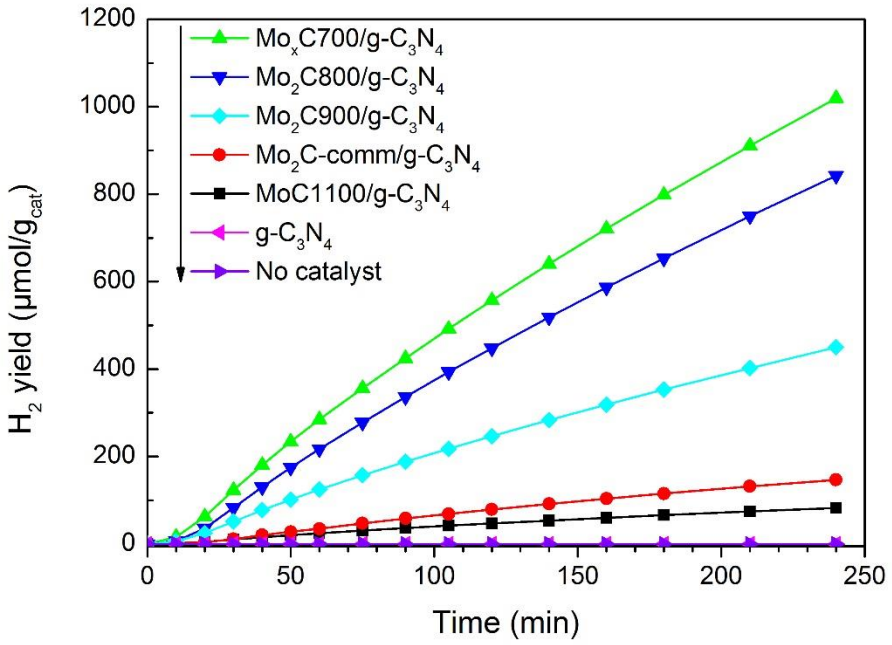

Figure 4.24. Total H_2 yield per gram of catalyst produced from ethanol$_{(aq)}$ 25% v/v over Mo_xCT/g-C_3N_4, Mo_2C-comm/g-C_3N_4, g-C_3N_4 and in the blank test. t= 4 h, T= 20 °C, visible irradiation.

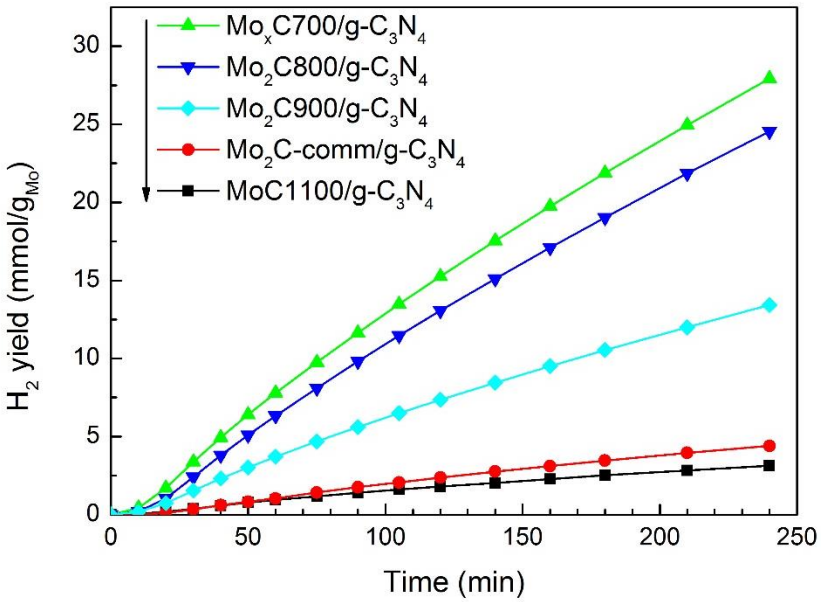

Figure 4.25. Total H_2 yield per gram of Mo produced from ethanol$_{(aq)}$ 25% v/v over $Mo_xCT/g\text{-}C_3N_4$, $Mo_2C\text{-comm}/g\text{-}C_3N_4$, $g\text{-}C_3N_4$ and in the blank test. t= 4 h, T= 20 °C, visible irradiation.

Figure 4.26 shows the corresponding AQE values. Ass expected, $Mo_xC700/g\text{-}C_3N_4$ photocatalyst showed the highest AQE, 0.2 %.

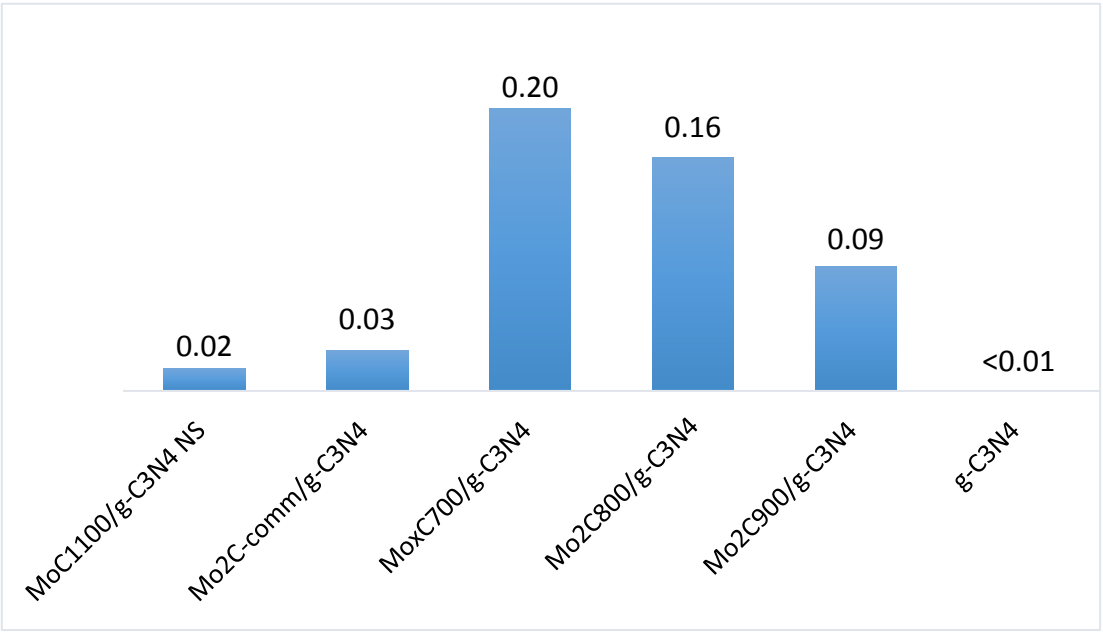

Figure 4.26. AQE (%) for photocatalytic H_2 production from ethanol$_{(aq)}$ 25% v/v over $Mo_xCT/g\text{-}C_3N_4$, $Mo_2C\text{-comm}/g\text{-}C_3N_4$ and $g\text{-}C_3N_4$.

Besides H_2, only 2,3-butanediol and CO_2 were found as carbon-containing products. As stated in Chapter 3, 2,3-butanediol can be formed by the coupling of two α-hydroxyethyl radicals ($\cdot CH(OH)CH_3$) [22-24].

The photocatalytic performance of $Mo_xCT/g\text{-}C_3N_4$ can be related with their physicochemical and photoelectrochemical characteristics. A lower recombination rate of the photogenerated charges, a lower barrier for the electron transport and a higher photocurrent response favor the photocatalytic H_2 production. Moreover, the characteristics of Mo_xC co-catalyst determined the above-mentioned properties. The presence of hexagonal Mo_2C in $Mo_xCT/g\text{-}C_3N_4$ leads to more performant photocatalysts than the presence of cubic MoC. Additionally, materials with smaller hexagonal hcp nanoparticles show a better photocatalytic behaviour. Finally, we propose that the presence of hexagonal Mo_2C and cubic MoC in the $Mo_xC700/g\text{-}C_3N_4$ greatly influences its characteristics and therefore its photocatalytic behaviour. As stated above, $Mo_xC700/g\text{-}C_3N_4$ showed the lowest rate of charge recombination, the highest photocurrent response, the lowest electron transfer resistance and the highest photocatalytic performance.

4.4 References

1. Liu X, Pajares A, Matienzo D J D C, et al. Preparation and characterization of bulk Mo_xC catalysts and their use in the reverse water-gas shift reaction. Catalysis Today, 2020, 356: 384-389.

2. She X, Wu J, Zhong J, et al. Oxygenated monolayer carbon nitride for excellent photocatalytic hydrogen evolution and external quantum efficiency. Nano Energy, 2016, 27: 138-146.

3. Wang X, Blechert S, Antonietti M. Polymeric graphitic carbon nitride for

heterogeneous photocatalysis. ACS Catalysis, 2012, 2: 1596-1606.

4. Niu P, Zhang L, Liu G, et al. Graphene‐like carbon nitride nanosheets for improved photocatalytic activities. Advanced Functional Materials, 2012, 22: 4763-4770.

5. Chen Z, Xia K, She X, et al. 1D metallic MoO_2-C as co-catalyst on 2D g-C_3N_4 semiconductor to promote photocatlaytic hydrogen production. Applied Surface Science, 2018, 447: 732-739.

6. Yan S C, Li Z S, Zou Z G. Photodegradation performance of g-C_3N_4 fabricated by directly heating melamine. Langmuir, 2009, 25: 10397-10401.

7. Cao S, Yu J. g-C_3N_4-based photocatalysts for hydrogen generation. The Journal of Physical Chemistry Letters, 2014, 5: 2101-2107.

8. Snyder R L. The use of reference intensity ratios in X-ray quantitative analysis. Powder Diffraction, 1992, 7: 186-193.

9. Thommes M, Kaneko K, Neimark A V, et al. Physisorption of gases, with special reference to the evaluation of surface area and pore size distribution (IUPAC Technical Report). Pure and Applied Chemistry, 2015, 87: 1051-1069.

10. Gates-Rector S, Blanton T. The powder diffraction file: a quality materials characterization database. Powder Diffraction, 2019, 34: 352-360.

11. Gu Q, Liao Y, Yin L, et al. Template-free synthesis of porous graphitic carbon nitride microspheres for enhanced photocatalytic hydrogen generation with high stability. Applied Catalysis B: Environmental, 2015, 165: 503-510.

12. Porosoff M D, Yang X, Boscoboinik J A, et al. Molybdenum carbide as alternative catalysts to precious metals for highly selective reduction of CO_2 to CO. Angewandte Chemie International Edition, 2014, 53: 6705-6709.

13. Liu X, Kunkel C, Ramirez de la Piscina P, et al. Effective and highly selective CO generation from CO_2 using a polycrystalline α-Mo_2C catalyst. ACS Catalysis, 2017, 7: 4323-4335.

14. Ma R, Zhou Y, Chen Y, et al. Ultrafine molybdenum carbide nanoparticles composited with carbon as a highly active hydrogen-evolution electrocatalyst. Angewandte Chemie International Edition, 2015, 127: 14936-14940.

15. Jiang Y, Sun Z, Tang C, et al. Enhancement of photocatalytic hydrogen evolution activity of porous oxygen doped g-C_3N_4 with nitrogen defects induced by changing electron transition. Applied Catalysis B: Environmental, 2019, 240: 30-38.

16. Long B, Lin J, Wang X. Thermally-induced desulfurization and conversion of guanidine thiocyanate into graphitic carbon nitride catalysts for hydrogen photosynthesis. Journal of Materials Chemistry A, 2014, 2: 2942-2951.

17. Oshikawa K, Nagai M, Omi S. Characterization of molybdenum carbides for methane reforming by TPR, XRD, and XPS. The Journal of Physical Chemistry B, 2001, 105: 9124-9131.

18. Porosoff M D, Yang X, Boscoboinik J A, et al. Molybdenum carbide as alternative catalysts to precious metals for highly selective reduction of CO_2 to CO. Angewandte Chemie International Edition, 2014, 53: 6705-6709.

19. Gao Q, Zhao X, Xiao Y, et al. A mild route to mesoporous Mo_2C–C hybrid nanospheres for high performance lithium-ion batteries. Nanoscale, 2014, 6: 6151-6157.

20. Sullivan M M, Held J T, Bhan A. Structure and site evolution of molybdenum carbide catalysts upon exposure to oxygen. Journal of Catalysis, 2015, 326:

82-91.

21. Makuła P, Pacia M, Macyk W. How to correctly determine the band gap energy of modified semiconductor photocatalysts based on UV–Vis spectra. The Journal of Physical Chemistry Letters, 2018, 9: 6814-6817.

22. Lu H, Zhao J, Li L, et al. Selective oxidation of sacrificial ethanol over TiO_2-based photocatalysts during water splitting. Energy & Environmental Science, 2011, 4: 3384-3388.

23. Sola A C, Ramírez de la Piscina P, Homs N. Behaviour of Pt/TiO_2 catalysts with different morphological and structural characteristics in the photocatalytic conversion of ethanol aqueous solutions. Catalysis Today, 2020, 341: 13-20.

24. Sola A C, Homs N, Ramírez de la Piscina P. Photocatalytic H_2 production from $ethanol_{(aq)}$ solutions: The effect of intermediate products. International Journal of Hydrogen Energy, 2016, 41: 19629-19636.

Chapter 5.

Photocatalytic H_2 production over materials with engineered Mo_xC/TiO_2 interfaces

In this chapter, we analyse the photocatalytic H_2 production over materials with engineered Mo_xC/TiO_2 interfaces. A study of the use of Mo_xC as co-catalyst in anatase TiO_2 nanoparticles with different shapes, TiO_2(NS)-X (X=F and 600) and TiO_2(bipy) with morphology of nanosheets and bipyramids, respectively is carried out.

Photocatalysts are analyzed using different techniques, such as N_2 adsorption/desorption isotherms, XRD, HRTEM, UV-vis DRS, XPS, PL spectroscopy and PEC measurements. The morphology and interface of the composited materials, determine their characteristics as photocatalysts in the photocatalytic hydrogen production from ethanol aqueous solutions under UV-visible irradiation.

The presence of Mo_xC onto anatase TiO_2 nanoparticles improves their photocatalytic behaviour. This effect is higher for TiO_2(bipy), which exposes mainly (101) facets. The efficiency of the systems is related with the characteristics of engineered Mo_xC-TiO_2 interfaces.

5.1 Preparation of Mo_xC/TiO_2 photocatalysts

5.1.1 TiO_2(NS)-X and TiO_2(bipy) used

We chose three different anatase TiO_2 samples with different shapes and surface properties to fabricate composited photocatalysts, namely TiO_2(NS)-X (X=F and 600) and TiO_2(bipy). TiO_2(NS)-F is constituted by nanosheets with dominant exposed (001) facets, which present adsorbed fluorides on the surface and in the bulk [1]. TiO_2(NS)-600 results from the calcination of TiO_2(NS)-F at 600 °C in the air to remove fluorides and shows similar morphology to TiO_2(NS)-F. TiO_2(bipy) presents a bipyramidal shape, mainly limited by (101) facets and does not contain fluorides [1]. The three anatase TiO_2 samples were synthesized by Dr. Lorenzo Mino (University of Torino) according to [1-4]; their characteristics will be discussed in the **5.2.1** section.

5.1.2 Mo_xC synthesis

Mo_xC was synthesized following the method used for the preparation of Mo_xC700 described in **4.1.1 section**. In brief, 5.6 mmol of $MoCl_5$ and 2.8 mmol of DI were added into 15 mL of ethanol under stirring and then ethanol was evaporated at 60 °C in the air to produce a gel. Afterward, the gel was treated in a tubular furnace under Ar flow up to 700 °C (2.5 °C·min^{-1}) for 5 h; then cooled down to room temperature under Ar flow.

5.1.3 Synthesis of Mo_xC/TiO_2(NS)-X and Mo_xC/TiO_2(bipy) photocatalysts

The process used for the preparation of Mo_xC/TiO_2(NS)-X and Mo_xC/TiO_2(bipy) photocatalysts is schematically illustrated in Figure 5.1. A certain amount of Mo_xC and TiO_2(NS)-X or TiO_2(bipy) were dispersed in ethanol and treated under ultrasounds (SONICS VCX 500) at 20 °C for 1 h and 250 W under Ar flow, then ethanol was carefully evaporated under continuous stirring at 70 °C keeping the Ar flow. Initially, three photocatalysts containing about 1%

wt Mo_xC were prepared, 1-Mo_xC/TiO_2(NS)-F 1-Mo_xC/TiO_2(NS)-600 and Mo_xC/TiO_2(bipy). Then, the study was extended using two more samples with about 0.5 % and 3.5% wt of Mo_xC onto TiO_2(bipy), 0.5-Mo_xC/TiO_2(bipy) and 3.5-Mo_xC/TiO_2(bipy), respectively.

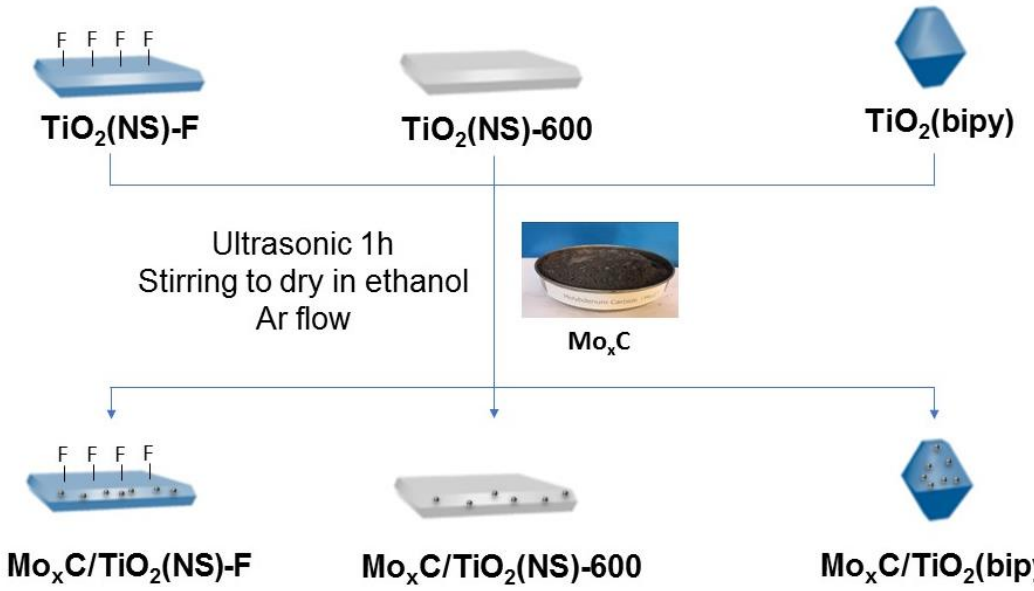

Figure 5.1. Synthesis procedure of Mo_xC/TiO_2(NS)-X and Mo_xC/TiO_2(bipy) photocatalysts.

5.2 Characteristics of 1-Mo_xC/TiO_2(NS)-X and 1-Mo_xC/TiO_2(bipy) photocatalysts

5.2.1 TiO_2(NS)-X and TiO_2(bipy) used

The crystalline structure of TiO_2(NS)-X and TiO_2(bipy) samples were characterized by powder XRD; the corresponding patterns are shown in Figure 5.2. Sharp diffraction peaks were displayed at 2θ of 25.28, 36.95, 37.80, 38.58, 48.05, 53.89, 55.06, 62.12, 62.69, 68.76, 70.31, 75.03 and 76.02° in all XRD

patterns, which fitted well with the standard diffraction pattern of anatase TiO_2 (JCPDS, 00-021-1272).

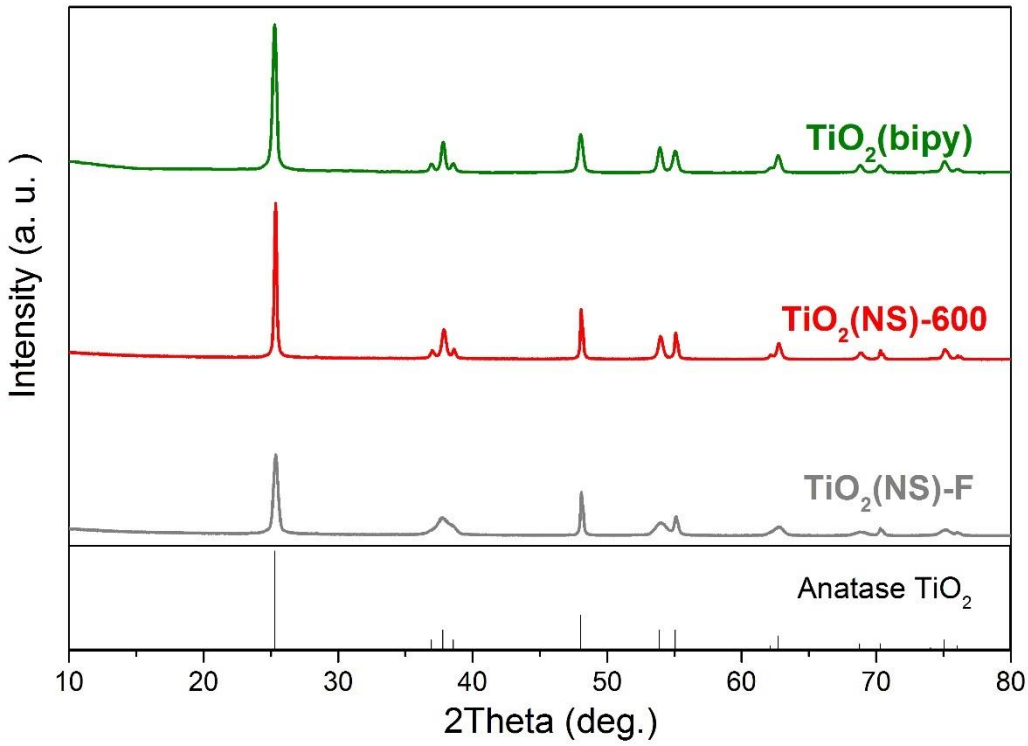

Figure 5.2. XRD patterns of TiO_2(NS)-X and TiO_2(bipy) samples.

The average crystallite dimensions of as-prepared TiO_2(NS)-X and TiO_2(bipy) samples were calculated by the Scherrer equation using the (004) and (200) peaks, the results are reported in Table 5.1. The crystallite dimensions of TiO_2(NS)-F (thickness 13 nm, width 54 nm) correspond to nanosheets. The use of fluorides in the preparation of TiO_2(NS)-F allowed tailoring the shape of TiO_2 nanoparticles and led to the synthesis of nanosheets as it had been previously demonstrated [1]. However, after the treatment at 600 °C, the thickness increased up to 31 nm, which suggests an aggregation of nanosheets along the c-axis in TiO_2(NS)-600 (Table 5.1). The thickness of TiO_2(bipy) is slightly higher than its width (Table 5.1), which is expected for truncated bipyramidal nanoparticles.

Table 5.1. Several characteristics of anatase TiO_2 nanoparticles: average dimension of crystallite domains obtained by Scherrer analysis of the (004) and (200) XRD peaks, BET surface area and bandgap energy.

Sample	d_{004} (nm)	d_{200} (nm)	S_{BET} (m^2/g)	Bandgap (eV)
TiO_2(NS)-F	13	54	36	3.27
TiO_2(NS)-600	31	53	20	3.25
TiO_2(bipy)	40	31	27	3.10

Figure 5.3 shows representative SEM images of the TiO_2 samples used. As shown in Figure 5.3A, the TiO_2(NS)-F sample is composed of nanosheets, mainly exposing (001) facets [1]; TiO_2(NS)-600 sample still shows a nanosheet shape (Figure 5.3B) but higher thickness than TiO_2(NS)-F, due to the calcination treatment. Figure 5.3C displays the shape of TiO_2(bipy), which exhibits truncated bipyramidal shape mainly dominated by (101) facets [1]. The percentage of exposed (001) and (101) facets for TiO_2(NS)-F (80 % (001), 20 % (101)), TiO_2(NS)-600 (60 % (001), 40 % (101)) and TiO_2(bipy) (10 % (001), 90 % (101)) had been previously calculated [1].

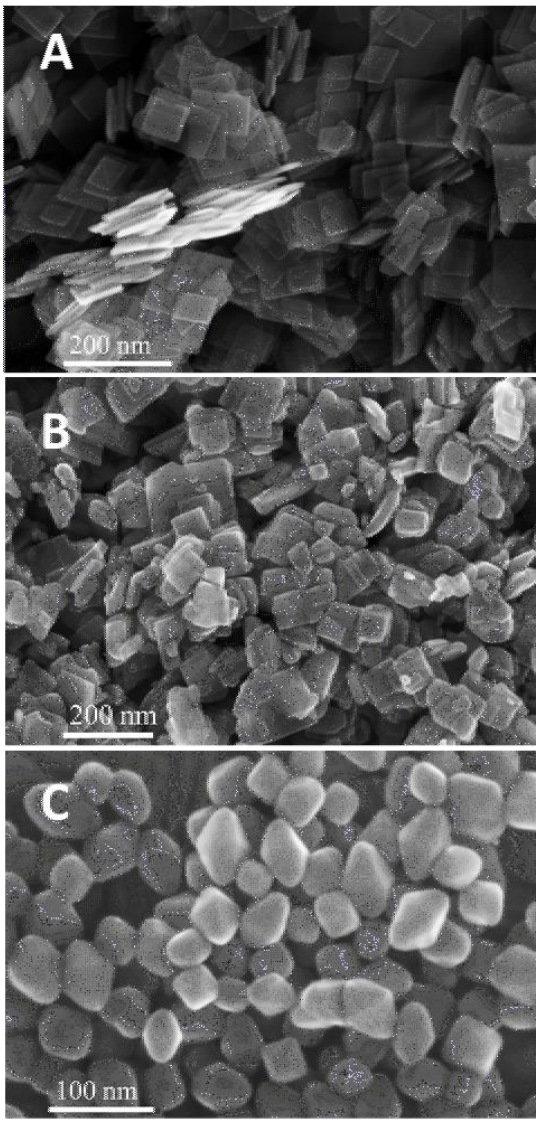

Figure 5.3. SEM images of (**A**) TiO_2(NS)-F, (**B**)TiO_2(NS)-600 and (**C**)TiO_2(bipy) samples.

UV-vis DR spectra of pristine TiO_2 samples are shown in Figure 5.4. The bandgap values were calculated from the Tauc plots (Figure 5.5) and are recorded in Table 5.1. TiO_2(NS)-X samples show a slightly higher bandgap (3.25-3.27 eV) than TiO_2(bipy) (3.10 eV), which agrees with previous studies [1]. This has been related with the presence of quantum confinement effects in TiO_2(NS)-X samples [1,5].

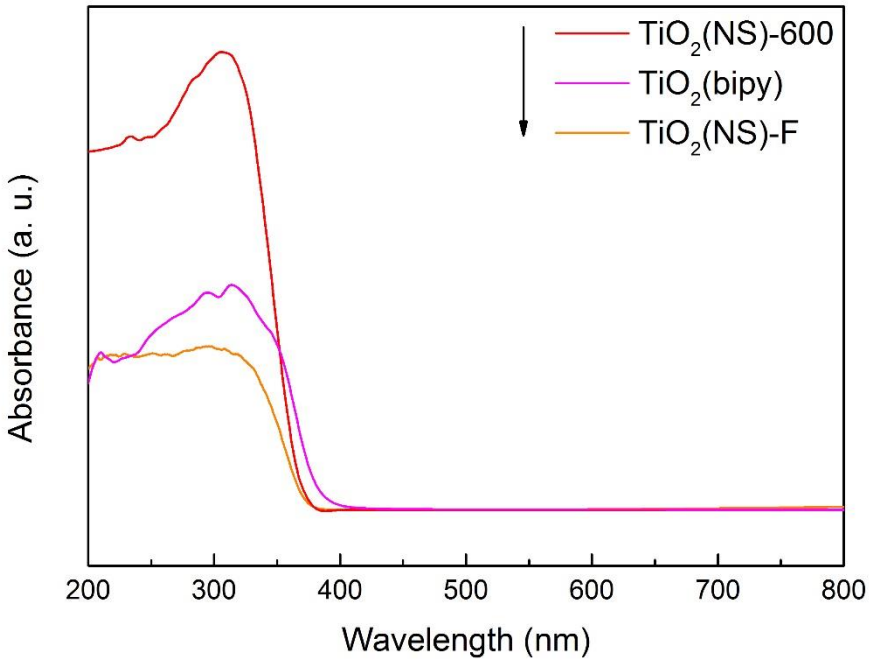

Figure 5.4. UV-vis diffuse reflectance spectra of TiO_2(NS)-X and TiO_2(bipy).

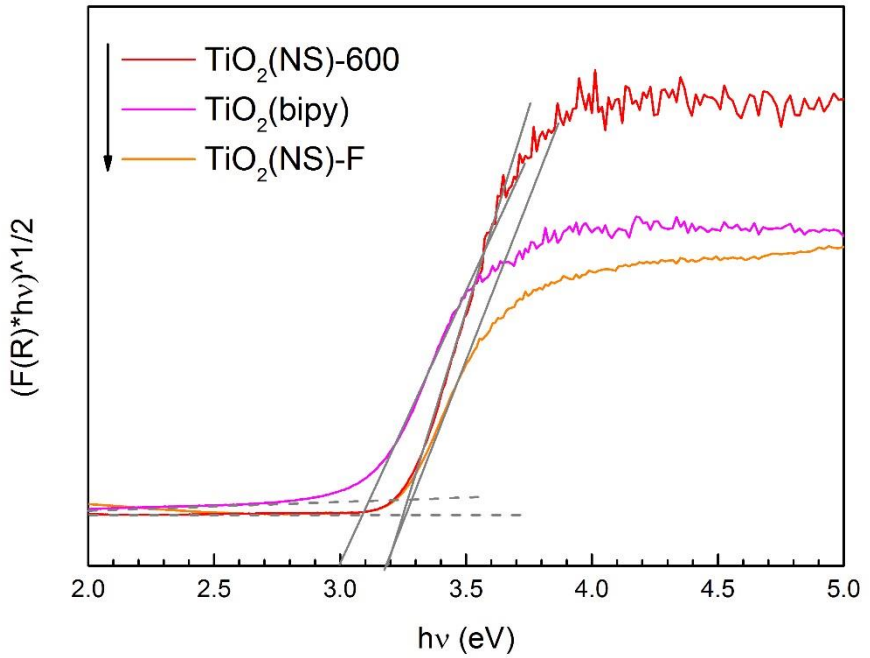

Figure 5.5. Tauc plots of the Kubelka-Munk function versus photonic energy of TiO_2(NS)-X and TiO_2(bipy).

The S_{BET} of as-made TiO_2(NS)-X and TiO_2(bipy) samples are shown in Table 5.1 (p. 154). TiO_2(NS)-F shows S_{BET} of 36 m^2/g, which is higher than that of TiO_2(NS)-600 (20 m^2/g). It could be due to the aggregation of TiO_2(NS)-600 nanosheets, as is proposed from XRD results. The S_{BET} of TiO_2(bipy) is in between those of TiO_2(NS)-F and TiO_2(NS)-600 samples.

5.2.2 Characteristics of Mo_xC

Mo_xC was characterized by XRD before its deposition onto TiO_2 (Figure 5.6). As expected, the presence of hexagonal Mo_2C and cubic MoC is evidenced. The semiquantitative analysis of the Mo_xC XRD patterns indicates the presence of about 86% and 14% of cubic MoC and hexagonal Mo_2C, respectively (Figure 5.7) [6]. An average crystallite size of 4 nm was determined for cubic MoC and of 11 nm for hexagonal Mo_2C.

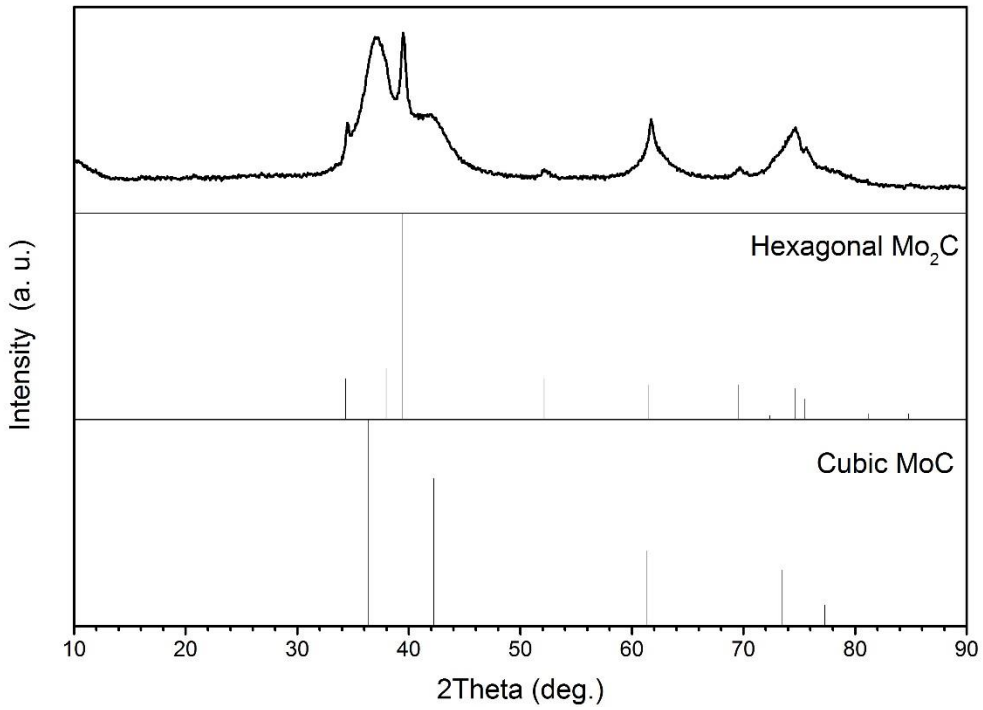

Figure 5.6. XRD pattern of Mo_xC nanoparticles.

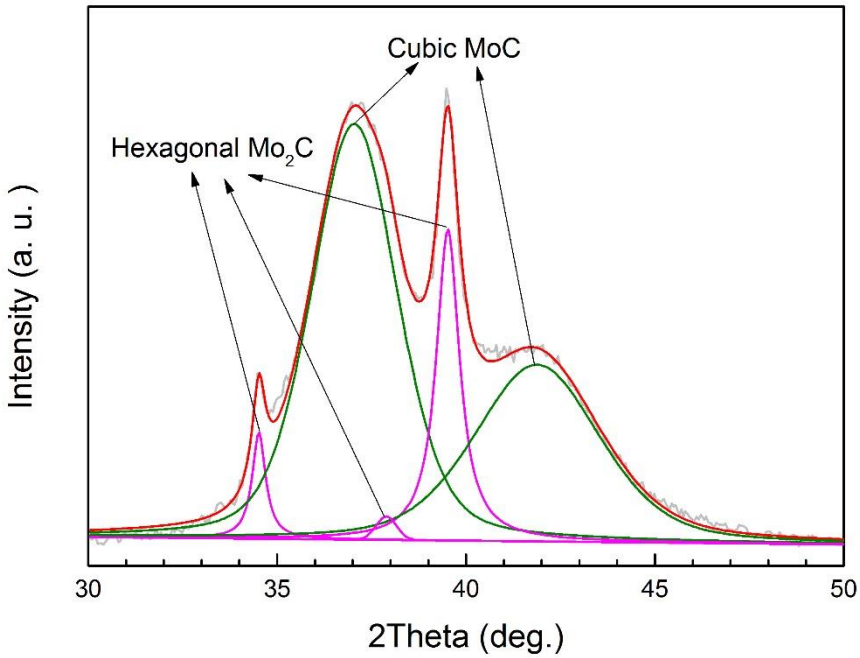

Figure 5.7. Full profile analysis of XRD pattern of Mo_xC nanoparticles.

5.2.3 1-Mo_xC/TiO_2(NS)-X and 1-Mo_xC/TiO_2(bipy) photocatalysts

1-Mo_xC/TiO_2(NS)-X and 1-Mo_xC/TiO_2(bipy) photocatalysts were characterized by XRD, TEM, BET, XPS and UV-vis DRS.

XRD patterns are shown in Figure 5.8; only diffraction peaks corresponding to anatase TiO_2 (No. JCPDS: 00-021-1272) can be determined in all materials. There were no observable diffraction peaks related with Mo_xC due to the relatively low content of Mo_xC (0.7-1% wt/wt) in the samples (Table 5.2).

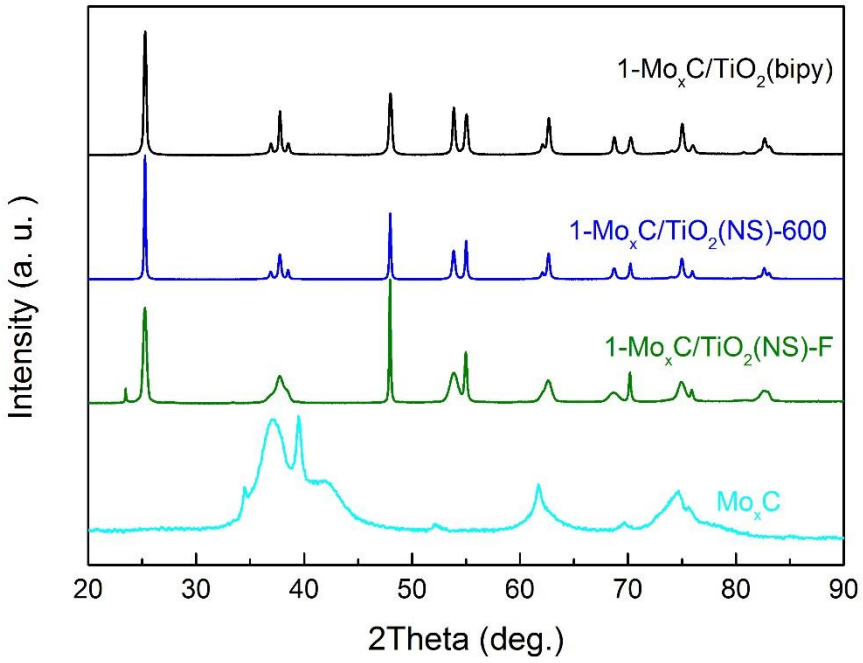

Figure 5.8. XRD diffraction patterns of 1-Mo_xC/TiO_2(NS)-X and 1-Mo_xC/TiO_2(bipy).

Table 5.2 also shows other characteristics of 1-Mo_xC/TiO_2(NS)-X and 1-Mo_xC/TiO_2(bipy) samples. Although after Mo_xC loading, the S_{BET} of all the samples decreased, the trend of S_{BET} is similar to that of TiO_2 used: 1-Mo_xC/TiO_2(NS)-F>1-Mo_xC/TiO_2(bipy)>1-Mo_xC/TiO_2(NS)-600.

On the other hand, the average crystallite dimensions of 1-Mo_xC/TiO_2(NS)-X and 1-Mo_xC/TiO_2(bipy) (Table 5.2) calculated from (004) and (200) XRD peaks are similar to those of TiO_2(NS)-X and TiO_2(bipy) (Table 5.1, p. 154).

Table 5.2. Average dimensions of crystal domains obtained by Scherrer analysis of the (004) and (200) XRD peaks, BET surface area, Mo content and bandgap of 1-Mo_xC/TiO_2(NS)-X and 1-Mo_xC/TiO_2(bipy).

Catalyst	d_{004} (nm)	d_{200} (nm)	S_{BET} (m^2/g)	Mo content (wt %)	Bandgap (eV)
1-Mo_xC/TiO_2(NS)-F	14	56	26	0.96	3.27
1-Mo_xC/TiO_2(NS)-600	30	53	9	0.73	3.26
1-Mo_xC/TiO_2(bipy)	36	29	15	0.69	2.92

1-Mo_xC/TiO_2(NS)-X and 1-Mo_xC/TiO_2(bipy) samples were analyzed by TEM and HRTEM (Figure 5.9). As can be seen in Figure 5.9, in all cases, the morphology of anatase TiO_2 nanoparticles was kept after Mo_xC deposition.

High-resolution TEM images shown in Figures 5.9B, D and F indicate that small Mo_xC particles were well dispersed on the surface of TiO_2. A similar Mo_xC particle size distribution was determined in all cases, according to the XRD results, which indicated the presence of hexagonal Mo_2C and cubic MoC with crystallite sizes of 4 nm and 11 nm, respectively. This particle size distribution is in turn similar to that of Mo_xC700/g-C_3N_4, which was similarly prepared but using g-C_3N_4 instead of TiO_2.

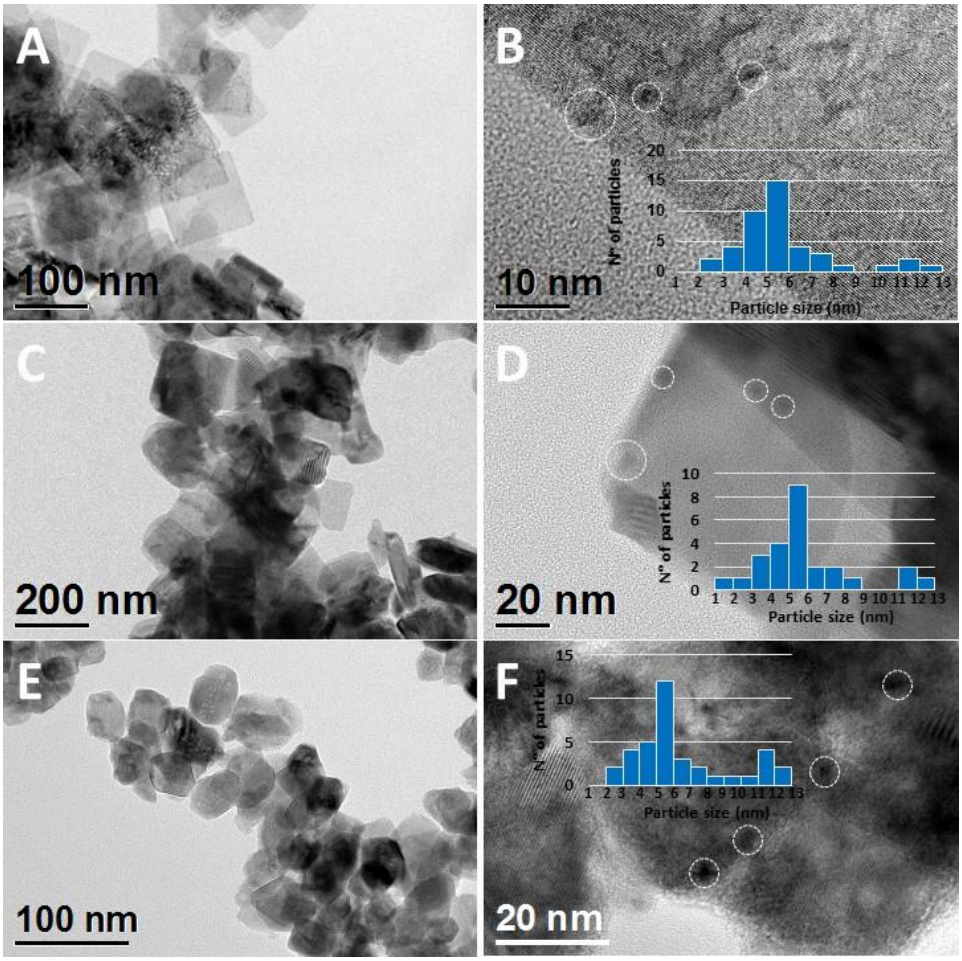

Figure 5.9. TEM and HRTEM images of 1-Mo_xC/TiO_2(NS)-F (**A** and **B**); 1-Mo_xC/TiO_2(NS)-600 (**C** and **D**) and 1-Mo_xC/TiO_2(bipy) (**E** and **F**) samples.

Figure 5.10 shows the XPS survey spectra of 1-Mo_xC/TiO_2(NS)-X and 1-Mo_xC/TiO_2(bipy) samples. In all cases, the presence of Mo (Mo 3p and 3d peaks), C (C 1s), Ti (Ti 2p) and O (O 1s) on the surface of the samples can be deduced. An intense peak corresponding to fluorides (F 1s) can be only observed for 1-Mo_xC/TiO_2(NS)-F.

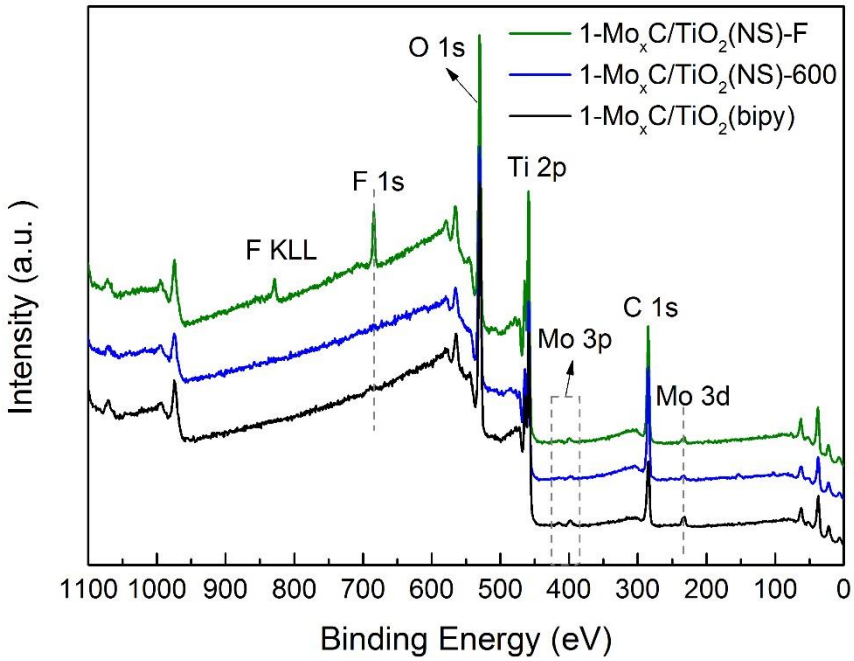

Figure 5.10. XPS survey spectra of 1-Mo_xC/TiO_2(NS)-X and 1-Mo_xC/TiO_2(bipy) samples.

The high-resolution C 1s spectra of 1-Mo_xC/TiO_2(NS)-X and 1-Mo_xC/TiO_2(bipy) samples are presented in Figure 5.11. In all cases, a central peak at 284.4 eV, which is attributed to C−C, is present. The C 1s peaks at 288.5 and 286.6-286.9 eV are related with the presence of O=C−O and C−O, respectively [7,8]. The C 1s spectrum of 1-Mo_xC/TiO_2(bipy) could be deconvoluted into 4 peaks. Besides the three peaks mentioned above, the peak at 283.0 eV can be assigned to Mo-C from molybdenum carbide and/or oxycarbide species [9-11].

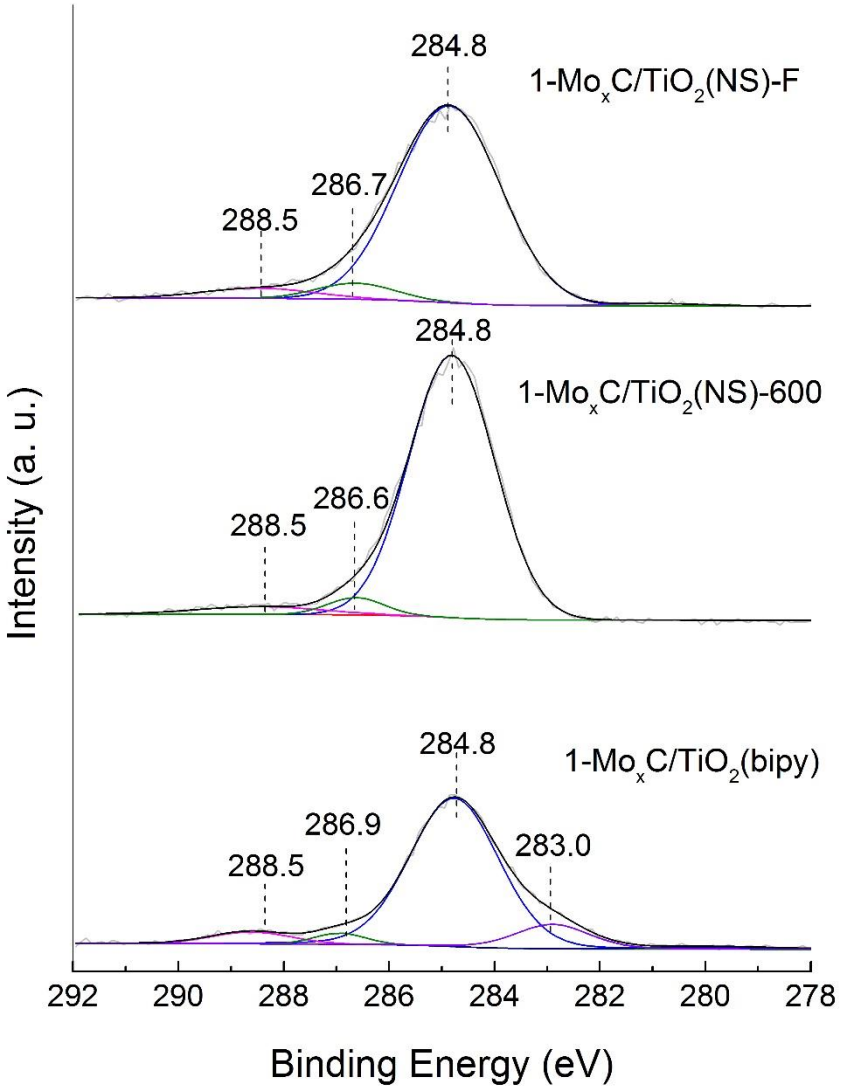

Figure 5.11. C 1s core-level spectra of 1-Mo_xC/TiO_2(NS)-X and 1-Mo_xC/TiO_2(bipy) samples.

Figure 5.12 shows Mo 3d core-level spectra of 1-Mo_xC/TiO_2(NS)-X and 1-Mo_xC/TiO_2(bipy) samples. In all cases, spectra are dominated by two main components at 232.0-231.7 eV and 235.1-234.9 eV, which are assigned to Mo^{5+} surface species, coming from the formation of Mo_xCO_y species after interaction with the metal oxide surface. The Mo $3d_{5/2}$ – Mo $3d_{3/2}$ doublet at 228.3–228.7 and 231.4–231.8 eV is assigned to the presence of Mo^{2+} and/or Mo^{3+}, which is

related with the presence of Mo_xC and/or oxycarbide species on the surface of the samples [12-14].

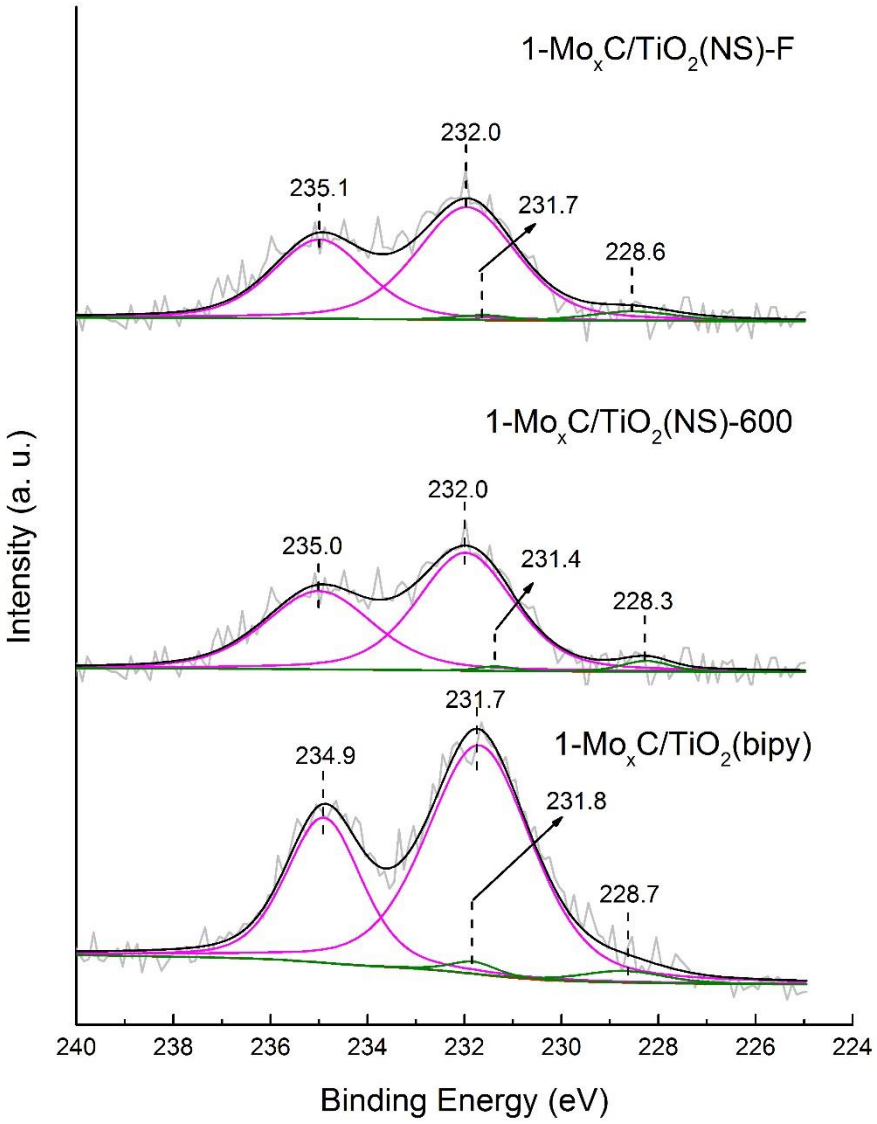

Figure 5.12. Mo 3d core-level spectra of 1-Mo_xC/TiO_2(NS)-X and 1-Mo_xC/TiO_2(bipy) samples.

Figure 5.13 shows Ti 2p spectra of 1-Mo_xC/TiO_2(NS)-X and 1-Mo_xC/TiO_2(bipy) samples. For 1-Mo_xC/TiO_2(NS)-F and 1-Mo_xC/TiO_2(NS)-600 samples, Ti $2p_{3/2}$ peaks at 459.0 eV characteristic of Ti^{4+} species can be

observed. The Ti 2p peaks corresponding to 1-Mo_xC/TiO_2(bipy) are clearly asymmetric and can be deconvoluted into two components. The Ti $2p_{1/2}$ – Ti $2p_{3/2}$ doublet peaks at 463.2 and 457.5 are characteristic of Ti^{3+} species [15,16], which could be related with the interfacial interaction between Mo_xC and TiO_2(bipy) with dominant (101) facets.

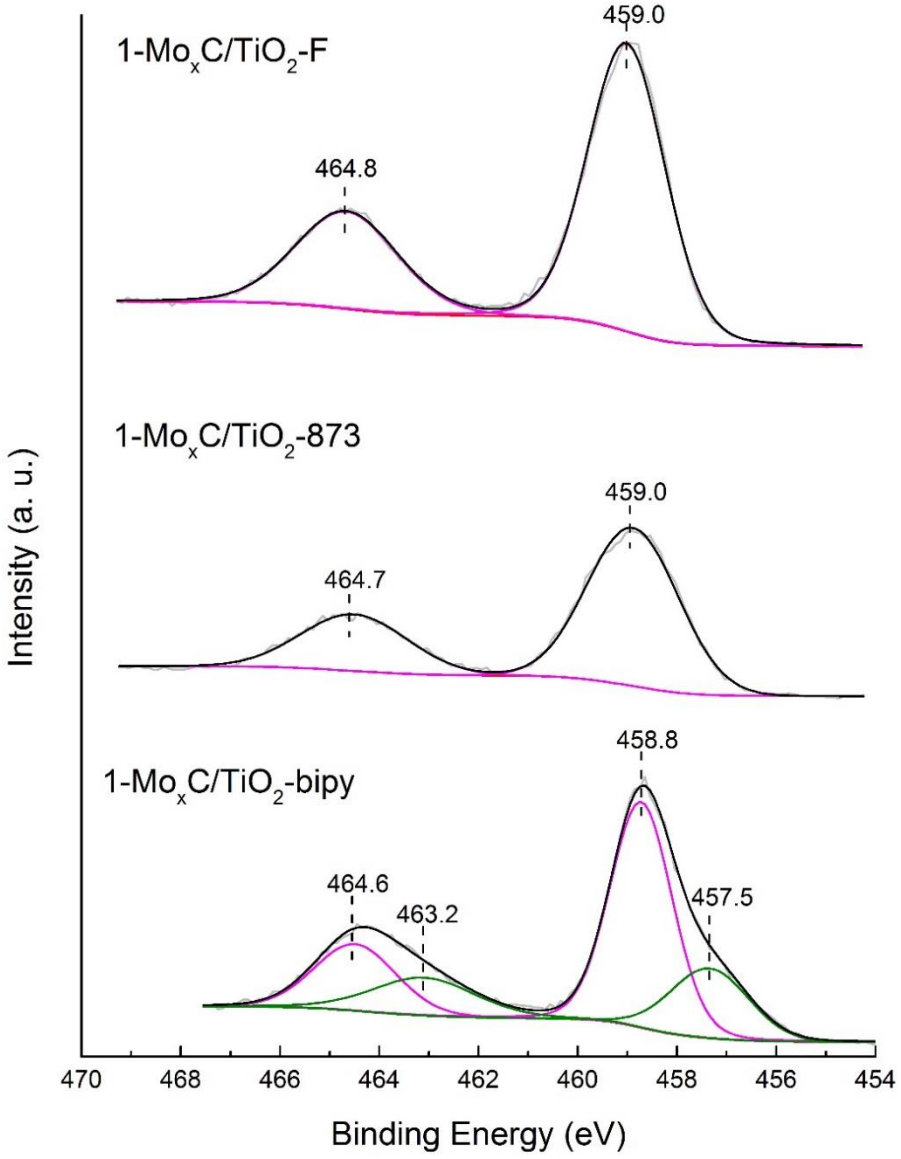

Figure 5.13. Ti 2p core level spectra of 1-Mo_xC/TiO_2(NS)-X and 1-Mo_xC/TiO_2(bipy) samples.

O 1s spectra of 1-Mo_xC/TiO_2(NS)-X and 1-Mo_xC/TiO_2(bipy) are shown in Figure 5.14. In all cases, two peaks at about 530.0 eV and 531.3-531.8 eV can be observed, which are associated with the surface oxide of TiO_2 and molybdenum oxide or oxycarbide species, respectively. Besides these two peaks, 1-Mo_xC/TiO_2(bipy) shows a shoulder with maximum of 528.4 eV, which could be related with the presence of oxygen interacting with Ti^{3+} [17]. From XPS characterization, a preferential reduction of bipyramidal TiO_2 induced by the Mo_xC can be proposed. This agrees with the different reducibility and barriers for oxygen vacancy migration reported for (101) and (001) surfaces [18].

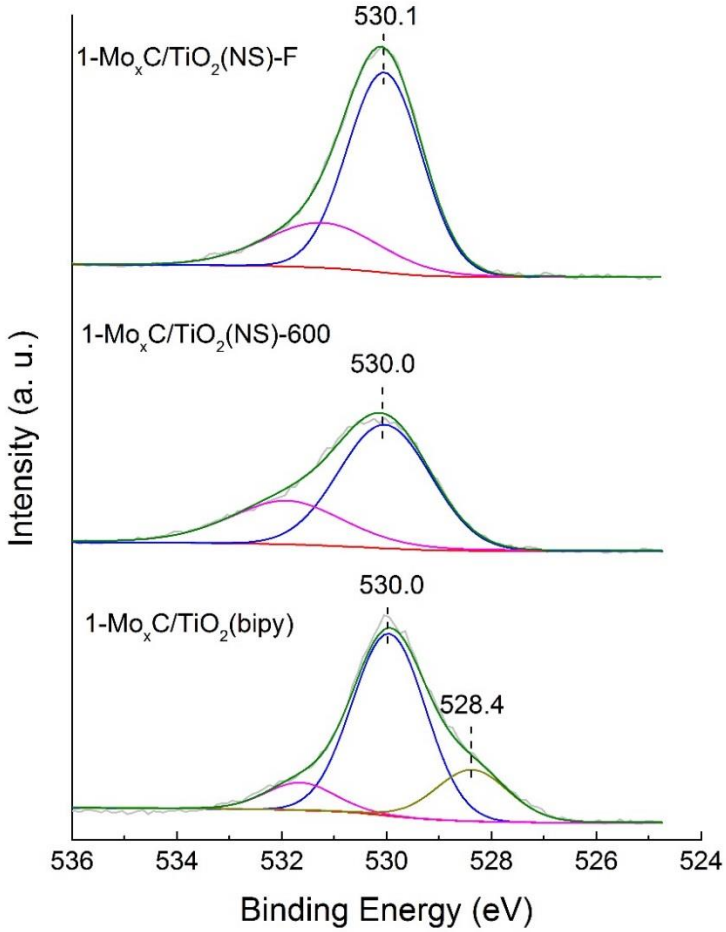

Figure 5.14. O 1s core-level spectra of 1-Mo_xC/TiO_2(NS)-X and 1-Mo_xC/TiO_2(bipy) samples.

Figure 5.15 shows F 1s core-level spectra. Only in 1-Mo_xC/TiO_2(NS)-F sample, clear peaks at 689.3 and 684.8 eV can be observed, which are attributed to organic and inorganic fluoride species, respectively [1]. For 1-Mo_xC/TiO_2(NS)-600 and 1-Mo_xC/TiO_2(bipy) samples, no signals were observed in this region, according to the characteristics of TiO_2(NS)-600 and TiO_2(bipy).

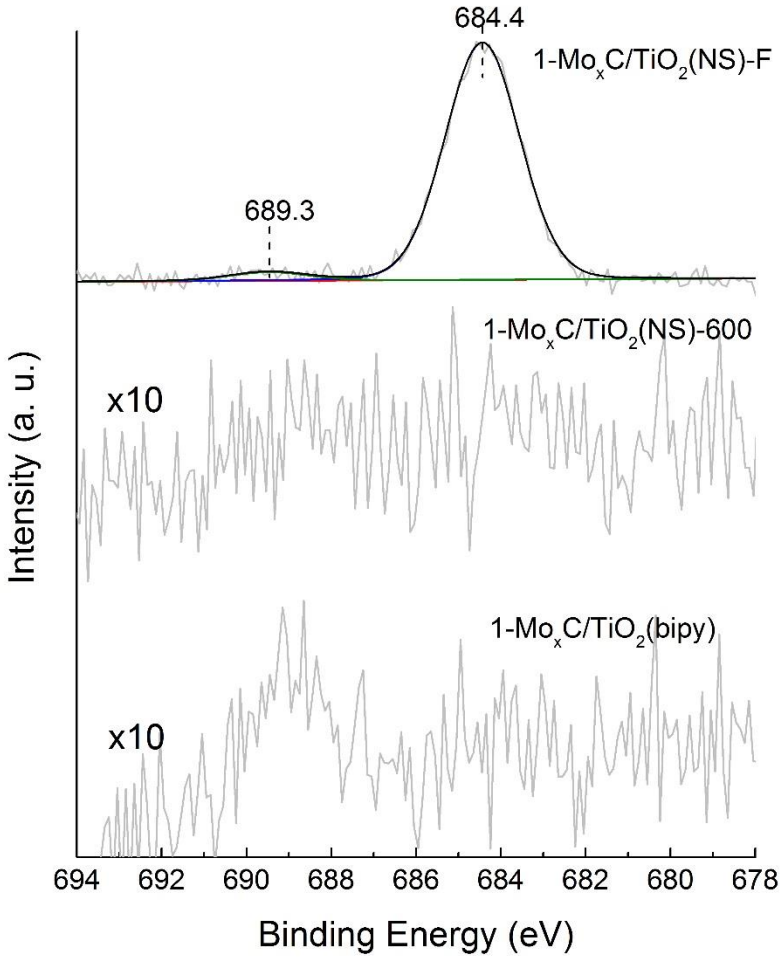

Figure 5.15. F 1s core-level spectra of 1-Mo_xC/TiO_2(NS)-X and 1-Mo_xC/TiO_2(bipy) samples.

UV-vis DRS analysis of 1-Mo_xC/TiO_2(NS)-X and 1-Mo_xC/TiO_2(bipy) samples were performed and the corresponding spectra appear in Figure 5.16.

In all cases, samples revealed a conspicuous absorption edge at about 390 nm, which agrees well with the band edge absorption of anatase TiO_2 [19]. 1-Mo_xC/TiO_2(bipy) exhibits a higher absorption in the visible region than 1-Mo_xC/TiO_2(NS)-F and 1-Mo_xC/TiO_2(NS)-600.

Figure 5.17 shows the Tauc plots of samples used for the bandgap energies determination [20]. The corresponding bandgap energies of 1-Mo_xC/TiO_2(NS)-F, 1-Mo_xC/TiO_2(NS)-600 and 1-Mo_xC/TiO_2(bipy) are estimated to be 3.27, 3.26 and 2.92 eV, respectively (Table 5.2, p. 160). There is no obvious difference between the bandgap energy values of 1-Mo_xC/TiO_2(NS)-X and their TiO_2(NS)-X counterparts (Table 5.1, p. 154). However, after introducing Mo_xC nanoparticles into TiO_2(bipy), the bandgap energy decreases from 3.10 to 2.92 eV, which could be correlated with the different surface chemistry of (101) and (001) surface already evidenced by XPS.

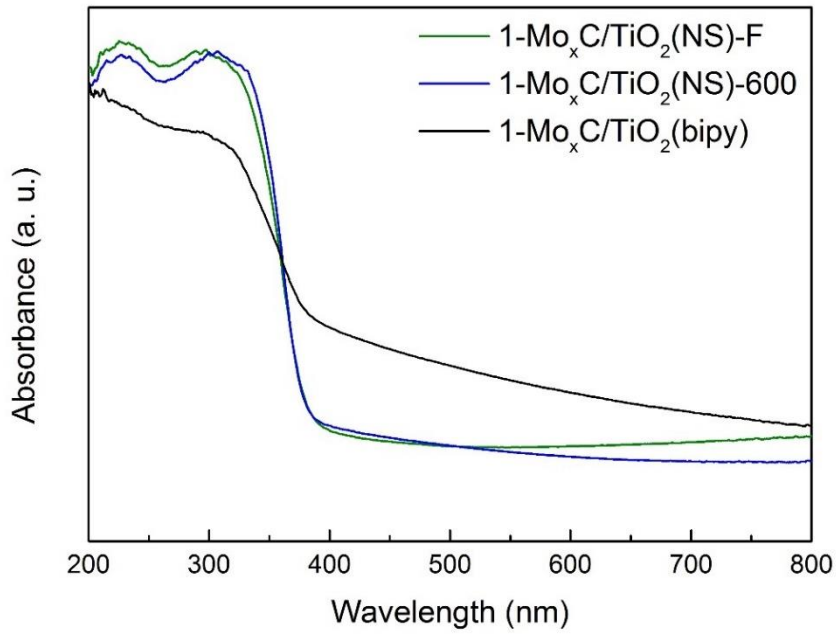

Figure 5.16. UV-vis diffuse reflectance spectra of 1-Mo_xC/TiO_2(NS)-X and 1-Mo_xC/TiO_2(bipy).

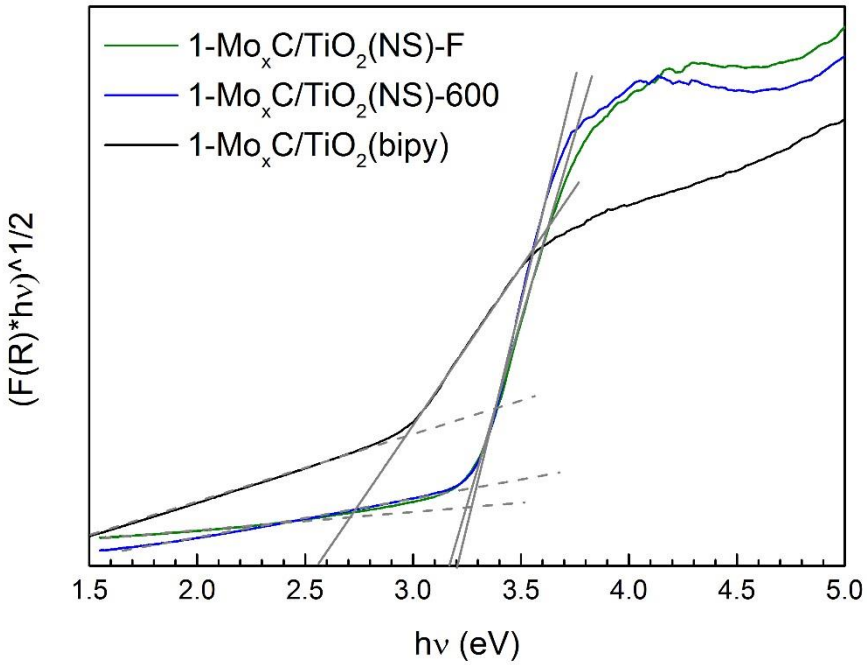

Figure 5.17. Tauc plots of the Kubelka-Munk function versus photonic energy of 1-Mo_xC/TiO_2(NS)-X and 1-Mo_xC/TiO_2(bipy).

The photoinduced charge recombination of samples was analyzed by PL spectroscopy. PL spectra of 1-Mo_xC/TiO_2(NS)-X, 1-Mo_xC/TiO_2(bipy), TiO_2(NS)-X and TiO_2(bipy) are shown in Figure 5.18. In all cases, a broad emission peak with maximum at about 595 nm can be observed, which can be related with the presence of a high density of defect sites [21]; specifically, peaks at about 495-540 nm have been related with the presence of surface oxygen vacancies and peaks at about 600-650 nm with that of subsurface oxygen vacancies [22].

On the other hand, the intensity of PL spectra of 1-Mo_xC/TiO_2(NS)-X and 1-Mo_xC/TiO_2(bipy) is lower than those of bare TiO_2(NS)-X and TiO_2(bipy), indicating that the presence of Mo_xC improves the efficiency of photogenerated h^+/e^- pairs separation. The intensity of PL band follows the order: TiO_2(NS)-F> TiO_2(NS)-600>TiO_2(bipy)>1-Mo_xC/TiO_2(NS)-F>1-Mo_xC/TiO_2(NS)-600>1-

Mo_xC/TiO_2(bipy). Both the morphology and adsorbed species on anatase TiO_2 greatly influence the photoinduced charge recombination. TiO_2(NS)-600 is more effective in lowering the charge recombination rate than TiO_2(NS)-F. Moreover, the recombination is less favored in TiO_2(bipy) nanoparticles.

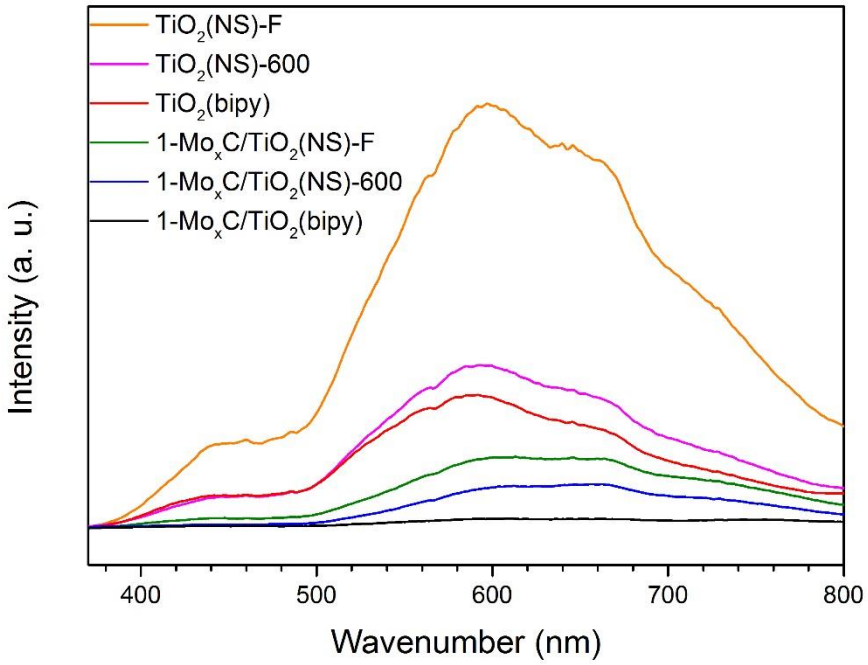

Figure 5.18. PL spectra of 1-Mo_xC/TiO_2(NS)-X, 1-Mo_xC/TiO_2(bipy), TiO_2(NS)-X and TiO_2(bipy) samples.

For a deeply evaluation of photogenerated charge transfer properties of the photocatalysts, transient photocurrent responses and EIS measurements were carried out.

Figure 5.19 shows the transient photocurrent responses of 1-Mo_xC/TiO_2(NS)-X, 1-Mo_xC/TiO_2(bipy), TiO_2(NS)-X and TiO_2(bipy) samples under simulated solar light irradiation with a pulse light on-off process. In general, Mo_xC containing samples show larger photocurrent density than the corresponding TiO_2 samples. However, this effect is much higher for TiO_2(bipy)

than for TiO_2(NS)-X. The order of photocurrent density responses is: 1-Mo_xC/TiO_2(bipy)>>TiO_2(bipy)>>1-Mo_xC/TiO_2(NS)-600>1-Mo_xC/TiO_2(NS)-F> TiO_2(NS)-600>TiO_2(NS)-F.

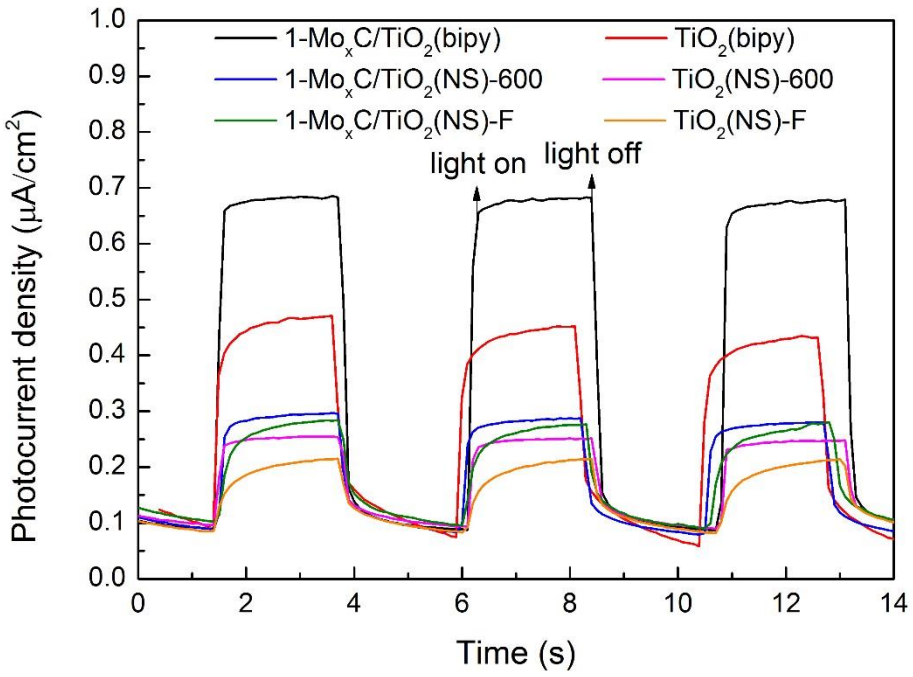

Figure 5.19. Photocurrent response of 1-Mo_xC/TiO_2(NS)-X, 1-Mo_xC/TiO_2(bipy), TiO_2(NS)-X and TiO_2(bipy) samples.

The EIS Nyquist plots of as-made samples obtained in dark and under simulated solar irradiation are shown in Figures 5.20 and 5.21, respectively. In all cases, 1-Mo_xC/TiO_2(NS)-X and 1-Mo_xC/TiO_2(bipy) samples show smaller arc radius than bare TiO_2(NS)-X and TiO_2(bipy), which indicates that the presence of Mo_xC onto TiO_2(NS)-X and TiO_2(bipy) reduces the transport resistance of photogenerated electrons, both in dark and illuminated conditions. Meanwhile, in all cases, the arc radius under solar illumination is smaller than in dark conditions; the irradiation produces photogenerated electrons and decreases the barrier of the electron transfer in these materials. The Nyquist

arc radius follows the order: TiO_2(NS)-F>TiO_2(NS)-600>1-Mo_xC/TiO_2(NS)-600> 1-Mo_xC/TiO_2(NS)-F>TiO_2(bipy)>1-Mo_xC/TiO_2(bipy) in both conditions. This result is in good agreement with PL and photocurrent responses characterization, and highlights the importance of the Mo_xC/TiO_2 interfaces on the composite photochemical characteristics.

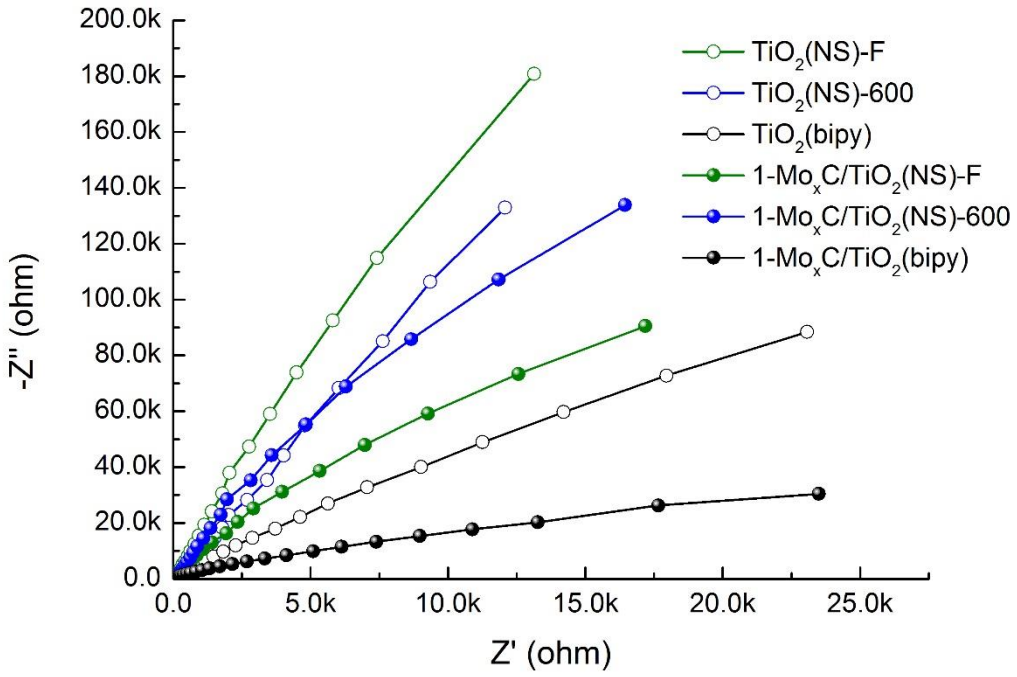

Figure 5.20. EIS Nyquist plots of 1-Mo_xC/TiO_2(NS)-X, 1-Mo_xC/TiO_2(bipy), TiO_2(NS)-X and TiO_2(bipy) in dark.

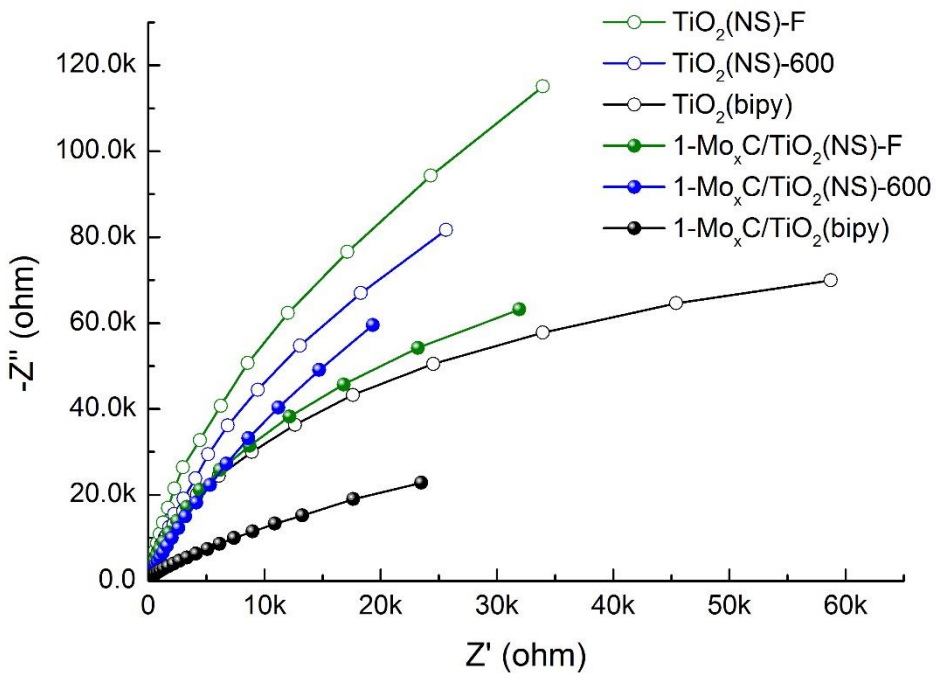

Figure 5.21. EIS Nyquist plots of 1-Mo_xC/TiO_2(NS)-X, 1-Mo_xC/TiO_2(bipy), TiO_2(NS)-X and TiO_2(bipy) samples under simulated solar irradiation.

5.3 Photocatalytic H_2 production over 1-Mo_xC/TiO_2(NS)-X and 1-Mo_xC/TiO_2(bipy)

As stated above, 1-Mo_xC/TiO_2(NS)-X and 1-Mo_xC/TiO_2(bipy) were used as photocatalysts (250 mg) for the H_2 production from ethanol$_{(aq)}$ (25% v/v). For comparison, TiO_2(NS)-X and TiO_2(bipy) samples were also tested. The results of H_2 production yield along time are displayed in Figure 5.22 and the corresponding AQE values in Figure 5.23.

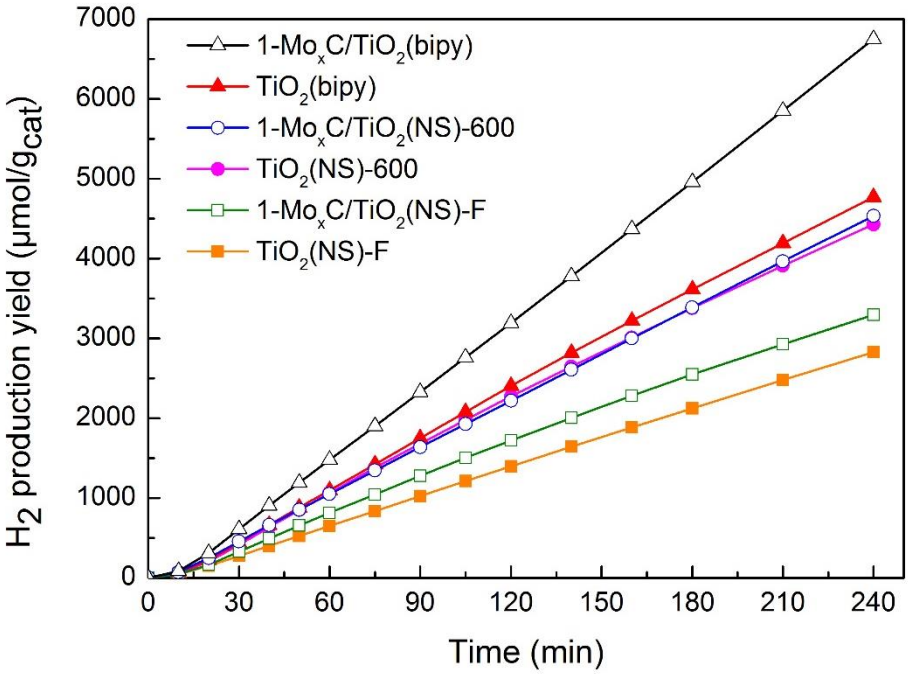

Figure 5.22. Total H_2 yield per gram of catalyst produced from ethanol$_{(aq)}$ 25% v/v over 1-Mo_xC/TiO_2(NS)-X, 1-Mo_xC/TiO_2(bipy), TiO_2(NS)-X and TiO_2(bipy). t= 4 h, T= 20 °C, UV-vis irradiation.

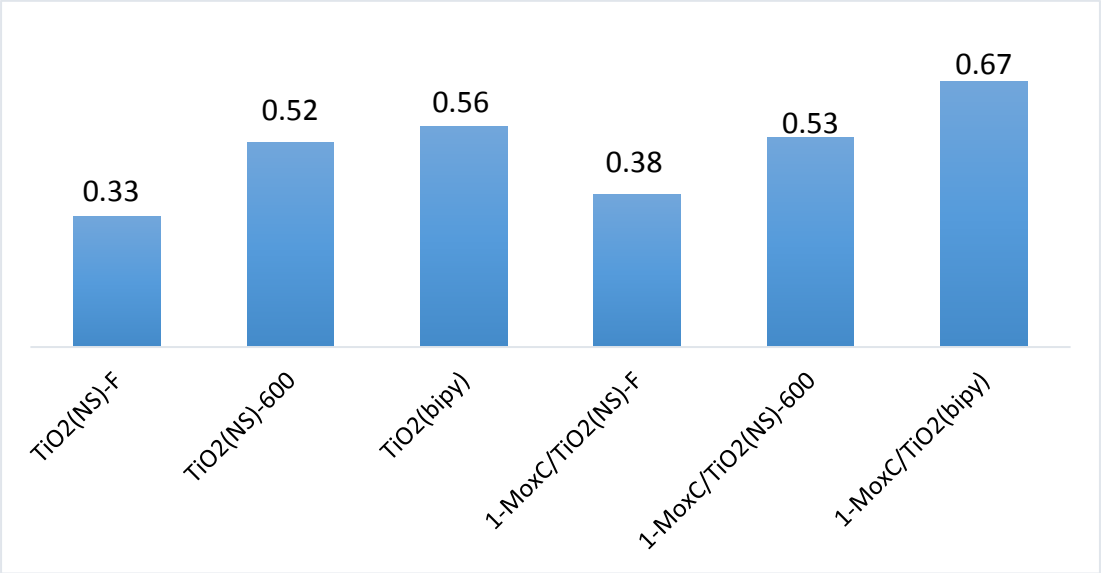

Figure 5.23. AQE (%) for H_2 production from ethanol$_{(aq)}$ 25% v/v over 1-Mo_xC/TiO_2(NS)-X, 1-Mo_xC/TiO_2(bipy), TiO_2(NS)-X and TiO_2(bipy) photocatalysts.

All TiO_2 samples are active in the photocatalytic H_2 production under UV-visible irradiation from ethanol$_{(aq)}$ solution, the amount of hydrogen produced and the AQE followed the order: TiO_2(bipy)>TiO_2(NS)-600>>TiO_2(NS)-F (Figures 5.22 and 5.23). It indicates that the presence of fluorides on the surface could produce a detrimental effect on H_2 production. A similar result has been recently reported for the formic acid photoreforming [23]. Moreover, the bipyramidal shape of TiO_2(bipy) sample with dominant (101) facets shows the highest H_2 production (4772 μmol•g^{-1}). TiO_2(bipy) mainly exposes (101) facets, which favours the electron transfer for the H_2 production, as has been proved using methanol as the sacrificial agent [24].

On the other hand, all the Mo_xC containing samples show a higher H_2 production than their respective TiO_2(NS)-X and TiO_2(bipy) (Figures 5.22 and 5.23). This result demonstrates the role of Mo_xC as co-catalyst, which depended on the TiO_2 used (Figure 5.22). The amount of hydrogen produced and the AQE followed the trend: 1-Mo_xC/TiO_2(bipy)>1-Mo_xC/TiO_2(NS)-600>1-Mo_xC/TiO_2(NS)-F, indicating the paramount importance of the shape of TiO_2 nanoparticles.

To be specific, as both TiO_2(NS)-600 and TiO_2(bipy) show surface fluoride-free but different ratios of facets, they are suitable to compare the effect of Mo_xC as co-catalysts on TiO_2 with different dominant facets.

H_2 production over 1-Mo_xC/TiO_2(NS)-600 catalyst is only slightly higher than over TiO_2(NS)-600. However, H_2 production over 1-Mo_xC/TiO_2(bipy) increased almost 41% when it is compared with the bare TiO_2(bipy). According to the characteristics of as-prepared samples, we relate the higher effect of Mo_xC onto TiO_2(bipy) with the preferential deposition of Mo_xC nanoparticles onto (101) facets and with the presence of surface Ti^{3+}, as it was determined by XPS. As stated above, the electron transfer, which is necessary for H_2

production, is favored onto (101) facets [25,26]. Moreover, an improved photocatalytic activity has been demonstrated for TiO_2 nanoparticles containing Ti^{3+} surface species, being the presence of surface defects related with a lower recombination rate [27,28].

Besides H_2, C1 (CO and CH_4) and C2 (C_2H_4 and CH_3CHO) products were also detected in the gas phase during the photoreaction (Table 5.3). In the liquid phase, 2,3-butanediol was the main product detected.

Table 5.3. Products obtained (μmol/g_{cat}) during the photocatalytic H_2 production tests using ethanol$_{(aq)}$ 25% v/v with TiO_2-X and Mo_xC/TiO_2-X catalysts (250 mg) under UV-vis irradiation. Other reaction conditions: 20 °C, t=4 h.

Catalyst	H_2	CO	CH_4	C_2H_4	CH_3CHO[a]	2,3-butanediol
TiO_2(NS)-F	2826	185	120	29	82	1430
TiO_2(NS)-600	4429	163	120	32	73	1525
TiO_2(bipy)	4772	183	103	28	54	5958
1-Mo_xC/TiO_2(NS)-F	3297	190	122	31	81	2460
1-Mo_xC/TiO_2(NS)-600	4533	212	116	46	83	4972
1-Mo_xC/TiO_2(bipy)	6748	224	138	53	83	5502

[a] CH_3CHO in liquid phase was not quantified.

5.4 Influence of Mo_xC loading amount on TiO_2(bipy)

Taking into account that 1-Mo_xC/TiO_2(bipy) produced the highest amount of hydrogen, two more Mo_xC/TiO_2(bipy) catalysts with different Mo_xC loading, 0.5-Mo_xC/TiO_2(bipy) and 3.5-Mo_xC/TiO_2(bipy) were prepared following the same procedure (Table 5.4).

Table 5.4. Average dimensions of crystal domains obtained by Scherrer analysis of the (004) and (200) XRD peaks, BET surface area, Mo content and bandgap of TiO_2(bipy) and 0.5-, 1-, and 3.5-Mo_xC/TiO_2(bipy) samples.

Catalyst	d_{004} (nm)	d_{200} (nm)	S_{BET} (m^2/g)	Mo content (wt%)	Bandgap (eV)
TiO_2(bipy)	40	31	27	--	3.10
0.5-Mo_xC/TiO_2(bipy)	36	29	38	0.50	3.10
1-Mo_xC/TiO_2(bipy)	36	29	15	0.69	2.92
3.5-Mo_xC/TiO_2(bipy)	25	20	26	3.25	2.85

XRD patterns of all Mo_xC/TiO_2(bipy) samples only show characteristic diffraction peaks of anatase TiO_2 (Figure 5.24). On the other hand, the average crystallite dimensions of 3.5-Mo_xC/TiO_2(bipy) are lower than those of samples containing a lower Mo_xC loading (Table 5.4).

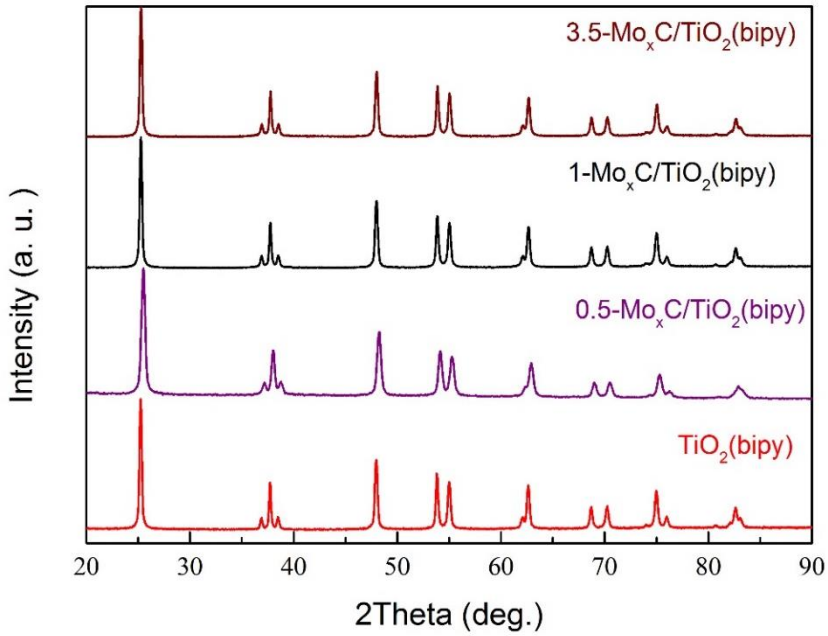

Figure 5.24. XRD diffraction patterns of TiO_2(bipy) and 0.5-, 1-, and 3.5-Mo_xC/TiO_2(bipy).

The bandgap values of Mo_xC/TiO_2(bipy) samples recorded in Table 5.4 were determined from Tauc plots (Figure 5.25); a decrease of the bandgap can be observed with the increase of Mo_xC loading, which could be related with the progressive deposition of Mo_xC onto (101) facets.

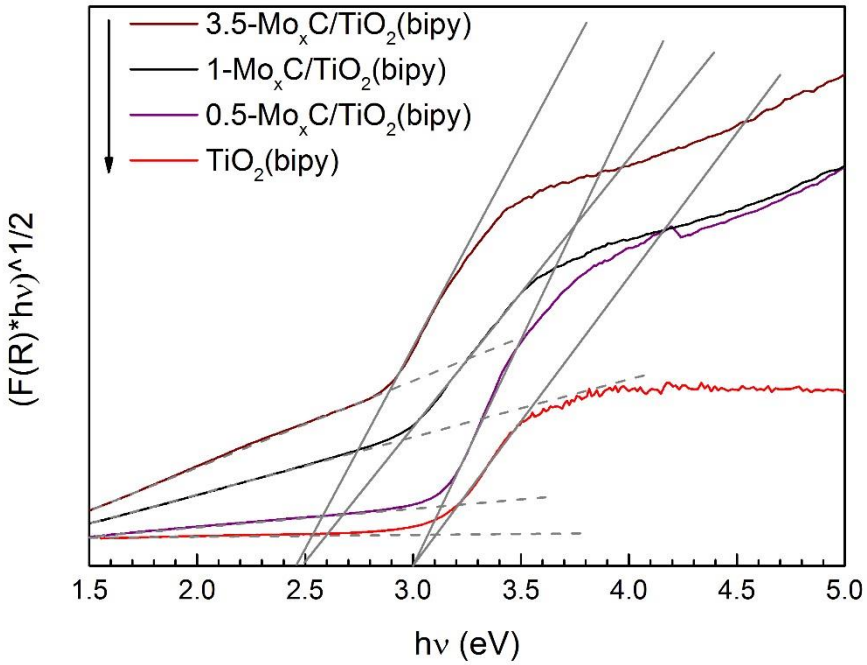

Figure 5.25. Tauc plots of the Kubelka-Munk function versus photonic energy of TiO_2(bipy) and 0.5-, 1-, and 3.5-Mo_xC/TiO_2(bipy).

Moreover, photoelectrochemical measurements, including PL, transient photocurrent responses and EIS measures were also carried out to determine the photoinduced charge recombination and the photogenerated charge transfer for all Mo_xC/TiO_2(bipy) samples.

PL spectra of Mo_xC/TiO_2(bipy) samples and TiO_2(bipy) are shown in Figure 5.26. All PL spectra of Mo_xC-containing samples show lower intensity than that of bare TiO_2(bipy). The intensity of PL spectra follows the trend: TiO_2(bipy)>> 0.5-Mo_xC/TiO_2(bipy)>3.5-Mo_xC/TiO_2(bipy)>1-Mo_xC/TiO_2(bipy), this indicating that the 1-Mo_xC/TiO_2(bipy) is the most effective in the photoinduced separation charge.

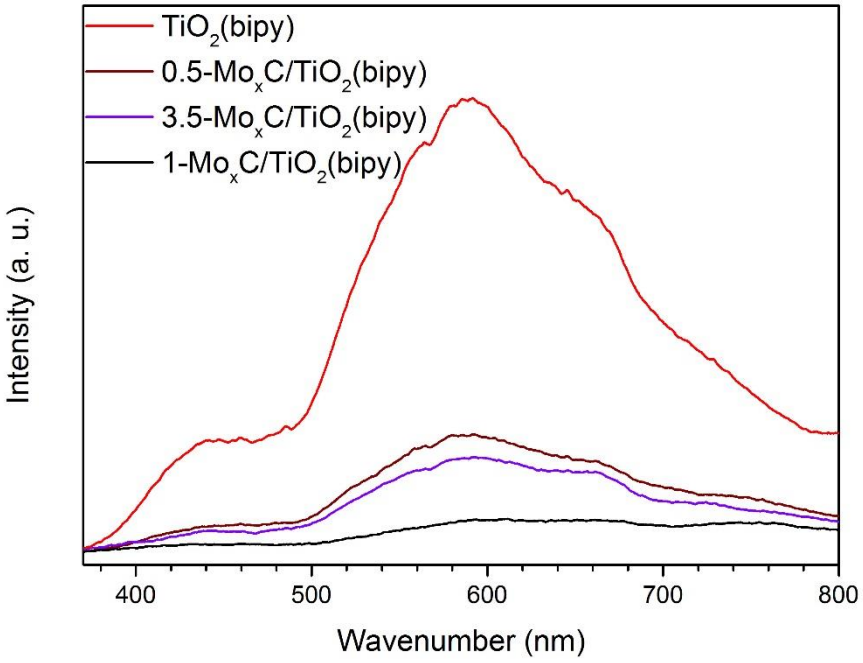

Figure 5.26. Photoluminescence spectra of TiO_2(bipy) and 0.5-, 1-, and 3.5-Mo_xC/TiO_2(bipy) samples.

Figure 5.27 shows the transient photocurrent responses of TiO_2(bipy) and 0.5-, 1-, 3.5-Mo_xC/TiO_2(bipy) samples. All the Mo_xC/TiO_2(bipy) samples exhibit a higher photocurrent response than that of TiO_2(bipy), following the trend: 1-Mo_xC/TiO_2(bipy)>3.5-Mo_xC/TiO_2(bipy)>0.5-Mo_xC/TiO_2(bipy)>TiO_2(bipy). The lower the rate of photogenerated charge recombination, the higher photocurrent density.

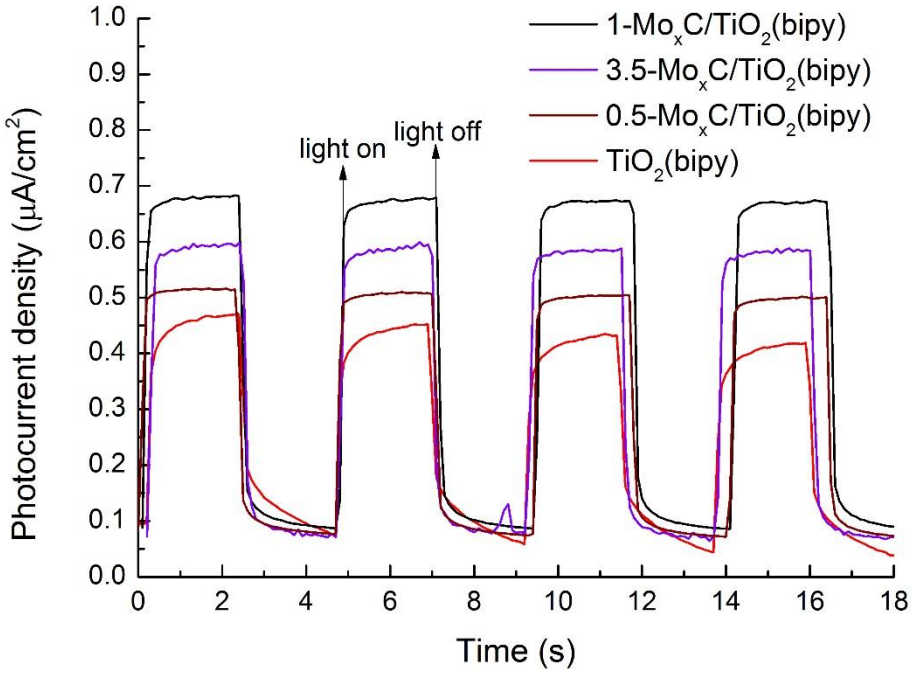

Figure 5.27. Photocurrent response of TiO_2(bipy) and 0.5-, 1-, and 3.5-Mo_xC/TiO_2(bipy) samples.

Figures 5.28 and 5.29 show the EIS Nyquist plots of TiO_2(bipy) and Mo_xC/TiO_2(bipy) samples obtained in dark and under simulated solar irradiation, respectively. In all cases, Mo_xC containing samples (Mo_xC/TiO_2(bipy)) show a smaller arc radius than bare TiO_2(bipy); on the other hand, all the arc radius under solar illumination are smaller than in dark conditions. The Nyquist arc radius follows the order: TiO_2(bipy)>0.5-Mo_xC/TiO_2(bipy)>3.5-Mo_xC/TiO_2(bipy)>1-Mo_xC/TiO_2(bipy). Samples showing a lower barrier of electron transfer also showed a lower rate of photogenerated charge recombination and a higher photocurrent density.

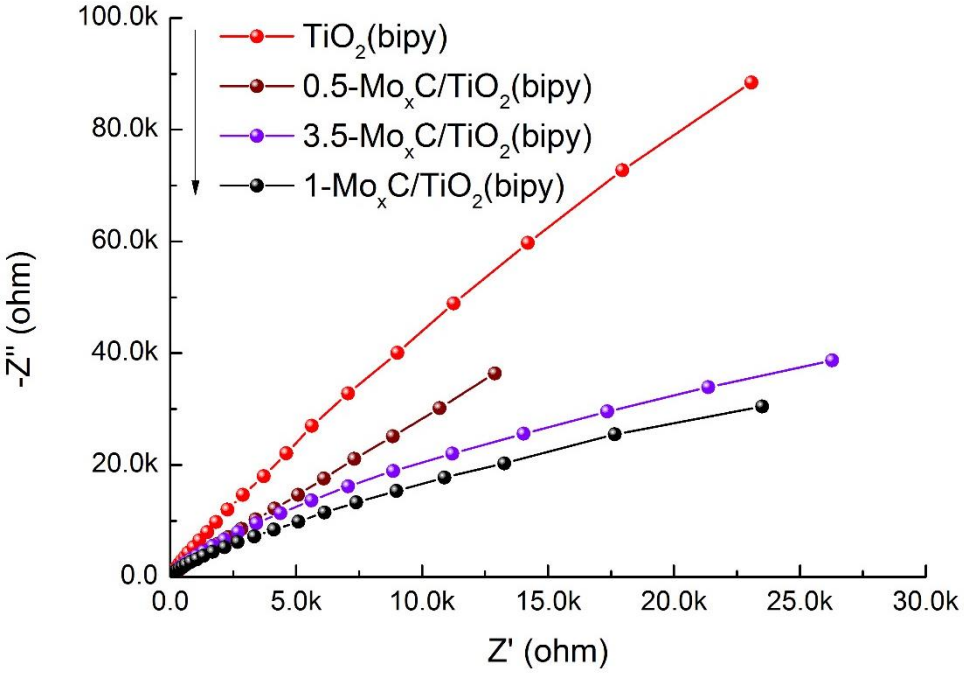

Figure 5.28. EIS Nyquist plots of TiO_2(bipy) and 0.5-, 1-, and 3.5-Mo_xC/TiO_2(bipy) samples in dark.

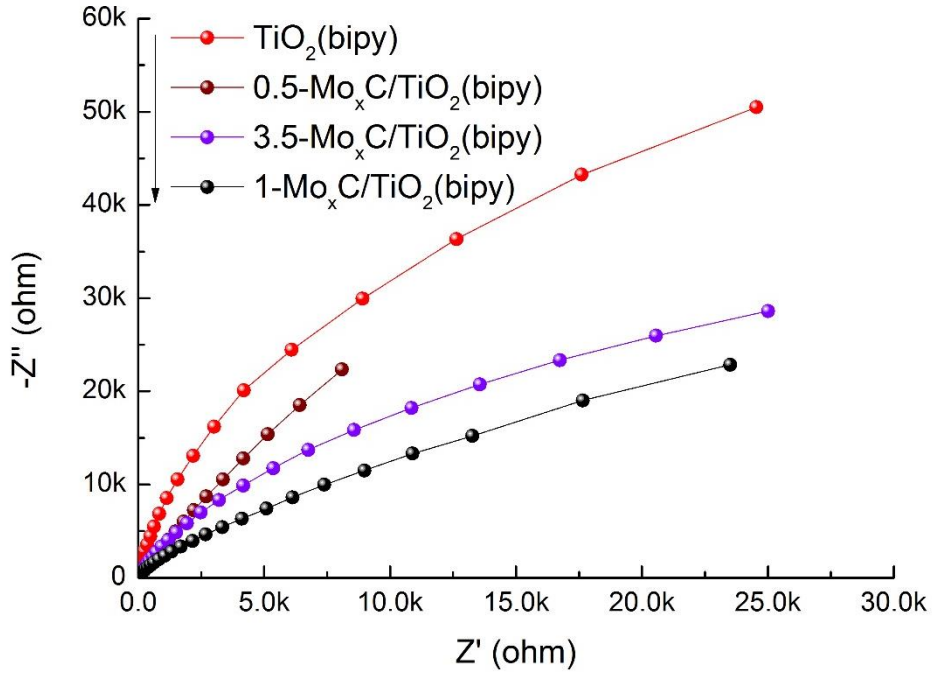

Figure 5.29. EIS Nyquist plots of TiO_2(bipy) and 0.5-, 1-, and 3.5-Mo_xC/TiO_2(bipy) samples under simulated solar irradiation.

Figure 5.30 shows the H_2 yield along time of all Mo_xC/TiO_2(bipy) and TiO_2(bipy) samples, and Table 5.5 the C-containing products obtained. Besides the main production of H_2, the presence of other carbon-containing products (CO, CH_4, C_2H_4 and CH_3CHO) were determined in the gas phase during the photoreaction; 2,3-butanediol was the main product detected in the liquid phase (Table 5.5).

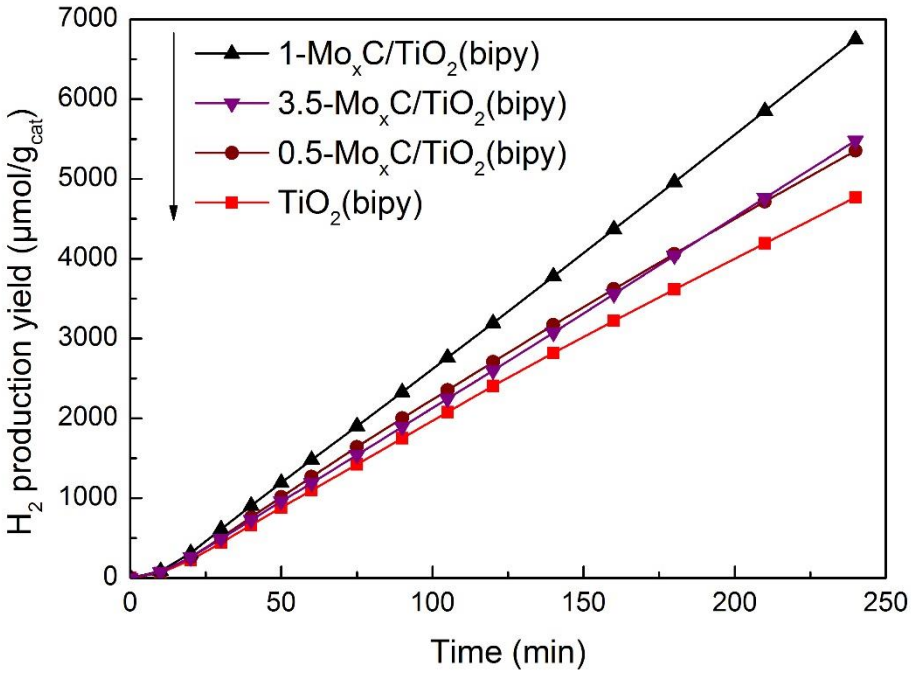

Figure 5.30. Total H_2 yield per gram of catalyst produced from ethanol$_{(aq)}$ 25% v/v over 0.5-, 1-, and 3.5-Mo_xC/TiO_2(bipy) photocatalysts. t= 4 h, T= 20 °C, UV-visible light irradiation.

As expected, all Mo_xC/TiO_2(bipy) showed higher H_2 yield than bare TiO_2(bipy). Moreover, the photocatalyst with about 0.7% wt Mo_xC (1-Mo_xC/TiO_2-bipy) produced the highest amount of H_2, according to its photoelectrochemical properties. This sample, which showed the lowest rate of photoinduced charge recombination, has the highest transient photocurrent

response and the lowest barrier of electron transfer. 1-Mo_xC/TiO_2(bipy) also showed the highest AQE (Figure 5.31).

Table 5.5. Products obtained (μmol/g_{cat}) during the photocatalytic H_2 production tests using ethanol$_{(aq)}$ 25% v/v with TiO_2(bipy) and Mo_xC/TiO_2(bipy) catalysts under UV-vis irradiation. Other reaction conditions: 20 °C, t=4 h.

Catalyst	H_2	CO	CH_4	C_2H_4	CH_3CHO[a]	2,3-butanediol
TiO_2(bipy)	4772	183	103	28	54	5958
0.5-Mo_xC/TiO_2(bipy)	5352	90	136	39	74	7388
1-Mo_xC/TiO_2(bipy)	6748	224	138	53	83	5502
3.5-Mo_xC/TiO_2(bipy)	5477	170	128	34	73	9692

[a] CH_3CHO in liquid phase was not quantified.

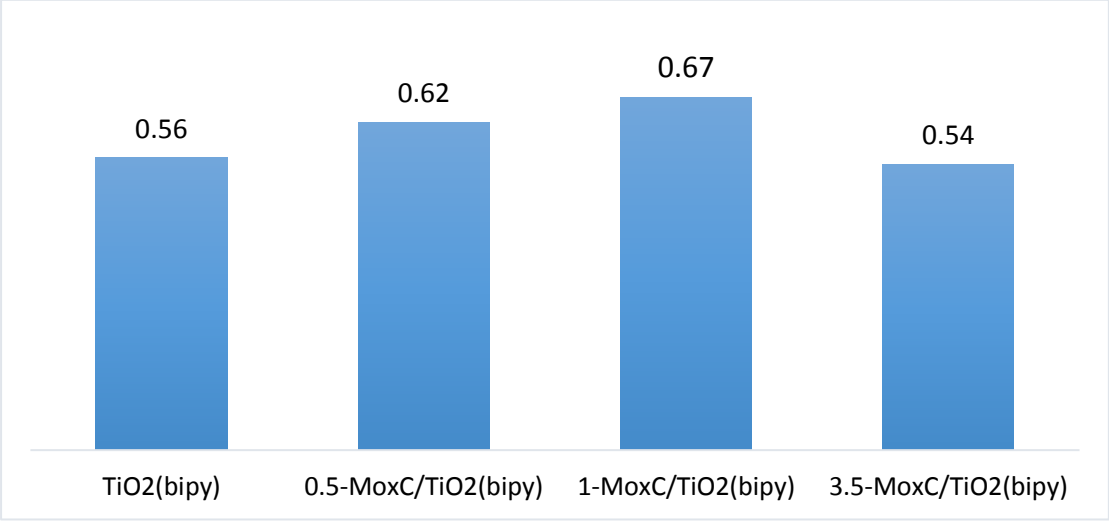

Figure 5.31. AQE (%) for H_2 production from ethanol$_{(aq)}$ 25% v/v over TiO_2(bipy) and 0.5-, 1-, and 3.5-Mo_xC/TiO_2(bipy) photocatalysts.

These results show the beneficial effect of Mo_xC as co-catalyst in TiO_2(bipy) at least till 0.7% wt. However, a Mo_xC content of 3.5% wt is higher than the optimal value, being the sample 3.5-MoxC/TiO_2(bipy) located at the right side of the volcano plot.

5.5 References

1. Mino L, Pellegrino F, Rades S, et al. Beyond shape engineering of TiO_2 nanoparticles: post-synthesis treatment dependence of surface hydration, hydroxylation, Lewis acidity and photocatalytic activity of TiO_2 anatase nanoparticles with dominant {001} or {101} facets. ACS Applied Nano Materials, 2018, 1: 5355-5365.

2. Han X, Kuang Q, Jin M, et al. Synthesis of titania nanosheets with a high percentage of exposed (001) facets and related photocatalytic properties. Journal of the American Chemical Society, 2009, 131: 3152-3153.

3. Zhang J, Wang J, Zhao Z, et al. Reconstruction of the (001) surface of TiO_2 nanosheets induced by the fluorine-surfactant removal process under UV-irradiation for dye-sensitized solar cells. Physical Chemistry Chemical Physics, 2012, 14: 4763-4769.

4. Sugimoto T, Zhou X, Muramatsu A. Synthesis of uniform anatase TiO_2 nanoparticles by gel–sol method: 3. Formation process and size control. Journal of colloid and interface science, 2003, 259: 43-52.

5. Luca V. Comparison of size-dependent structural and electronic properties of anatase and rutile nanoparticles. The Journal of Physical Chemistry C, 2009, 113: 6367-6380.

6. Snyder R L. The use of reference intensity ratios in X-ray quantitative

analysis. Powder Diffraction, 1992, 7: 186-193.

7. Yang H G, Zeng H C. Preparation of hollow anatase TiO_2 nanospheres via Ostwald ripening. The Journal of Physical Chemistry B, 2004, 108: 3492-3495.

8. Chen M, Liu J, Zhou W, et al. Nitrogen-doped graphene-supported transition-metals carbide electrocatalysts for oxygen reduction reaction. Scientific Reports, 2015, 5: 10389.

9. Jiang J, Liu Q, Zeng C, et al. Cobalt/molybdenum carbide@ N-doped carbon as a bifunctional electrocatalyst for hydrogen and oxygen evolution reactions. Journal of Materials Chemistry A, 2017, 5: 16929-16935.

10. Zhu Y, Wang S, Zhong Y, et al. Facile synthesis of a MoO_2–Mo_2C–C composite and its application as favorable anode material for lithium-ion batteries. Journal of Power Sources, 2016, 307: 552-560.

11. Ojha K, Saha S, Kolev H, et al. Composites of graphene-Mo_2C rods: highly active and stable electrocatalyst for hydrogen evolution reaction. Electrochimica Acta, 2016, 193: 268-274.

12. Oshikawa K, Nagai M, Omi S. Characterization of molybdenum carbides for methane reforming by TPR, XRD, and XPS. The Journal of Physical Chemistry B, 2001, 105: 9124-9131.

13. Porosoff M D, Yang X, Boscoboinik J A, et al. Molybdenum carbide as alternative catalysts to precious metals for highly selective reduction of CO_2 to CO. Angewandte Chemie International Edition, 2014, 53: 6705-6709.

14. Gao Q, Zhao X, Xiao Y, et al. A mild route to mesoporous Mo_2C–C hybrid nanospheres for high performance lithium-ion batteries. Nanoscale, 2014, 6: 6151-6157.

15. Khan M M, Ansari S A, Pradhan D, et al. Band gap engineered TiO_2 nanoparticles for visible light induced photoelectrochemical and photocatalytic studies. Journal of Materials Chemistry A, 2014, 2: 637-644.

16. Yan Y, Han M, Konkin A, et al. Slightly hydrogenated TiO_2 with enhanced photocatalytic performance. Journal of Materials Chemistry A, 2014, 2: 12708-12716.

17. Sola A C, Ramírez de la Piscina P, Homs N. Behaviour of Pt/TiO_2 catalysts with different morphological and structural characteristics in the photocatalytic conversion of ethanol aqueous solutions. Catalysis Today, 2020, 341: 13-20.

18. Selcuk S, Zhao X, Selloni A. Structural evolution of titanium dioxide during reduction in high-pressure hydrogen. Nature Materials, 2018, 17: 923-928.

19. Eder D, Motta M, Windle A H. Iron-doped $Pt–TiO_2$ nanotubes for photo-catalytic water splitting. Nanotechnology, 2009, 20: 055602.

20. Makuła P, Pacia M, Macyk W. How to correctly determine the band gap energy of modified semiconductor photocatalysts based on UV–Vis spectra. The Journal of Physical Chemistry Letters, 2018, 9: 6814-6817.

21. Li W, Shang C, Li X. A one-step thermal decomposition method to prepare anatase TiO_2 nanosheets with improved adsorption capacities and enhanced photocatalytic activities. Applied Surface Science, 2015, 357: 2223-2233.

22. Pallotti D K, Passoni L, Maddalena P, et al. Photoluminescence mechanisms in anatase and rutile TiO_2. The Journal of Physical Chemistry C, 2017, 121: 9011-9021.

23. Pellegrino F, Sordello F, Mino L, et al. Formic acid photoreforming for

hydrogen production on shape-controlled anatase TiO_2 nanoparticles: Assessment of the role of fluorides,{101}/{001} surfaces ratio, and platinization. ACS Catalysis, 2019, 9: 6692-6697.

24. Gordon T R, Cargnello M, Paik T, et al. Nonaqueous synthesis of TiO_2 nanocrystals using TiF_4 to engineer morphology, oxygen vacancy concentration, and photocatalytic activity. Journal of the American Chemical Society, 2012, 134: 6751-6761.

25. Sun D, Yang W, Zhou L, et al. The selective deposition of silver nanoparticles onto {101} facets of TiO_2 nanocrystals with co-exposed {001}/{101} facets, and their enhanced photocatalytic reduction of aqueous nitrate under simulated solar illumination. Applied Catalysis B: Environmental, 2016, 182: 85-93.

26. Kashiwaya S, Olivier C, Majimel J, et al. Nickel oxide selectively deposited on the {101} Facet of anatase TiO_2 nanocrystal bipyramids for enhanced photocatalysis. ACS Applied Nano Materials, 2019, 2: 4793-4803.

27. Yan Y, Han M, Konkin A, et al. Slightly hydrogenated TiO_2 with enhanced photocatalytic performance. Journal of Materials Chemistry A, 2014, 2: 12708-12716.

28. Yaghoubi H, Li Z, Chen Y, et al. Toward a visible light-driven photocatalyst: the effect of midgap-states-induced energy gap of undoped TiO_2 nanoparticles. ACS Catalysis, 2015, 5: 327-335.

Chapter 6.

Conclusions

New mesoporous hybrid materials (Ti-PMOs), based on periodic organosilicas, with biphenyl moieties and containing Ti (Si/Ti=10-40 mol/mol), were successfully prepared following a microwave-assisted method. Ti-PMOs are mesoscopically ordered, show molecular-scale periodicity in the pore walls and surface-areas in the range of 740-830 m^2g^{-1}.

The photocatalytic transformation of aqueous ethanol (25% v/v) over Ti-PMOs produces H_2 and 2,3-butanediol as main carbon-containing product. The photocatalytic performance in hydrogen production of Ti-PMOs is higher than that of Ti-free PMO. After illumination, the electron transfer from organic groups to Ti^{4+} centers could favour the charge separation. Ti20-PMO (Si/Ti=23 mol/mol) shows the best photocatalytic behaviour, with a mean H_2 production of 511 μmol H_2 g_{cat}^{-1} h^{-1} during the photocatalytic test (4h). Ti20-PMO is stable under the conditions used, keeping a constant H_2 production rate along time. Ti20-PMO shows the lowest velocity of (e^-/h^+) charge recombination, the lowest electron transport resistance, and the highest transient photocurrent response. We relate these photoelectrochemical characteristics with the photocatalytic behaviour of Ti20-PMO and with the presence of dispersed tetrahedral Ti^{4+} centers in the Ti20-PMO framework.

On the other hand, the CO_2 photoreduction studies carried out using Ti-PMOs as photocatalysts and TEOA as SED, indicate that at least a part of C1 and C2 products obtained came from the TEOA. The evaluation of the behavior of SED, in the conditions used in the photocatalytic test, is of fundamental importance. Moreover, for an appropriate interpretation of the CO_2 photoreduction results, a test in the absence of CO_2 should be always performed.

Mo_xC is an effective co-catalyst for g-C_3N_4 and TiO_2 systems in the photocatalytic production of H_2 from aqueous ethanol (25% v/v), under UV-visible (Mo_xC/TiO_2(X)) and visible (Mo_xCT/g-C_3N_4) irradiation.

The preparation of tailored nanocomposites Mo_xCT/g-C_3N_4, containing hcp Mo_2C and/or fcc MoC onto g-C_3N_4 nanosheets, was accomplished using g-C_3N_4 nanosheets and Mo_xC nanoparticles previously synthesized and an ultrasonic-assisted method; the characteristics of g-C_3N_4 nanosheets and Mo_xC used in the preparation are kept in Mo_xCT/g-C_3N_4.

The photoelectrochemical properties of Mo_xCT/g-C_3N_4 depend on the phase and size of the Mo_xC used, and they can be related with the effect of Mo_xC as co-catalyst in g-C_3N_4, in the photocatalytic hydrogen production. The activity of Mo_xCT/g-C_3N_4 containing hcp Mo_2C is higher than that of photocatalysts containing only fcc MoC. Moreover, the photocatalytic activity increases with the decrease of the crystallite size of the hcp Mo_2C phase. On the other hand, the close presence of both phases results beneficial for the photocatalytic behaviour. The highest hydrogen production, about 255 μmol H_2 g^{-1}_{cat} h^{-1}, was obtained with Mo_xC700/g-C_3N_4, containing hcp Mo_2C and fcc MoC nanoparticles, and exhibiting the lowest rate of charge recombination, the lowest electron transfer resistance and the highest photocurrent response.

The study of engineered Mo_xC/TiO_2 materials in which Mo_xC nanoparticles were incorporated onto anatase TiO_2 nanoparticles with different geometries, nanosheets and bipyramidal, allowed to determine the paramount importance of the Mo_xC-TiO_2 interface in the photocatalytic behaviour of the samples. The doping of the shape-controlled anatase nanoparticles with Mo_xC, decreased the e^-/h^+ recombination rate and the electron transfer resistance; meanwhile, the

photocurrent response increased. The efficiency of the photocatalysts in the hydrogen production can be correlated with the amount of exposed (101) TiO_2 facets and their photoelectrochemical characteristics. The incorporation of Mo_xC nanoparticles onto bipyramidal anatase with dominant (101) facets favoured the formation of Ti^{3+} species. The cooperative effect between the reducibility of the anatase (101) surface and the presence of Mo_xC nanoparticles, favours the transfer of the photogenerated electrons to produce H_2 from the aqueous ethanol solution. 1-Mo_xC/TiO_2(bipy) produced the highest amount of H_2, 1687 μmol g^{-1}_{cat} h^{-1} under the experimental conditions used.

ANNEX

Annex: Copyright permissions

Kudo A, Miseki Y. Heterogeneous photocatalyst materials for water splitting. Chemical Society Reviews, 2009, 38: 253-78.

1. Chemical Society reviews

0.00 USD

Article: Heterogeneous photocatalyst materials for water splitting.

Order License ID	Pending	Publisher	ROYAL SOCIETY OF CHEMISTRY, ETC.]
ISSN	0306-0012		
Type of Use	Republish in a thesis/dissertation	Portion	Image/photo/illustration

LICENSED CONTENT

Publication Title	Chemical Society reviews	Rightsholder	Royal Society of Chemistry
Article Title	Heterogeneous photocatalyst materials for water splitting.	Publication Type	Journal
		Start Page	253
Author/Editor	CHEMICAL SOCIETY (GREAT BRITAIN)	End Page	278
		Issue	1
Date	01/01/1972	Volume	38
Language	English		
Country	United Kingdom of Great Britain and Northern Ireland		

REQUEST DETAILS

Portion Type	Image/photo/illustration	Distribution	Worldwide
Number of images / photos / illustrations	1	Translation	Original language of publication
Format (select all that apply)	Electronic	Copies for the disabled?	No
Who will republish the content?	Academic institution	Minor editing privileges?	No
Duration of Use	Current edition and up to 5 years	Incidental promotional use?	No
Lifetime Unit Quantity	Up to 499	Currency	USD
Rights Requested	Main product		

NEW WORK DETAILS

Title	Mr.	Institution name	University of Barcelona
Instructor name	Yan Wang	Expected presentation date	2022-02-03

ADDITIONAL DETAILS

Order reference number	N/A	The requesting person / organization to appear on the license	Yan Wang from University of Barcelona

REUSE CONTENT DETAILS

Title, description or numeric reference of the portion(s)	Figure 1	Title of the article/chapter the portion is from	Heterogeneous photocatalyst materials for water splitting.
Editor of portion(s)	Kudo, Akihiko; Miseki, Yugo	Author of portion(s)	Kudo, Akihiko; Miseki, Yugo
Volume of serial or monograph	38	Issue, if republishing an article from a serial	1
Page or page range of portion	253-278	Publication date of portion	2009-01-01

Total Items: 1 Total Due: 0.00 USD

Accepted: All Publisher and CCC Terms and Conditions

Yuan Y J, Chen D, Yu Z T, et al. Cadmium sulfide-based nanomaterials for photocatalytic hydrogen production. Journal of Materials Chemistry A, 2018, 6: 11606-11630.

1. Journal of materials chemistry. A, Materials for energy and sustainability — 0.00 USD

Article: Cadmium sulfide-based nanomaterials for photocatalytic hydrogen production

Order License ID	Pending	Publisher	Royal Society of Chemistry
ISSN	2050-7488		
Type of Use	Republish in a thesis/dissertation	Portion	Image/photo/illustration

LICENSED CONTENT

Publication Title	Journal of materials chemistry. A, Materials for energy and sustainability	Rightsholder	Royal Society of Chemistry
		Publication Type	Journal
Article Title	Cadmium sulfide-based nanomaterials for photocatalytic hydrogen production	Start Page	11606
		End Page	11630
		Issue	25
Author/Editor	Royal Society of Chemistry (Great Britain)	Volume	6
Date	01/01/2012		
Language	English		
Country	United Kingdom of Great Britain and Northern Ireland		

REQUEST DETAILS

Portion Type	Image/photo/illustration	Distribution	Worldwide
Number of images / photos / illustrations	1	Translation	Original language of publication
Format (select all that apply)	Electronic	Copies for the disabled?	No
		Minor editing privileges?	No
Who will republish the content?	Author of requested content		
		Incidental promotional use?	No
Duration of Use	Current edition and up to 5 years	Currency	USD
Lifetime Unit Quantity	Up to 499		
Rights Requested	Main product		

NEW WORK DETAILS

Title	Mr.	Institution name	University of Barcelona
Instructor name	Yan Wang	Expected presentation date	2022-02-03

ADDITIONAL DETAILS

Order reference number	N/A	The requesting person / organization to appear on the license	Yan Wang from University of Barcelona

REUSE CONTENT DETAILS

Title, description or numeric reference of the portion(s)	Figure 1	Title of the article/chapter the portion is from	Cadmium sulfide-based nanomaterials for photocatalytic hydrogen production
Editor of portion(s)	Yuan, Yong-Jun; Chen, Daqin; Yu, Zhen-Tao; Zou, Zhi-Gang	Author of portion(s)	Yuan, Yong-Jun; Chen, Daqin; Yu, Zhen-Tao; Zou, Zhi-Gang
Volume of serial or monograph	6	Issue, if republishing an article from a serial	25
Page or page range of portion	11606-11630	Publication date of portion	2018-01-01

Total Items: 1 Total Due: 0.00 USD

Ran J, Zhang J, Yu J, et al. Earth-abundant cocatalysts for semiconductor-based photocatalytic water splitting. Chemical Society Reviews, 2014, 43: 7787-7812.

1. Chemical Society reviews

0.00 USD

Article: Earth-abundant cocatalysts for semiconductor-based photocatalytic water splitting.

Order License ID	Pending	Publisher	ROYAL SOCIETY OF CHEMISTRY, ETC.]
ISSN	0306-0012		
Type of Use	Republish in a thesis/dissertation	Portion	Image/photo/illustration

LICENSED CONTENT

Publication Title	Chemical Society reviews	Rightsholder	Royal Society of Chemistry
		Publication Type	Journal
Article Title	Earth-abundant cocatalysts for semiconductor-based photocatalytic water splitting.	Start Page	7787
		End Page	7812
		Issue	22
		Volume	43
Author/Editor	CHEMICAL SOCIETY (GREAT BRITAIN)		
Date	01/01/1972		
Language	English		
Country	United Kingdom of Great Britain and Northern Ireland		

REQUEST DETAILS

Portion Type	Image/photo/illustration	Distribution	Worldwide
Number of images / photos / illustrations	1	Translation	Original language of publication
Format (select all that apply)	Electronic	Copies for the disabled?	No
Who will republish the content?	Academic institution	Minor editing privileges?	No
Duration of Use	Current edition and up to 5 years	Incidental promotional use?	No
Lifetime Unit Quantity	Up to 499	Currency	USD
Rights Requested	Main product		

NEW WORK DETAILS

Title	Mr.	Institution name	University of Barcelona
Instructor name	Yan Wang	Expected presentation date	2022-02-03

ADDITIONAL DETAILS

Order reference number	N/A	The requesting person / organization to appear on the license	Yan Wang from University of Barcelona

REUSE CONTENT DETAILS

Title, description or numeric reference of the portion(s)	Figure 2	Title of the article/chapter the portion is from	Earth-abundant cocatalysts for semiconductor-based photocatalytic water splitting.
Editor of portion(s)	Ran, Jingrun; Zhang, Jun; Yu, Jiaguo; Jaroniec, Mietek; Qiao, Shi Zhang	Author of portion(s)	Ran, Jingrun; Zhang, Jun; Yu, Jiaguo; Jaroniec, Mietek; Qiao, Shi Zhang
Volume of serial or monograph	43		
Page or page range of portion	7787-7812	Issue, if republishing an article from a serial	22
		Publication date of portion	2014-11-21

Total Items: 1

Total Due: 0.00 USD

Zhu B, Zhang L, Cheng B, et al. First-principle calculation study of tri-s-triazine-based g-C_3N_4: a review. Applied Catalysis B: Environmental, 2018, 224: 983-999.

Licensed Content

Licensed Content Publisher	Elsevier
Licensed Content Publication	Applied Catalysis B: Environmental
Licensed Content Title	First-principle calculation study of tri-s-triazine-based g-C3N4: A review
Licensed Content Author	Bicheng Zhu,Liuyang Zhang,Bei Cheng,Jiaguo Yu
Licensed Content Date	May 2018
Licensed Content Volume	224
Licensed Content Issue	n/a
Licensed Content Pages	17

Order Details

Type of Use	reuse in a thesis/dissertation
Portion	figures/tables/illustrations
Number of figures/tables/illustrations	3
Format	electronic
Are you the author of this Elsevier article?	No
Will you be translating?	No

About Your Work

Title	Mr.
Institution name	University of Barcelona
Expected presentation date	Feb 2022

Additional Data

Portions	Figure 3

Requestor Location

Requestor Location	UB Carrer de Martí i Franquès, 1-11, 08028 Barcelona, Barcelona 08028 Spain Attn: UB

Tax Details

Publisher Tax ID	GB 494 6272 12

Billing Information

Billing Type	Invoice
Billing address	UB Carrer de Martí i Franquès, 1-11, 08028 Barcelona, Spain 08028 Attn: UB

Price

Total	0.00 USD

Total: 0.00 USD

Hou Y, Laursen A B, Zhang J, et al. Layered nanojunctions for hydrogen‐evolution catalysis. Angewandte Chemie International Edition, 2013, 125: 3709-3713.

Order Completed

Thank you for your order.

This Agreement between UB -- YAN WANG ("You") and John Wiley and Sons ("John Wiley and Sons") consists of your license details and the terms and conditions provided by John Wiley and Sons and Copyright Clearance Center.

Your confirmation email will contain your order number for future reference.

License Number	5241251204206
License date	Feb 03, 2022

Printable Details

Licensed Content

Licensed Content Publisher	John Wiley and Sons
Licensed Content Publication	Angewandte Chemie
Licensed Content Title	Layered Nanojunctions for Hydrogen-Evolution Catalysis
Licensed Content Author	Ib Chorkendorff, Søren Dahl, Xinchen Wang, et al
Licensed Content Date	Mar 12, 2013
Licensed Content Volume	125
Licensed Content Issue	13
Licensed Content Pages	5

Order Details

Type of use	Dissertation/Thesis
Requestor type	University/Academic
Format	Electronic
Portion	Figure/table
Number of figures/tables	1
Will you be translating?	No

About Your Work

Title	Mr.
Institution name	University of Barcelona
Expected presentation date	Feb 2022

Additional Data

Portions	abstract figure

Licensed Content

Licensed Content Publisher	John Wiley and Sons
Licensed Content Publication	Angewandte Chemie
Licensed Content Title	Layered Nanojunctions for Hydrogen-Evolution Catalysis
Licensed Content Author	Ib Chorkendorff, Søren Dahl, Xinchen Wang, et al
Licensed Content Date	Mar 12, 2013
Licensed Content Volume	125
Licensed Content Issue	13
Licensed Content Pages	5

Order Details

Type of use	Dissertation/Thesis
Requestor type	University/Academic
Format	Electronic
Portion	Figure/table
Number of figures/tables	1
Will you be translating?	No

About Your Work

Title	Mr.
Institution name	University of Barcelona
Expected presentation date	Feb 2022

Additional Data

Portions	abstract figure

Requestor Location

Requestor Location	UB Carrer de Martí i Franquès, 1-11, 08028 Barcelona, Barcelona 08028 Spain Attn: UB

Tax Details

Publisher Tax ID	EU826007151

Price

Total	0.00 USD

Chang X, Wang T, Gong J. CO_2 photo-reduction: insights into CO_2 activation and reaction on surfaces of photocatalysts. Energy & Environmental Science, 2016, 9: 2177-2196.

1. Energy & environmental science

0.00 USD

Article: CO2 photo-reduction: insights into CO2 activation and reaction on surfaces of photocatalysts

Order License ID	Pending	Publisher	Royal Society of Chemistry
ISSN	17545692		
Type of Use	Republish in a thesis/dissertation	Portion	Image/photo/illustration

LICENSED CONTENT

Publication Title	Energy & environmental science	Rightsholder	Royal Society of Chemistry
		Publication Type	Journal
Article Title	CO2 photo-reduction: insights into CO2 activation and reaction on surfaces of photocatalysts	Start Page	2177
		End Page	2196
		Issue	7
		Volume	9
Author/Editor	Royal Society of Chemistry (Great Britain)		
Date	01/01/2008		
Language	English		
Country	United Kingdom of Great Britain and Northern Ireland		

REQUEST DETAILS

Portion Type	Image/photo/illustration	Distribution	Worldwide
Number of images / photos / illustrations	1	Translation	Original language of publication
Format (select all that apply)	Electronic	Copies for the disabled?	No
		Minor editing privileges?	No
Who will republish the content?	Academic institution		
		Incidental promotional use?	No
Duration of Use	Current edition and up to 5 years	Currency	USD
Lifetime Unit Quantity	Up to 499		
Rights Requested	Main product		

NEW WORK DETAILS

Title	Mr.	Institution name	University of Barcelona
Instructor name	Yan Wang	Expected presentation date	2022-02-03

ADDITIONAL DETAILS

Order reference number	N/A	The requesting person / organization to appear on the license	Yan Wang from University of Barcelona

REUSE CONTENT DETAILS

Title, description or numeric reference of the portion(s)	Figure 2	Title of the article/chapter the portion is from	CO2 photo-reduction: insights into CO2 activation and reaction on surfaces of photocatalysts
Editor of portion(s)	Chang, Xiaoxia; Wang, Tuo; Gong, Jinlong	Author of portion(s)	Chang, Xiaoxia; Wang, Tuo; Gong, Jinlong
Volume of serial or monograph	9	Issue, if republishing an article from a serial	7
Page or page range of portion	2177-2196	Publication date of portion	2016-07-06

Total Items: 1 Total Due: 0.00 USD